Structure-guided design of an IL-1β immunogen for the treatment of autoinflammatory diseases

Thesis submitted for the degree of Doctor of Philosophy in Clinical Medicine

Gilles A. S. Augusto

Supervised by Prof Martin Bachmann, Prof David Stuart, and Dr Aadil El-Turabi

Merton College

Trinity Term, 2024

Word count: 16,307

To my parents Cecilia and Claudio
Augusto, whose countless sacrifices
made this wonderful journey possible.

Structure-guided design of an IL-1β immunogen for the treatment of autoinflammatory diseases

Abstract

Systemic autoinflammatory diseases are a group of immunological disorders characterised by recurrent events of generalised sterile inflammation. Central to the pathogenesis of most SAIDs is the overproduction of interleukin-1β, a potent proinflammatory cytokine normally secreted by cells of the innate immune system in response to infections. Not surprisingly, the most advanced therapies for SAIDs are based on the precise inhibition of IL-1β, which is carried out either by a specific monoclonal antibody or by a recombinant version of the endogenous IL-1 receptor antagonist. Although effective in ameliorating the symptoms of mild-to-moderate systemic inflammation, these biologicals offer only limited benefits to the patients suffering from the most severe forms of SAIDs, particularly those presenting neurological involvement. In addition to their inherent poor blood-brain barrier penetrability, the monospecific nature of these inhibitors is the most likely reason for their partial efficacy, given that it allows for residual cytokine bioavailability when it occurs at extremely high concentrations, as in the event of a severe flare. Addressing this issue, we have developed a virus-like particle-vectored therapeutic vaccine capable of eliciting neutralising polyclonal antibody responses against IL-1β protective even in the event of an extreme flare. To further improve its safety and (potentially) efficacy, we have also submitted the carried antigen to extensive modifications in a way that its interactions with IL-1β's endogenous receptors were nearly abrogated, with no major effect on the cross-reactivity between the two proteins. This thesis discusses the design approach employed on this task, particularly focusing the translational potential of the devised techniques.

Preface

As further discussed below, this thesis addresses the problem of the unexpectedly high B-call tolerance observed for an anti-interleukin 1β immunogen in clinical studies. Based on positive results from previous studies performed with other vaccines targeting similar autologous antigens, we hypothesised that the unusually low immunogenicity of the cytokine in humans may have been caused by interactions between the tested vaccine and the soluble forms of IL-1β's endogenous receptors, in particular the high-affinity decoy receptor IL-1R2. Although some supporting evidence is discussed along the text, demonstrating this hypothesis is not the primary aim of this thesis. It is rather focused on discussing the rationale, methods, and results related to an immunogen design strategy conceived for bypassing endogenous interactions while maintaining a high level of neutralising cross-reactivity with the targeted antigen.

Due the broad applicability of the devised methods (e.g., on improving the safety profiles of vaccines by modulating the cross-reactivity of their elicited antibody responses), this text is structured in a way that facilitates the progressive understanding of the process, with each experimental chapter reflecting a major step in the design pipeline. In this way, the case for a new therapeutic vaccine targeting IL-1β is presented in chapter I, together with a non-exhaustive review of previous development attempts.

Chapter II discusses the rationale guiding the redesign of IL-1β's surface, beginning with a thorough description of the energy minimisation-based method employed for the generation and initial assessment of mutated sequences. The discussion then focuses on the stability analysis of selected designs by molecular dynamics. Finally, a discussion on how these distinct techniques complement each other is proposed.

Chapter III then describes the biophysical characterisation of the selected muteins, beginning with binding kinetics assays performed to assess the effects of the designed modifications on the interactions between sIL-1R2 and the antigen. Conformational stability analyses of a small number of these mimetics are also discussed in this chapter.

Selected for their low affinity for sIL-1R2, these muteins were subsequently tested *in vivo* for their capacity to elicit neutralising responses against the wildtype cytokine. The results of these assays are presented in chapter IV, which also discusses the relationship between the design strategy and the cross-reactivity among the tested antigens.

Finally, chapter V summarises the conclusions drawn from the previous chapters, also listing the opportunities for improvement identified along the design process. An outlook for future development of an anti-IL-1β therapeutic vaccine based on the most promising mutein is also presented in this chapter.

Acknowledgements

I am deeply grateful for the invaluable support and guidance provided by Prof Martin Bachmann, Prof Sir David Stuart, and Dr Aadil El-Turabi throughout my DPhil studies. Their diligent and gentle supervision, belief in my ideas, and unwavering patience during challenging moments were vital for making this work possible. Their competence and character have inspired me and shaped the kind of scientist I aspire to become. I extend my heartfelt appreciation to Prof Robert Gilbert, the director of the graduate school, and Prof Simon Draper, my college advisor, for their kind mentorship and availability whenever I needed assistance during my academic journey in Oxford. I am also thankful to Simon Jones and the entire welfare team in Merton for their life-saving assistance during critical times over the past five years.

Additionally, I extend my deep gratitude to all the team members in both Oxford and Bern for their generous time, knowledge, and friendship. I particularly want to acknowledge Prof Monique Vogel, the deputy director of the Department of Immunology at the University of Bern, for her guidance during my visiting period at this esteemed institution. Special thanks also go to Lee-Anne Brand, PA to Prof Martin Bachmann, for her attentive support during my transition to the Swiss capital. I am indebted to Dr Simon Zinkhan, Dr Kevin Plattner, and Dr Anne-Kathrine Vogt, all members of the Bachmann group in Bern, for their invaluable help with the *in vivo* experiments.

Furthermore, I am deeply appreciative of the collaboration with our colleagues at the École Polytechnique Fédérale de Lausanne (EPFL), specifically Dr Florence Pojer and Dr Luciano Abriata. Their generous assistance with acquiring, processing, and interpreting biophysical data has significantly contributed to the outcomes presented in this work.

Finally, I would like to acknowledge the immeasurable importance of the Clarendon Scholarship for the realisation of this project. For that, I am profoundly grateful to the Medical Sciences Division of the University of Oxford, the Clarendon Fund, and my forever *alma mater* Merton College.

Conventions

For improved clarity and coherence, this document follows a few lexical conventions:

Names & abbreviations

- The expressions "IL-1β," "native IL-1β," "WT IL-1β," or "wildtype cytokine" all refer to the mature form of human interleukin-1β, used as template for the design of improved anti-IL-1β-based antigens. In this sense, the terms "design(s)" and "sequence(s)" both refer to the model structures of modified IL-1β produced during the *in-silico* phase of the design process, whereas "mimetic(s)," "mutant(s)," and "mutein(s)," designate those selected for subsequent synthesis and biophysical characterisation. Finally, the common jargon "antigen(s)" indicates here only the mutein(s) submitted, together with the wildtype cytokine, to immunisation assays.
- Gene and protein abbreviations follow the style guide of the National Center for Biotechnological Information (NCBI), 2004 edition. That is, acronyms for genes are written in italic, and for proteins in roman style. When from human origin, both types of abbreviations are spelled in upper-case letters. Non-human homologs are written in lower-case letters.
- Genes and proteins were named as they appear in the most recent literature with no mention to historical variations (e.g., *IL1R3* and IL-1R3 instead of the more common *IL1RAP* and IL-1RAcP forms). Two-letter species-designating prefixes were added to the abbreviations of non-human proteins only (e.g., IL-1β for human interleukin-1β, and muIL-1β for its murine homolog). An "s" preceding any protein abbreviation indicates that the referred protein is in its soluble forms (e.g., sIL-1R2 and smuIL-1R2 for the human and murine secreted IL-1R2, respectively).
- Widely employed techniques are mentioned by their most common names (e.g., "nuclear magnetic resonance spectroscopy") and subsequently cited by

their respective abbreviations (e.g., “NMR”). A similar rule applies to standard experimental conditions, which are first mentioned by their complete descriptions and subsequently cited by their most common abbreviations (e.g., “room temperature” and “RT”). Popular consumables, however, are referred to only by their best-known abbreviations (e.g., “PBS” only instead of “phosphate buffer saline” followed by “PBS”). Finally, only the suppliers of the most relevant items (e.g., biolayer interferometer) are cited in the text, initially by their names immediately followed by the address of their headquarters (e.g., “Sartorius, Wokingham RG – UK”), and subsequently by their names only (e.g., “Sartorius”).

Units of measurement

- With a few exceptions (e.g., the angstrom, “Å,” equivalent to $1 \cdot 10^{-10}$ m), all units of measurement cited in this text are part of the International System of Units (SI), and, therefore, are expressed according to the rules preconised by that convention (e.g., “s” for time and “s^{-1}” for frequency). Base units, however, are often abbreviated to their most commonly employed form, independently of lexical imperatives (e.g., “0.3 nM” instead of “300 μM” or “$3 \cdot 10^{-8}$ M”).

Contents

List of figures

List of tables

Structure-guided design of an IL-1β immunogen for the treatment of autoinflammatory diseases

Chapter I. Introduction

1.1. Systemic autoinflammatory diseases (SAIDs)

The term systemic autoinflammatory diseases (SAIDs) collectively refers to a growing number of rare immunological disorders commonly manifested as recurrent events of unprovoked systemic inflammation.[1] In contrast to autoimmune diseases, where autoreactive lymphocytes drive the pathogenic process, SAIDs result primarily from the hyperactivity of monocytes, macrophages, and neutrophils,[2] the reason these diseases are broadly thought of as diseases of the innate immune system.[3]

While the best understood SAIDs arise from mutations in single genes (and therefore are transmitted in a mendelian way), the majority are of polygenic or multifactorial nature, with disease phenotypes frequently determined by environmental factors.[4,5] SAIDs can be further categorised according to their pathophysiology as actinopathies, inflammasomopathies, interferonopathies, ubiquitinopathies, and those caused by other mechanisms[1] (see Appendix A1 for a brief overview of the four classic hereditary recurrent fevers). Approximately 50 phenotypes of SAIDs have been described to date, with their estimated prevalence rarely exceeding 1:200,000 of the general population.[6]

Symptoms of SAIDs vary broadly in presentation and severity. Periodic fever attacks are the most frequent complaint, although not present in all phenotypes. Other common clinical manifestations may include cutaneous and mucosal (e.g., aphthae, erythema, dermatitis, urticaria), haematological (e.g., autoantibodies, cytopenia, immunodeficiency), rheumatological (e.g., polyarthritis, synovitis, tenosynovitis), and neurological (e.g., recurrent meningitis, strokes) features.[6]

1.2. Current therapies for SAIDs

Independently of the pathogenic mechanism, all SAIDs lead to hyperactivity of proinflammatory cytokines, in particular of those belonging to the interleukin 1 (IL-1) and tumour necrosis factor (TNF) families. Hence, the most advanced therapeutics for

SAIDs act by neutralising the effects of these immune mediators, in particular IL-1β, the most potent of the IL-1 cytokines.[7,8] To this end, two biological inhibitors are currently available on the market: anakinra (Kineret, by SOBI), a recombinant version of the endogenous IL-1 receptor antagonist IL-1RA; and canakinumab (Ilaris, by Novartis), a fully human κIgG1 anti-IL-1β monoclonal antibody. Table 1.1 below lists the FDA/EMA indications of the two drugs referencing the clinical studies that supported these approvals.

Kineret is sold as prefilled syringes containing 0.67 mL of anakinra at 150 $mg \cdot mL^{-1}$. The drug is produced in *E. coli* and formulated in citrate at pH 6.5. As listed in Table 1.1, the drug has been proved efficacious in the treatment of several SAIDs, most notably of neonatal-onset multisystem inflammatory disease (NOMID),[9] an extremely severe phenotype of cryopyrin-associated periodic syndrome (CAPS, see Appendix A1.3). Due its requirement for daily injections, however, Kineret is normally prescribed as second-in-line to Ilaris, which is administered much less frequetly. The most common (≥ 10 %) side effects of Anakinra are injection site reaction and cephalgia (headache). Serious infections in the respiratory tract are also commonly (≥ 1 % < 10 %) associated with the use of Kineret.

Due its varied posology,[10] Ilaris is commercialised as 150 mg lyophilised powder for reconstitution in water to be carried out by a healthcare professional. The drug is produced in mouse myeloma Sp2/0 cells and formulated in sucrose, reaching pH values between 6.5 and 6.8 after resolubilisation. It is prescribed as subcutaneous injections every 4-8 weeks depending on the indication. As also listed in Table 1.1, canakinumab has been demonstrated efficacious in the treatment of SAIDs, particularly of the milder phenotypes of CAPS.[11] It has shown little efficacy, however, in the treatment of adult-onset Still's disease (AOSD) and mevalonate kinase deficiency (MKD).[12] Most common side effects include injection site reactions, infections in the respiratory and urinary tracts, abdominal pain, arthralgia, and decreased renal creatine clearance.

Table 1.1 – Current FDA/EMA indications for biological IL-1β blockers. AOSD, adult-onset Still's disease; CAPS, cryopyrin-associated periodic syndrome; DIRA, deficiency in IL-1 receptor antagonist; FMF, familial Mediterranean fever; GA, gouty arthritis; HIDS/MKD, hyperimmunoglobulinemia D syndrome/mevalonate kinase deficiency; RA, rheumatoid arthritis; SIJA, systemic juvenile idiopathic arthritis; TRAPS, tumour necrosis factor-associated periodic syndrome.

Drug	EMA/FDA approval (disease)	Primary endpoint effectiveness (drug/control)	Study	Comments
Anakinra (Kineret)	AOSD	50 % / 20 %	NCT01033656[13]	DMARTs as control
	CAPS	75 % / 93 %	NCT00214851[9]	Canakinumab as control. Approved for NOMID
	DIRA	100 %	NCT00059748[14]	Patients responsive to treatment
	FMF	60 % / 0 %	NCT01705756[15]	Placebo as control. PEP: number of patients with less than a mean of one FMF attack per month
	SJIA	67 % / 8 %	NCT00339157[16]	Placebo as control
	RA	46 % / 19 %	NCT00037648[17] NCT00117091[18]	Placebo or NSAIDs as control
Canakinumab	AOSD	66% / 41% (n.s.)	NCT02204293[19]	Placebo as control. Approved due improvements in secondary endpoints
	CAPS	94 % / 25%	NCT00465985[11,20] NCT00487708[21] NCT00685373[22]	Placebo as control. Approved for all CAPS phenotypes
	FMF	61% / 6%	NCT02059291[23]	Placebo as control
	MKD	35% / 6%	NCT02059291[23,24]	Placebo as control
	SIJA	46% / 0%	NCT00426218[25] NCT00886769[25] NCT00889863[25,26] NCT00891046[25]	Placebo as control. Follow-up: <50% of participants reported a flare in the drug group; >50% reported a flare in the placebo group, with average time of 236 days
	TRAPS	45% / 8%	NCT02059291[23]	Placebo as control
	GA	62%	NCT01362608[27]	Reduction of risk of new flares compared to triamcinolone acetonide (TA)

Because of its neutralising capacity, gevokizumab (GKB) was used, together with canakinumab (CKB) as a benchmark for inhibition of IL-1β in several of the experiments described in this thesis (see section 2.1.2). This mAb was initially developed by XOMA for the treatment of uveitis in patients with Behçet's disease,[28-30] later being discontinued by Novartis after acquiring its licensing rights.

1.3. The need for new therapies for SAIDs

The results from the clinical trials summarised in Table 1.1 above indicated a tendency for reduction in both drug's efficacy as the severity of the treated diseases increases, e.g., from CAPS to MKD to TRAPS (see Appendix A1).[12] This effect is more noticeable in the clinical trials involving patients presenting different phenotypes of the same condition, e.g., from FCAS to MWS to NOMID in CAPS (see Appendix A1.3).[11,20,22] A possible explanation for this trend considers the rapid increase in cytokine concentration during disease flares, more frequent and intense in patients of severe SAIDs. According to this hypothesis, these peaks in IL-1β concentration would be accompanied by proportional increases in cytokine bioavailability, not entirely neutralised by anakinra or canakinumab due the monospecific nature of their binding kinetics.

In this sense, a new drug capable of circumventing this limitation would have the potential to benefit a broad group of patients suffering from severe SAIDs which pathogenesis is centred on the overproduction of IL-1β (see Appendix A1). This project proposes the development of such drug, exploring the cytokine neutralisation by polyclonal antibodies as its main mechanism of action. As discussed in section 1.4.1, several studies have demonstrated the potential of anti-IL-1β active immunisation as a therapeutic strategy against SAIDs and other chronic diseases in which the cytokine plays a role. Among other encouraging results, these earlier attempts have demonstrated the unique capacity of the elicited responses to completely neutralise the pro-inflammatory effects of IL-1β *in vivo*, something not achievable with monospecific interventions. Naturally, new approaches come with new challenges, and those involving the use of anti-

autologous IL-1β immunogens in humans are discussed in the next sections, together with a proposal to overcome these issues.

1.4. An anti-IL-1β therapeutic immunogen

1.4.1. Previous development efforts

The idea of treating chronic inflammatory diseases via immunisation against IL-1 cytokines is not new. Based on the evidence that IL-1β blocking can improve glycaemic control in patients of type 2 mellitus diabetes (T2DM),[31-33] Spohn and colleagues proposed, in 2014,[34] the design of a virus-like particle (VLP)-vectored anti-IL-1β immunogen for treatment of T2DM. The resulting vaccine (named hIL-1b-Qβ) consisted of modified human IL-1β chemically cross-linked to a VLP derived from bacteriophage Qβ.[35] hIL-1b differed from wildtype IL-1β by an amino acid substitution (D145K, numbering the mature sequence 1-153) and an N-terminal insertion (_A1insMDI). It is not clear in the manuscript the reason for inserting a tripeptide N-terminally of the wildtype sequence, apart from the need for adding an initiator codon (M_3) for expression in a bacterial system. The single-point mutation, on the other hand, is aimed at detoxifying the antigen, i.e., to reduce the potent proinflammatory effects of IL-1β. Indeed, D145K hIL-1b showed activity levels in mice ≈ 45 times less activity in mice than the WT cytokine.

Immunisation assays in WT and IL-1β double-knockout C57BL/6 mice using a murine equivalent of the designed particle (i.e., D143K muIL-1β conjugated to Qβ VLP) showed no significant difference in antibody titres against either the antigen or the carrier, suggesting that, at least in mice, the anti-D143K mIL-1b humoral response was not constrained by muIL-1β-specific B-cell repertoire. The authors also demonstrated that the D143K mIL-1b-immunised animals were fully protected against the systemic effects of large amounts of serum muIL-1β. Analyses of antigen-specific $CD4^+$ T cells also showed these animals to lack substantial cell-mediated immunity against

D143K mIL-1b, even with the vaccine formulated with CpGs, a strong vaccine adjuvant.[36]

In a subsequent study,[37] Cavelti-Weder *et al* reported having immunised a large number of rhesus monkeys against either simian or human D145K-mutated IL-1β coupled to Qβ VLP. As expected, the two groups exhibited almost identical serum conversion profiles, reflecting the ≈ 96 % identity between the tested antigens. Unusually though, neutralisation titres only increased after the third injection, requiring three extra boosts to reach their peak values. Despite these seemingly negative results, the authors proceeded to exploratory trials enrolling patients of T2DM. In this case, however, immunotolerance to the vaccine proved to be even stronger: of the six dose regimens tested, only the most aggressive (6-8 x 900 μg of hIL-1b-Qβ s.c.) led to serum conversion, with all the others failing to produce significant anti-IL-1β antibody titres. Based on a previous first-in-human trial with another auto-antigen conjugated to Qβ,[38] in which high neutralising antibody titres were obtained with two injections only, the authors argued that the poor immunogenicity observed for hIL-1b-Qβ in this study might have been due the apparent high B-cell tolerance humans exhibit towards IL-1β in particular. This hypothesis is in connection with the fact that, contrary to other proinflammatory cytokines (e.g., IFNα, IL-1α, and IL-6),[39,40] spontaneously generated auto-antibodies against IL-1β are not found in healthy individuals following an infection.[41]

In a similar direction, Zha and colleagues,[42] reported the development of an anti-IL-1β immunogen composed of a 30 residue-long peptide (V163-F228) adjuvated with polylactic acid (PLA) microparticles. Despite the modest B-cell responses obtained from KK-A^y mice, a model for T2DM, immunisation with the so called 1βEPP vaccine resulted in a noticeable improvement in both glucose control and body weight gain. The authors later presented what seems like a new version of the same immunogen (sequence still undisclosed) having Alum instead of PLA microparticles as adjuvant.[43] Although the tested formula moderately increased total anti-IL-1β IgG titres, immunisation with 1βEPP under comparable conditions failed to yield additional improvements in diabetes readouts.

Exploring the role of IL-1β in skin hypersensitivity,[44,45] Goksøyr and colleagues recently proposed neutralising the cytokine via active immunisation as a new therapeutic strategy for allergic contact dermatitis (ACD).[46] For that purpose, the authors designed an immunogen made of the secreted sequence of IL-1β covalently bound to the surface of the AP205 VLP via their previously developed Tag/Catcher system.[47] Interestingly, immunisation assays in WT C57BL/6 mice with either muIL-1β or its detoxified Q15G version coupled to the VLP (3 x 10 μg equivalent of antigen in Addavax, i.m.) resulted in significantly higher antibody titres against the mutated cytokine, suggesting a particular relationship between B-cell tolerance and receptor binding properties for IL-1β. The authors have also demonstrated that animals pre-sensitised with 1-fluoro-2,4-dinitrobenzene (DNFB, a model for ACD) resisted allergen challenge if immunised against muIL-1β Q15G.

1.4.2. Proposal for a new design

These experiences indicate that the main challenge faced by the development of an anti-IL-1β therapeutic vaccine is the atypically low immunogenicity of the cytokine, apparently specific to humans and non-human primates. The fact that other clinical studies performed with vaccines targeting similar cytokines (e.g., IFNα[48] and TNFα[49]) resulted in satisfactory neutralising antibody titres rules out the hypothesis that the poor responses obtained from the trial reported by Cavelti-Weder and colleagues[37] (see section 1.4.1) were due to a lack of B-cell repertoire against IL-1β.

An alternative explanation considers the differences in the way the cytokine interacts with its endogenous receptors in humans and mice. Although rodents also possess IL-1R2, this decoy receptor plays a more relevant role in the negative control of IL-1β's potent pro-inflammatory activity in humans,[50] binding the cytokine with significantly higher affinity than IL-1R1 both on the cell's membrane and extracellular space when in its secreted form [51] (for a detailed description of the interactions between IL-1β and types 1, 2, and 3 IL-1 receptors, see section 2.1.1, chapter II). This hypothesis then states that an unpredicted (and, as demonstrated in section 3.2.2.1, irreversible) association

between endogenous sIL-1R2 and the IL-1β displayed by the VLP shields the antigen from B-cell receptors, markedly decreasing its immunogenicity.

Therefore, an improved VLP-vectored immunogen displaying a modified version of IL-1β with significantly reduced affinity for IL-1R2 would have the potential to by-pass the remarkably high immunotolerance exhibited by humans towards this specific cytokine, fully harnessing the potential of this vaccine platform for the treatment of chronic diseases.[52] The design of such improved antigen is the object of this project.

1.4.2.1. Design strategy and expected results

The design of a highly cross-reactive version of IL-1β with significantly reduced affinity for sIL-1R2 faces a few difficult challenges, the most relevant one being the need to maintain the antigen's surface as intact as possible (and, therefore, highly cross-reactive against the wildtype cytokine) while disrupting remarkably strong interactions with the receptor. Another issue is the almost perfect overlapping between the interfaces of IL-1R2 and IL-1R1, implying that modifications performed in one receptor's binding site will inevitably affect cross-reactivity against the other. A strategy to overcome this limitation was to concentrate the performed mutations only on the cytokine's interface with domain D3 of IL-1R2, thus preserving the areas interacting with domains D1 and D2 (see section 2.2.1). Restricted by this constrain, 12 residues located in three segments of this region were selected to be replaced by others capable of disrupting the interactions irreversibly binding IL-1R2 to the cytokine. The expected result then is a significant reduction in the affinity of the cytokine for its decoy receptor.

It is expected, however, that mutating ≈ 8 % of the protein's sequence will have an effect on the overall conformation of the designed muteins, potentially affecting their cross-reactivity with the wildtype cytokine. Addressing this possibility, advanced computational methods (developed by other teams) were employed on the design and preliminary conformational analysis of these IL-1β-derived muteins (see sections 2.2.2 and 2.2.3 ,chapter II), with the primary aim of restricting the number of generated sequences

to those most likely to exhibit the desired biophysical and immunological properties (discussed in chapters III and IV, respectively).

Chapter II. Computational design of IL-1β-based antigens

2.1. Introduction

As mentioned in section 1.4.1, early attempts of designing an anti-IL-1β immunogen targeting the cytokine's secreted sequence (wildtype[53] or single-pointedly mutated for reduced toxicity[54]) produced satisfactory antibody responses in rodents but not in humans.[37] Considering the number of clinical studies demonstrating that B-cell repertoire is not a limiting factor for the immunogenicity of autologous antigens in humans,[52] undesired interactions with endogenous receptors emerged as a potential cause for IL-1β's poor immunogenicity in primates. In this sense, an extensive surface redesign approach has been proposed as a mean for bypassing these interactions, which, in addition to posing a safety concern, could potentially shield the antigen from binding to its cognate B-cell receptors (see section 1.4.2).

This chapter describes the rationale underlying the design strategy, as well as the methods and results of each *in-silico* assay performed. It begins with a discussion on the structural features of IL-1β's interactions with types 1, 2, and 3 IL-1 receptors (section 2.1.1), as well as with canakinumab (CKB) and gevokizumab (GKB, section 2.1.2), two clinically relevant neutralising monoclonal antibodies (see section 1.2, chapter I). These detailed structural analyses provided the necessary information for a rational selection of a set of residues to be mutated on the cytokine's surface, described in section 2.2.1.

Section 2.2.2 is dedicated to the description of the computational simulations performed for the generation of the initial set of mutated sequences. The method employed here makes use of stochastic energy sampling/minimisation for building structural models of altered protein sequences.[55,56] Its execution protocol includes, in addition to the instructions relative to the positions and nature of the substitutions, a set of filters intended to rapidly assess the structural characteristics of the yielded models and discard those more likely to assume conformations too dissimilar to IL-1β's. The primary aim

of this screening process – continued in the subsequent steps – is to the ensure that the muteins selected for *in vivo* characterisation (chapter V) will exhibit the highest possible level of cross-cross reactivity with the wildtype cytokine. The results of these simulations are discussed in section 2.3.1.

Finally, section 2.2.3 describes the second step in the *in-silico* phase of the project: the assessment, by molecular dynamics, of the conformational stability of designed sequences selected from the previous step. The aim of these MD simulations is to compare the structural movements undergone by the selected designs with those observed for the native cytokine under similar conditions, an effort to predict precipitation and/or aggregation during protein expression. Discussed in section 2.3.2, the results of this comparison are also key for the interpretation of the differences in the immunological properties of the designed muteins, investigated in chapter IV.

2.1.1. Structural features of IL-1β-mediated signalling

Secreted IL-1β is the product of proteolytic activation of a 269 residue-long (≈ 31 kDa) cytosolic precursor. This Caspase 1-mediated reaction yields a polypeptide of 153 residues (≈ 18.6 kDa) folded into 13 β-strands and 2 α-helices (Figure 2.1A). While the β -sheets are embedded in the core of the protein, the α-helices and connecting loops are mostly exposed to the solvent (Figure 2.1B), forming the majority of the interaction surface between the cytokine and its receptors.

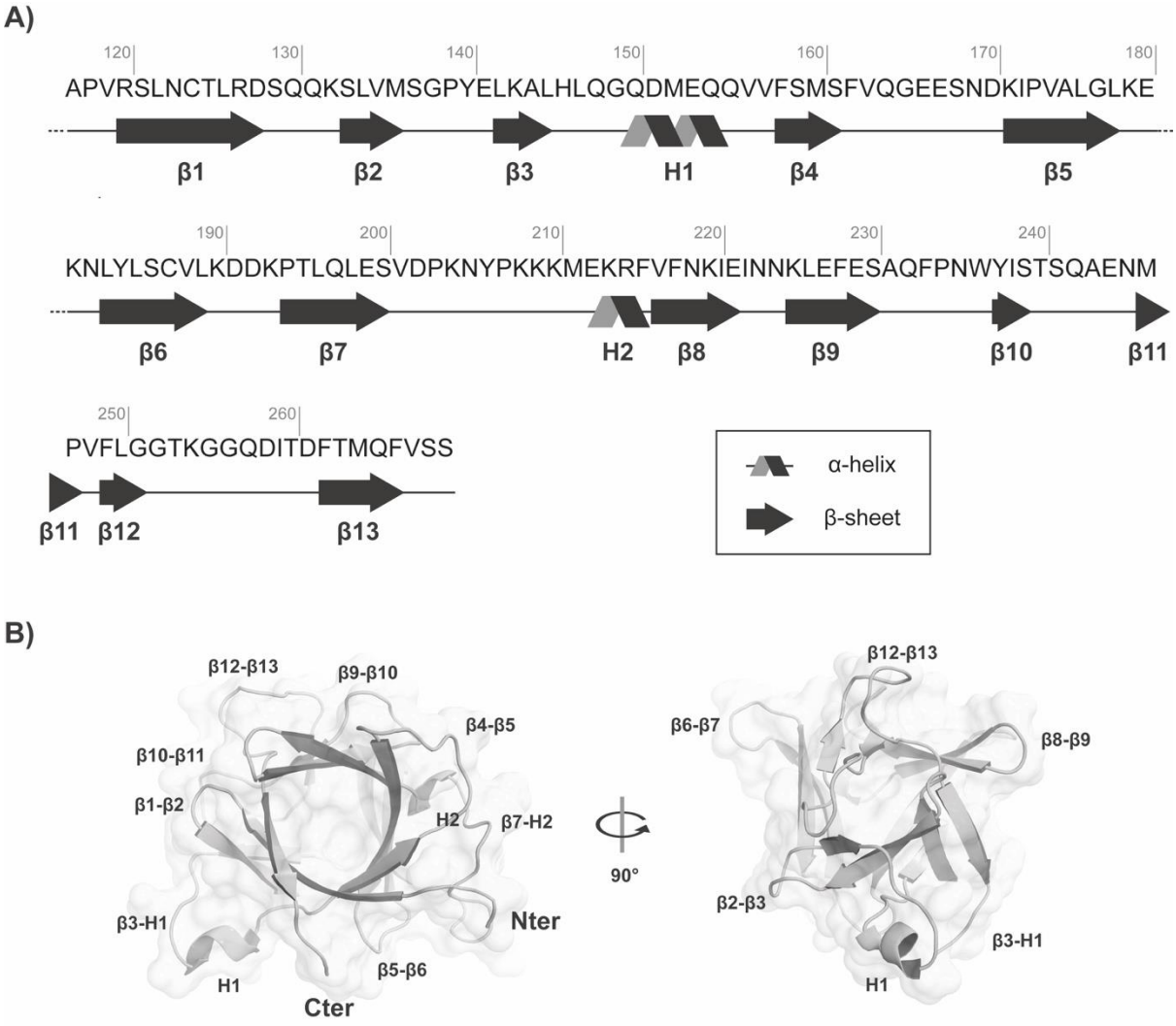

Figure 2.1 – Structure of IL-1β. A) IL-1β's primary and secondary structures. Residues are numbered from the initiator methionine of the precursor sequence, although the 116 N-terminal residues of pro-IL-1β (cleaved off by Caspase 1 during proteolytic activation) are not shown. Secondary structures are numbered from the first β-strand of the mature cytokine. **B)** Two perspectives of the protein's tertiary structure. Only α-helices and loops are indicated. Loops are numbered according to the secondary structures they connect. From PDB 1IOB.

Mechanistically, IL-1R1 binds IL-1β initially via a specific interaction with two of its three domains, D1 and D2, which, due their structural proximity, behave as a single ligand-recognition domain (D1/D2).[51] The long flexible loop connecting D1/D2 to D3 allows the cytokine to subsequently interact with IL-1R2's third domain, which increases the interface area in ≈ 126 %, from 803 to 1,819 Å^2. This area corresponds to ≈ 22 % of the total solvent-accessible area of the cytokine (Figure 2.2A). This enlargement of contact surface likely translates into an increased binding affinity, which in turn stabilises the complex in a conformation suitable for association of the coreceptor.

Although IL-1R3 does not interact extensively with IL-1β, it contributes to the stabilisation of the complex (IL-1β-IL-1R1)-IL-1R3 by binding both domains D2 and D3 of IL-1R1 (Figure 2.2B).

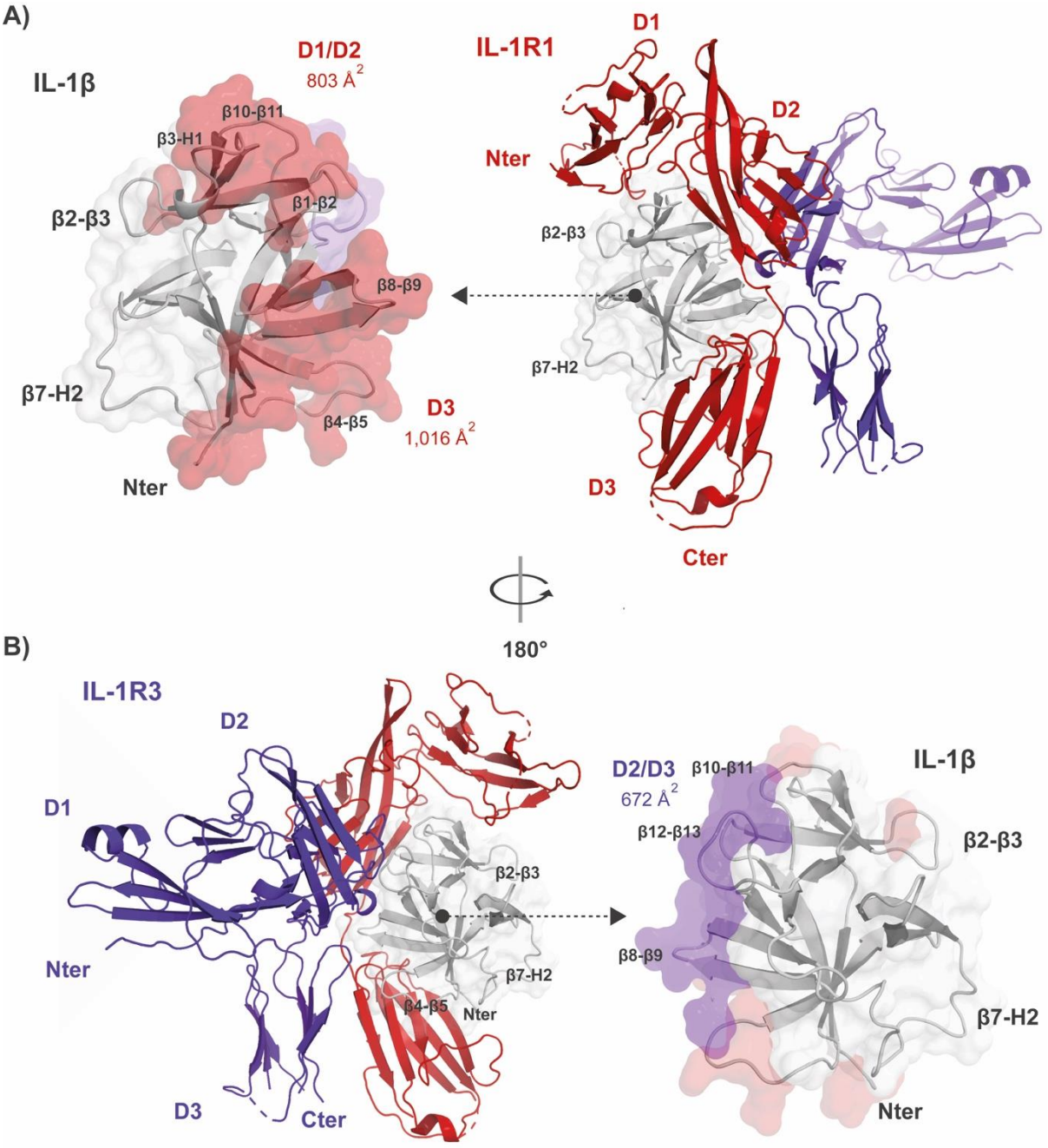

Figure 2.2 – IL-1β's signalling-competent complex. A) (right) A perspective of the [IL-1β-IL-1R1]-IL-1R3 complex. (left) Detail of the interaction surface between IL-1β and IL-1R1 (red). **B)** (left) Same perspective shown in A) rotated 180° . (right) Detail of the interaction surface between IL-1β and IL-1R3 (violet). IL-1β is represented as grey ribbon and surface, IL-1R1 as red ribbon, and IL-1R3 as violet ribbon. Surface areas calculated by SASA with solvent diameter of 1.4 Å. From PDB 4DEP.

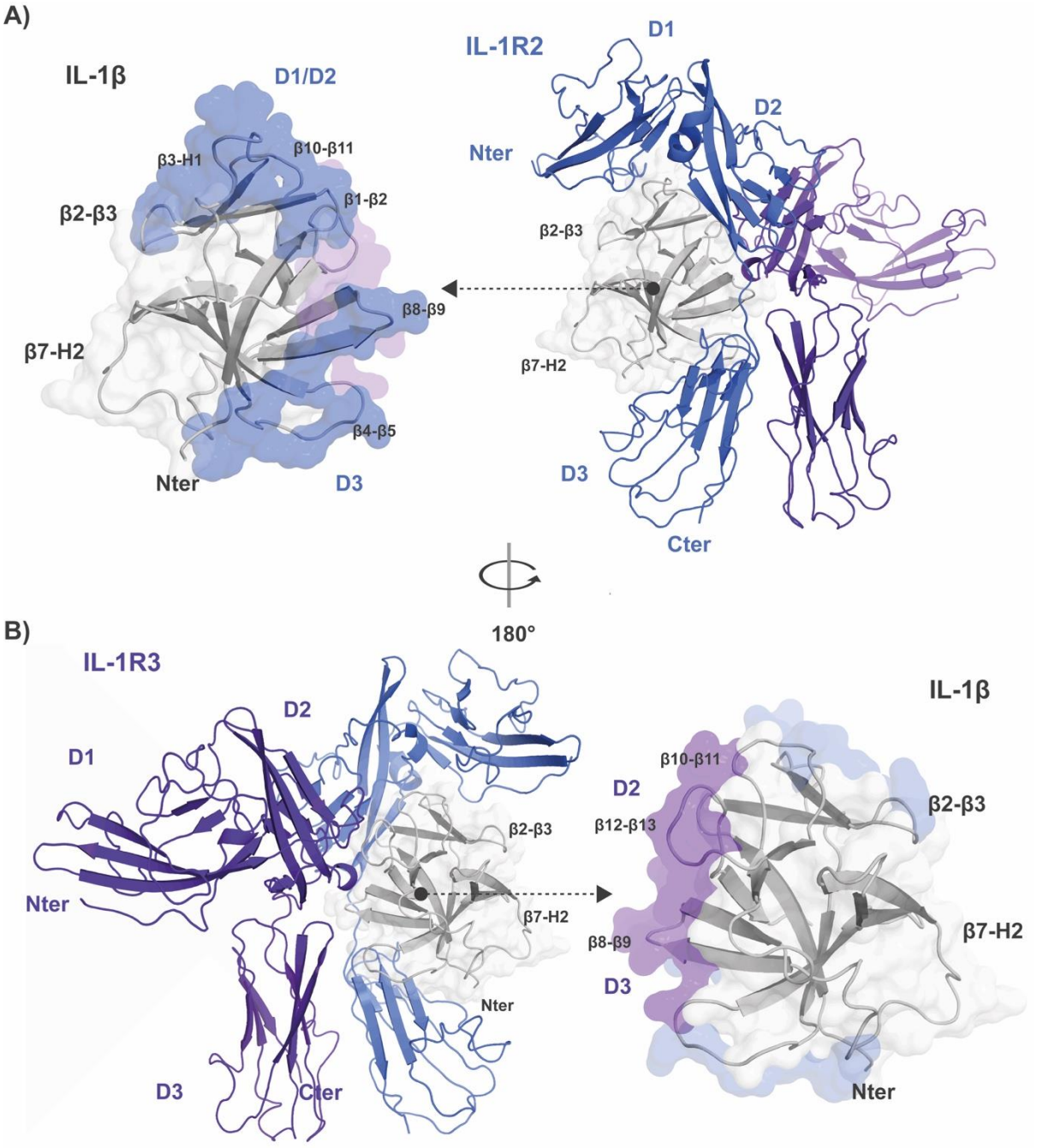

Figure 2.3 – IL-1β's signal-blocking complex. A) (right) A perspective of the [IL-1β-IL-1R2]-IL-1R3 complex. (left) Detail of the interaction surface between IL-1β and IL-1R2 (blue). **B)** (left) Same perspective shown in A) rotated 180° . (right) Detail of the interaction surface between IL-1β and IL-1R3 (violet). IL-1β is represented as grey ribbon and surface, IL-1R2 as blue ribbon, and IL-1R3 as violet ribbon. From PDB 3O4O.

Binding of IL-1β to IL-1R2 and subsequent recruitment of IL-1R3 follows a similar mechanism, although, since this so called "decoy" receptor constitutively lacks the required cytosolic TIR domain, formation of the ternary complex (IL-1β-IL-1R2)-IL-1R3 does not lead to transduction of the upstream signal.[57] Therefore, by trapping both

ligand and coreceptor into a signalling-incompetent complex, IL-1R2 negatively controls the cytokine's activity, a regulatory function consistent with the fact that its affinity for IL-1β is orders of magnitude higher than that of IL-1R1.[50] Interestingly, however, despite their marked differences in binding kinetics, both IL-1R1 and IL-1R2 interact with the same secondary structures on IL-1β: D1/D2 with loops β1-β2, β2-β3, β3-H1 and β10-β11; and D3 with loops β4-β5, β8-β9 and the N-terminus of the cytokine (Figure 2.2A and Figure 2.3A). As discussed below in section 2.2.1, this structural feature restricted the selection of the mutation points on IL-1β to the interface with D3 only, since cross-reactivity with D1/D2 is an essential part of the design strategy.

Not surprisingly, when complexed with IL-1R2, IL-1R3 the interaction surface on IL-1β covers the same area as when associated with IL-1R1, which comprises mainly loops β8-β9, β10-β11, β12- β13 (Figure 2.2B and Figure 2.3B). Differently from the ternary complex involving the primary receptor, however, docking of IL-1R3 is not required for stabilisation of the (IL-1β-IL-1R2)-IL-1R3 complex given that the interaction IL-1β-IL-1R2 is nearly irreversible already (hence sIL-1R2, and not sIL-1R1, can solely neutralise IL-1β in the extracellular environment)[50]. Exploiting this particularity of IL-1R3 binding to the cytokine, Spohn and colleagues showed that mutation D145K (numbering the secreted sequence only), which forms a salt bridge with residue S205 of IL-1R3 (numbering counting from signal peptide), significantly decreases IL-1β's activity,[58] likely reflecting a destabilisation of the complex (IL-1β-IL-1R1)-IL-1R3.

2.1.2. Inhibition of IL-1β by canakinumab and gevokizumab

The structural features of canakinumab and gevokizumab binding to IL-1β, as well as their effects on the inhibition of the cytokine, have been thoroughly described by Blech and colleagues.[59] Briefly, the two mAbs bind symmetrically opposite conformational epitopes (Figure 2.4A), with canakinumab's being formed by loops β2-β3, β3-H1, β5-β6 and β7-H2, and gevokizumab's by loops β4-β5, β6-β7, β7-H2, H2, H3 and β9-β10 (Figure 2.4B). These sites are similarly extensive, each covering ≈ 36 % of the cytokine's total SASA.

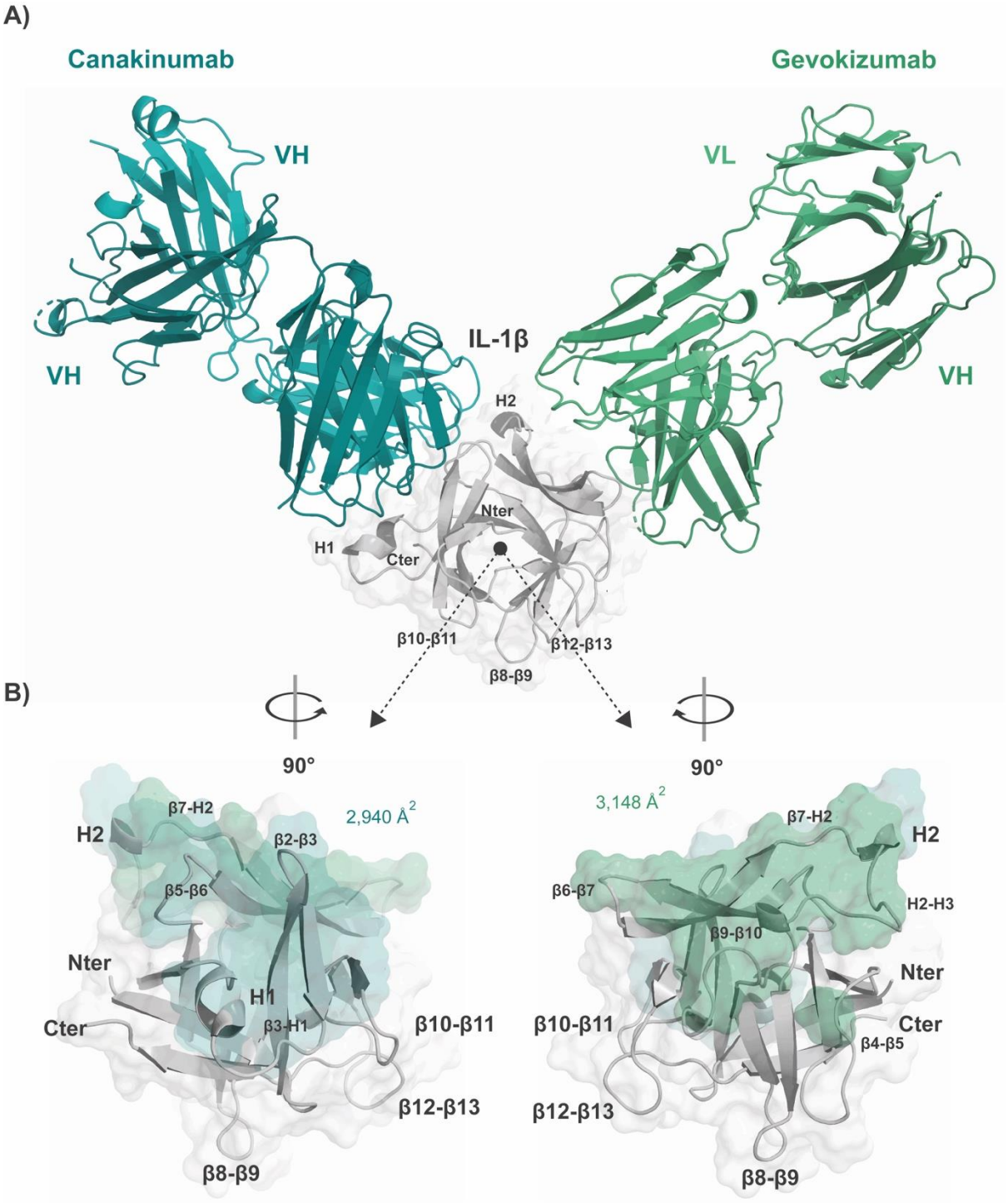

Figure 2.4 – IL-1β in complex with canakinumab and gevokizumab. A) Alignment of the crystal structures of IL-1β in complex with canakinumab (PDB 4G6J) and IL-1β in complex with gevokizumab (PDB 4G6M). **B)** (left) Detail of the interaction surface between IL-1β and canakinumab (cyan). (right) Detail of the interaction surface between IL-1β and gevokizumab (green). IL-1β is represented as grey ribbon and surface; canakinumab and gevokizumab F_{ab} fragments as cyan and green ribbon, respectively.

More interestingly though, superposition of the crystal structure of IL-1β bound to canakinumab Fab fragment onto that of the cytokine in complex with IL-1R1 reveals

a substantial steric impediment between the V_H domain of this mAb and the ligand-recognition domains D1/D2 of the receptor (Figure 2.5, upper detail). A slight interference with binding of the affinity-enhancing domain D3 of IL-1R1, however, is observed when the superimposed structure has gevokizumab Fab fragment as IL-1β's binding partner (Figure 2.5, lower detail). In general, these observations agree with results of MST and SPR inhibition assays, which show canakinumab to directly compete with the receptors for IL-1β while gevokizumab blocks the cytokine primarily via non-competitive mechanisms (e.g., increase of target turnover).

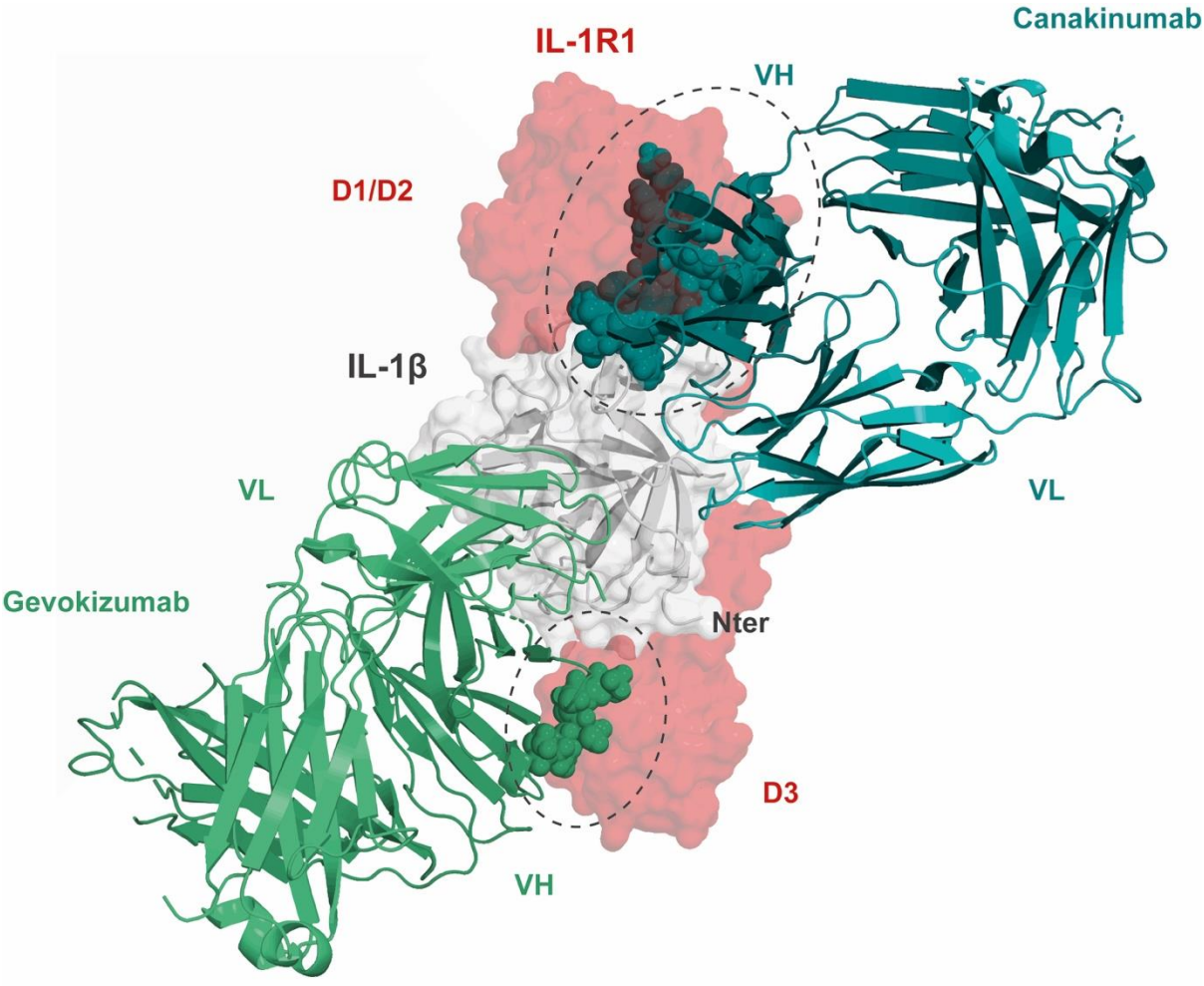

Figure 2.5 – IL-1β in complex with IL-1R1, canakinumab and gevokizumab. Alignment of the crystal structures of IL-1β in complex with IL-1R1/IL-1R3 (PDB 4DEP) and those of the cytokine in complex with either canakinumab Fab fragment (PDB 4G6J) or gevokizumab Fab fragment (PDB 4G6M). Dashed lines highlight steric impediment. IL-1β is represented as grey ribbon and surface; canakinumab as cyan ribbon and spheres, and gevokizumab as green ribbon and spheres. IL-1R3 is omitted for clarity.

Given their clinical relevance (and, therefore, their potential for eliciting neutralising antibodies), the epitopes of both canakinumab and gevokizumab were kept protected from the modifications implemented in the design protocol. The importance of this measure is illustrated by the fact that only two of the twelve mutations carried out on the surface of IL-1β (K209 and K210, Figure 2.6 and Figure 2.7 in section 2.2.1) altered the binding kinetics between gevokizumab and the designed muteins (section 3.2.2.1).

2.2. Material & methods

2.2.1. Selection of mutation points

As discussed in section 2.1.1, the first point of interaction between IL-1R2 and IL-1β is the area on the cytokine interfacing the ligand-recognition domain D1/D2 of the receptor. Modifying it to disrupt this initial interaction would, therefore, constitute a logical strategy for bypassing the inhibitory effects of sIL-1R2 on IL-1β-based immunogens. Nonetheless, given that the binding sites of the primary and decoy receptors on IL-1β almost perfectly overlap, it would also be reasonable to suppose that mutations on this particular area could significantly reduce the probability that the elicited antibodies would block recognition of the cytokine by IL-1R1. As a solution for this problem, only residues interfacing with the affinity-enhancing domain D3 of IL-1R2 were selected to be mutated by the design protocol, with all the other potentially neutralising sites kept intact, including the epitopes of canakinumab and gevokizumab (Figure 2.6A).

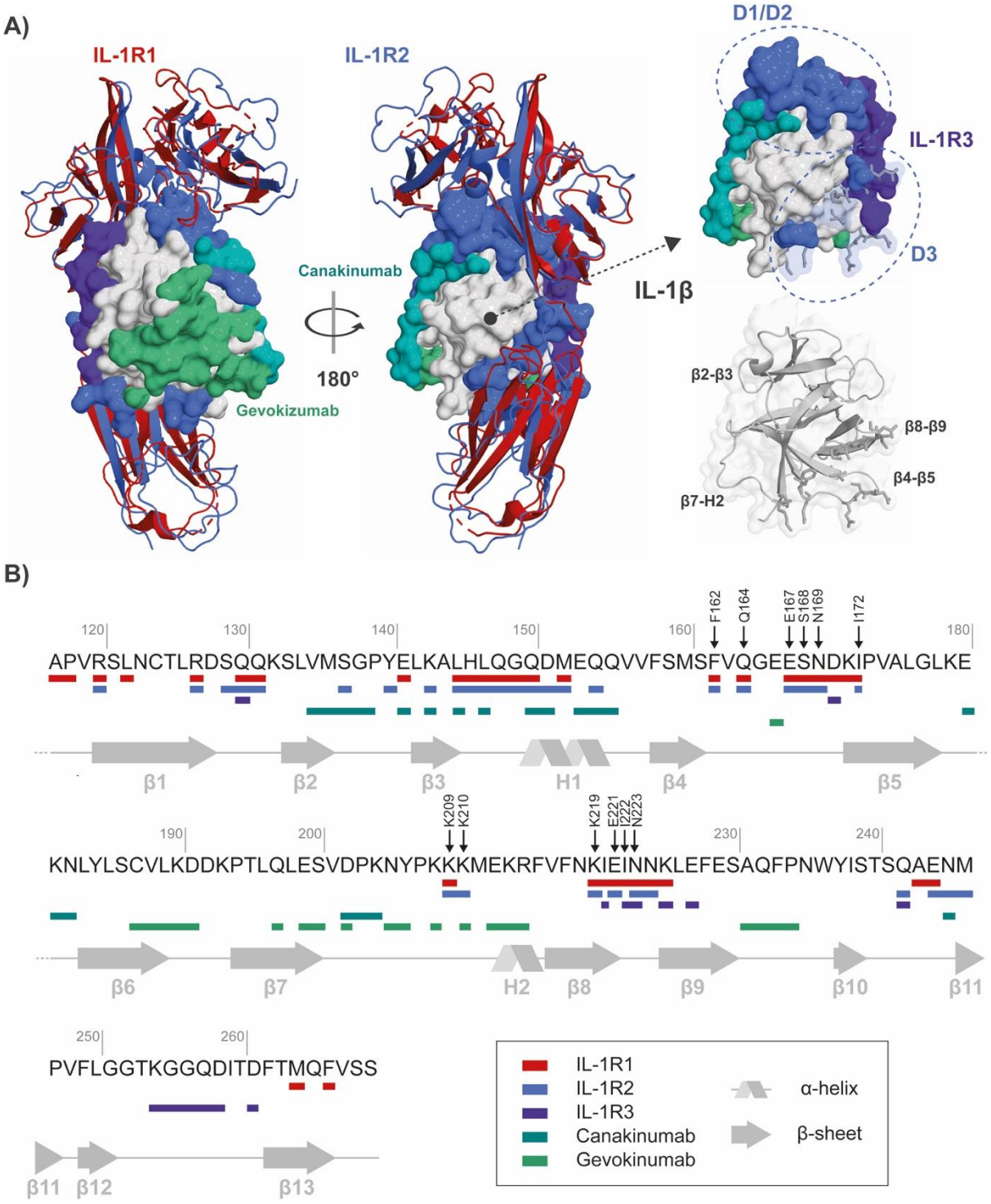

Figure 2.6 – Selection of mutation points on the surface of IL-1β. A) Superposition of the crystal structures of IL-1β in complex with either sIL-1R1 (PDB 4DEP) or sIL-1R2 (PDB 3O4O), detailing the positions of the selected mutation points relative to the interface between the cytokine and the affinity-enhancing domains D3 of both receptors. Present in both complexes, the structure of sIL-1R3 was omitted for clarity. **B)** Distribution of the binding sites of sIL-1R1, sIL-1R2, sIL-1R3, canakinumab and gevokizumab along the primary and secondary structures of IL-1β. Vertical arrows indicate the selected mutation points.

A total of 12 residues covering ≈ 25 % of the surface of the cytokine were set as mutation points: six between sheets β4 and β5 (F162, Q1654, E167, S168, N169 and I172); two between sheet β7 and helix H2 (K209 and K210); and four between sheets β8 and β9 (K219, E221, I222 and N223, Figure 2.6B). With the exception of K210, all these residues interact with both IL-1R1 and IL-1R2. The detailed nature of each interaction with IL-1R2 is illustrated in Figure 2.7, and briefly described below (IL-1R2 residues in *italic*):

- F162 interacts hydrophobically with *M271* (Figure 2.7B);
- Q164 interacts electrostatically with *W273*, being further stabilised by an intrachain electrostatic interaction with E167. E167 also interacts hydrophobically with *W273* (Figure 2.7C);
- N169 interacts electrostatically with the backbone of *F334*, which side chain interacts hydrophobically with S168. An intrachain electrostatic interaction is also observed between S169 and N169 (Figure 2.7D);
- I172 interacts hydrophobically with *N330* (Figure 2.7E);
- Both K209 and K210 interact electrostatically with *E282* (Figure 2.7F);
- A H-bond is formed between K219 and *T269* (Figure 2.7G);
- E221 interacts both electrostatically and hydrophobically with *T331* (Figure 2.7H).
- I222 does not interact directly with IL-1R2 (not shown in Figure 2.7).
- N223 forms a H-bond with *K231* (Figure 2.7I).

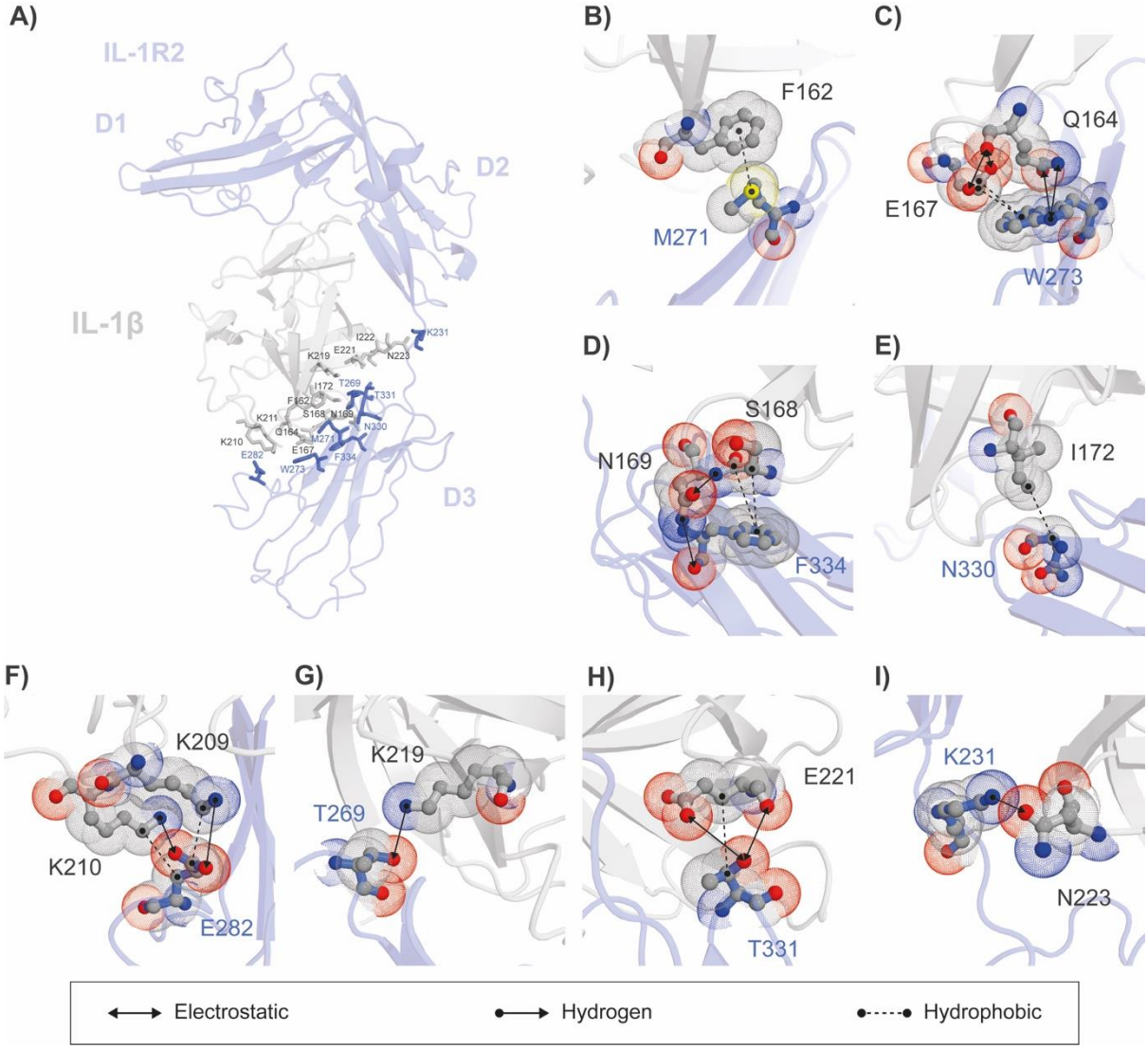

Figure 2.7 – Main interactions between mutated IL-1β residues and IL-1R2. The most likely electrostatic, hydrogen and hydrophobic interactions are shown. **A)** Relative position of the mutated residues and their binding partners in the IL-1β-IL-1R2 complex (PDB 3O4O). **B-I)** Close-up on each interaction. Colour code for dotted atoms: C, grey; N, blue; O, red; S, yellow.

As explained in the next section, the nature of these interactions guided the choice for the substitutions implemented through the design protocol.

2.2.2. Energy minimisation simulations

Implemented through Rosetta modelling suite[60] version 3.10, the design protocol followed a fixed-backbone,[61] property-guided approach (see section 1.4.2.1) in which residues engaged primarily in hydrophobic interactions with IL-1R2 (F162 and I172) were allowed to mutate only into polar amino acids (R, H, K, D, E, S, T, N, Q, G, P);

those forming directional H-bonds (Q164, S168, N169, N223) into non-H^+ donors/acceptors only (R, K, D, E, G, A, I, L, M, F, V); and, finally, those involved into ionic interactions (E167, K209, K210, K219, E221) were allowed to mutate only into non-polar amino acids (S, T, N, Q, G, P, A, I, L, M, F, Y, V, see previous section). I222, which does not interact directly with IL-1R2 was allowed to mutate into non-H^+ donors/acceptors only to better accommodate substitutions into positions 221 and 222. Cysteine and tryptophan were disallowed in all cases. These instructions were parsed to the program via a resfile (reproduced in Appendix A3).

Design was performed via "FastDesign" mover as part of a "GenericMonteCarlo" loop of 5 cycles. The fold tree was kept static through all cycles, although backbone (Φ and Ψ) and side chain (X_1 and X_2) torsion angles were allowed to move. REF15[62] with default terms was chosen as the score function. In addition to total energy score, nine other filters were applied to each cycle of the loop:

1. C_α RMSD for the full-length protein (threshold = 2.0 Å). By limiting backbone RMSD to $\leq$ 2.0 Å, this filter prevented the output of mutants affected by major structural distortions, a common result of lever arm effect.[63]
2. C_α RMSD for the RBS (threshold = 1.8 Å). This backbone RMSD filter was applied on the receptor binding site only. It controlled more tightly the structural fidelity of the RBS, an important area for generation of neutralising responses.
3. C_β RMSD for the RBS (threshold = 2.3 Å). Also aimed at improving structural fidelity (consequently, neutralising cross-reactivity), this filter limited to 2.3 Å the maximum amplitude of side chain movement for residues in the RBS.
4. Unsaturated buried H-bonds (24). This filter limited to 24 the maximum number of potential H-bonds not formed in the interior of the designed proteins, thereby preventing the output of likely unstable mutants.

5. Secondary structure (threshold = 0.95). This filter aborted the output of mutants which secondary structures differed from those of the native cytokine by more than 5 %.
6. Packing statistics (threshold = 0.65). This filter prevented the output of poorly packed structures. 0.65 is the recommended threshold.
7. Holes (threshold = 1.0). This filter measured, relatively to the crystal structure, the extension of solvent-accessible voids in the interior of the designed mutants, aborting the output of those with significantly larger internal pockets (> 1.0).
8. Total buried surface area (23,800 $Å^2$). By limiting the total surface area of the residues buried in the core of the muteins to a maximum of 23,800 $Å^2$ (only 315 $Å^2$ higher than that of the crystal structure), this filter also prevented the output of poorly packed mutants.

The Rosetta script containing these instructions is reproduced in Appendix A4. The results of the simulations are discussed in section 2.3.2.

2.2.3. Molecular dynamics simulations

To predict their overall structural stability, a small set of selected designs (see section 2.3.1) were subjected to molecular dynamics (MD) simulations at NPT (constant concentration, pressure, and temperature) conditions. These simulations were implemented via Gromacs[64] single precision version 2020.1 using Amber99SB-ILDN force field[65]. A system containing each protein to be simulated was set in a dodecahedron box with walls 2.0 nm larger than the longest dimension of the protein. It was then solvated with TIP5P water model[66] and neutralised with 150 mM NaCl. Parameter files for each step of the simulation are reproduced in Appendix A5.

Using a steepest descent integrator running at 10.0-fs steps, the system was energy-minimised to a maximum intermolecular force of 1,000 $kJ \cdot mol^{-1} \cdot nm^{-1}$. Short-range interactions were calculated with Verlet lists of maximum energy drift of 0.005

$kJ \cdot mol^{-1} \cdot ns^{-1}$ per particle (periodic boundary conditions were applied in all directions). A distance cut-off of 1.0 nm was set for calculation of van der Waals potentials. Finally, long-range electrostatic forces were calculated by particle-mesh Ewald (PME) running in a Fourier space of order 4 and grid dimensions of 0.1 nm. Bonds were not constrained in this step.

Prior to being submitted to production simulations, the system was stabilized in NVT (constant concentration, volume, and temperature) ensemble at 300 K for 100 ps. The temperatures of the protein and the solvent were coupled separately by velocity rescaling in intervals of 0.1 ps. Covalent bonds were constrained by Linear Constraint Solver (LINCS) with coupling matrix expansible up to order 4. Finally, the simulation was performed using a leap-frog integrator running at 2.0-fs steps for a total of 100 ps.

The system was further equilibrated in NPT ensemble also at 300 K for 100 ps. For that, isotropic pressure coupling was performed by the Parrinello-Rahman method with τ_P of 2.0 ps, P_{ref} of 1.0 bar and κ_T of $4.5 \cdot 10^{-5}$ bar^{-1}. These same parameters were applied in the production simulation, this one run for 100 ns in 0.01 ns-steps (i.e., total of 10,000 steps). The results of these simulations are discussed in section 2.3.2.

2.3. Results & discussion

2.3.1. Sequence generation and design selection

From the 25,000 cycles of design the production energy sampling simulation was set to run, 21,793 (≈ 81 %) passed the filters and generated decoy structures that were scored, additionally to the default parameters of the score function, for: C_α RMSD for both the full-length protein and for the receptor binding surface (RBS); presence of solvent- accessible pockets (holes) in the structure; unsaturated H-bonds; total buried surface; and total exposed surface for hydrophobic residues only (a description of each of these filters can be found in section 2.2.2). The results of these calculations are

illustrated in Figure 2.8, below, with a comparison between the selected designs (blue dots) and the native cytokine (orange dot).

Regarding minimum total energy, Figure 2.8 shows that most decoy structures scored slightly better than the crystal structure of the cytokine (-459 REU after relaxation), demonstrating the capacity of the program to search for the least-disrupting combinations of mutations within the range limited by design. Although -16 REU is not enough to predict superior biophysical properties (i.e., thermostability), a maximum of -465 REU (horizontal dotted lines) was set as a threshold for selection of the designs to be submitted to ML and MD simulations.

Another parameter assessed after the energy sampling simulations was the backbone RMSD for the full-length proteins. Figure 2.8A shows how C_α RMSD varies across all structures, including that of the crystal structure of the native cytokine, which diverted from the relaxed structure by ≈ 0.8 Å after relaxation. This difference was expected, as several cycles of energy minimisation invariably led to small structural distortions. Interestingly, though, diverted less than 0.2 Å from the native structure, which suggests that the mutations had almost no effect on the overall structure of the cytokine.

Similar observations can be made for residues in the receptor binding site (RBS) only. As Figure 2.8B shows, C_β RMSD varied by no more than 0.4 Å between the native cytokine and the majority of the designed mutants. This result suggests that the predominant orientation of the residues in close contact with the receptor was not affected by the mutations, therefore not influencing the binding properties of the selected mutants (section 2.1.1).

A third parameter applied as a filter in the design simulations detected the appearance of internal holes in the structures of the designed proteins, usually as a result of major structural distortions. This seems to have been the case here, as the majority of the decoy structures scored less than the relaxed structure of native IL-1β (Figure 2.8C), suggesting that, overall, the design process slightly improved the compactness of the protein.

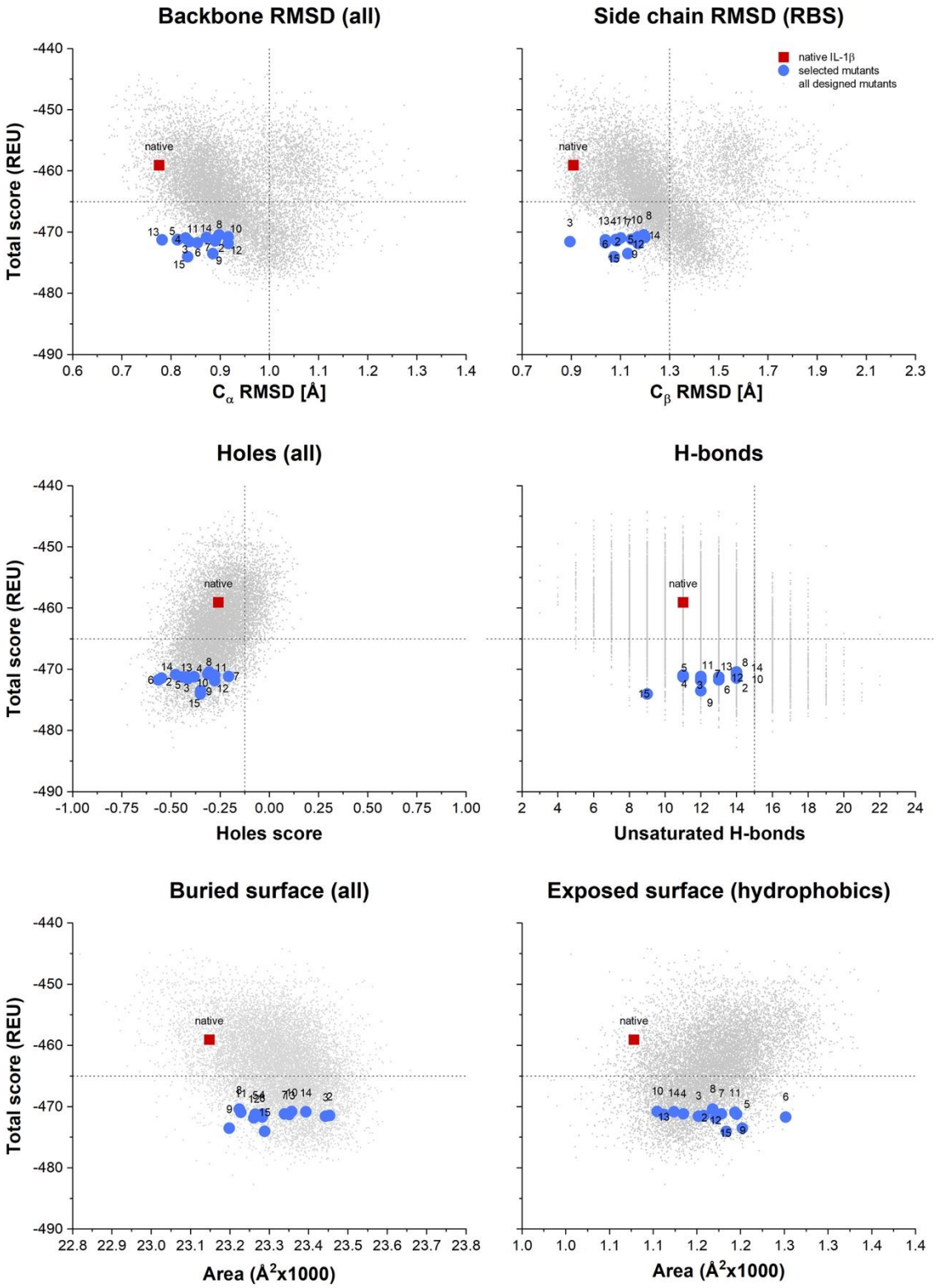

Figure 2.8 – **Rosetta scores.** Results of the reporter filters comparing the native cytokine (orange square) and the selected mutants (blue circle) with the entire pool of decoy structures (grey dots). RMSD scores were calculated with the crystal structure as reference. Dotted lines represent the thresholds used for selecting the best mutants.

Another interesting measure of the quality of the designed structures is their number of unsaturated H-bonds. These are potential hydrogen interactions that do not form due to structural modifications, usually resulting in decrease of overall structural stability. Figure 2.8D shows that the relaxed structure of native IL-1β has 11 unsaturated H-bonds, 3 less than the highest number found for the selected decoy structures. This difference, however, is still in the error range for this filter and should not suggest any loss of stability.

An additional measure of structural compactness is the total surface area of the buried residues (Figure 2.8E). As with holes and unsaturated H-bonds, this parameter seems not to have a strong correlation with total energy score, so that values for the selected designs are spread over a range of ≈ 400 $Å^2$ (≈ 1 % of total buried area).

Similar result was observed for the total surface area of exposed hydrophobic residues (Figure 2.8F). Conceived to predict the formation of hydrophobic pockets on the surface of the designed proteins, this filter also resulted in high variability (up to 30 % between native IL-1β and the selected mutants), although in this case it can be attributed, at least in part, to substitutions of hydrophilic residues.

Not illustrated in Figure 2.8, the final selection criterium concerns the trajectory of design, i.e., the distinct groups of mutations Rosetta randomly chooses to start a cycle of energy minimisation. No more than two decoy structures of the same trajectory were selected for MD simulations, a way to ensure their diversity and distinct binding properties. In total, 14 designs (IL-1b-02 to IL-1b-15) were selected for subsequent analysis.

Table 2.1 – **Sequence of wildtype IL-1β and selected designs.** Truncated sequences of IL-1β and selected designs. Mutations highlighted in bold.

ID	Sequence
IL-1β	M[117-160]SMS**F**V**Q**GE**ESN**DK**I**PVA[176-205]YPK**KK**MEKRFVFN**K**I**EIN**NKL[227-269]HHHHHHGGSC
IL-1b-02	M[117-160]SMS**D**V**R**GE**WDK**DK**R**PVA[176-205]YPK**YD**MEKRFVFN**L**I**YKD**NKL[227-269]HHHHHHGGSC
IL-1b-03	M[117-160]SMS**E**V**K**GE**WDK**DK**K**PVA[176-205]YPK**LD**MEKRFVFN**LI****FKD**NKL[227-269]HHHHHHGGSC
IL-1b-04	M[117-160]SMS**D**V**K**GE**WDK**DK**Q**PVA[176-205]YPK**WD**MEKRFVFN**L**I**YKD**NKL[227-269]HHHHHHGGSC
IL-1b-05	M[117-160]SMS**E**V**K**GE**WDK**DK**N**PVA[176-205]YPK**YD**MEKRFVFN**LI****FKD**NKL[227-269]HHHHHHGGSC
IL-1b-06	M[117-160]SMS**D**V**K**GE**WDK**DK**R**PVA[176-205]YPK**LD**MEKRFVFN**L**I**YVD**NKL[227-269]HHHHHHGGSC
IL-1b-07	M[117-160]SMS**D**V**K**GE**WDK**DK**Q**PVA[176-205]YPK**WD**MEKRFVFN**L**I**YKD**NKL[227-269]HHHHHHGGSC
IL-1b-08	M[117-160]SMS**E**V**R**GE**WDK**DK**N**PVA[176-205]YPK**YD**MEKRFVFN**LI****FKD**NKL[227-269]HHHHHHGGSC
IL-1b-09	M[117-160]SMS**E**VKGE**WDK**DK**N**PVA[176-205]YPK**LD**MEKRFVFN**LI****FKD**NKL[227-269]HHHHHHGGSC
IL-1b-10	M[117-160]SMS**D**VRGE**WDK**DK**Q**PVA[176-205]YPK**YD**MEKRFVFN**L**I**YKD**NKL[227-269]HHHHHHGGSC
IL-1b-11	M[117-160]SMS**D**VKGE**WDK**DK**Q**PVA[176-205]YPK**LD**MEKRFVFN**L**I**YKD**NKL[227-269]HHHHHHGGSC
IL-1b-12	M[117-160]SMS**E**VRGE**WDK**DK**N**PVA[176-205]YPK**WD**MEKRFVFN**LI****FKD**NKL[227-269]HHHHHHGGSC
IL-1b-13	M[117-160]SMS**E**VKGE**WDK**DK**N**PVA[176-205]YPK**WD**MEKRFVFN**LI****FKD**NKL[227-269]HHHHHHGGSC
IL-1b-14	M[117-160]SMS**E**VRGE**WDK**DK**Q**PVA[176-205]YPK**YD**MEKRFVFN**LI****FKD**NKL[227-269]HHHHHHGGSC
IL-1b-15	M[117-160]SMS**E**VKGE**FDK**DK**Q**PVA[176-205]YPK**LD**MEKRFVFN**LI****FKD**NKL[227-269]HHHHHHGGSC

2.3.2. Conformational stability analysis of selected designs

In addition to the crystal structure of native IL-1β, the decoy structures of 14 designed mutants (selected according to the criteria described in the previous section) were subjected to MD simulations at NPT ensemble, as described in section 2.2.3. Figure 2.9 below illustrates the amplitude of backbone (C_α) RMSD for the selected models relative to the relaxed crystal structure of IL-1β used as design template.

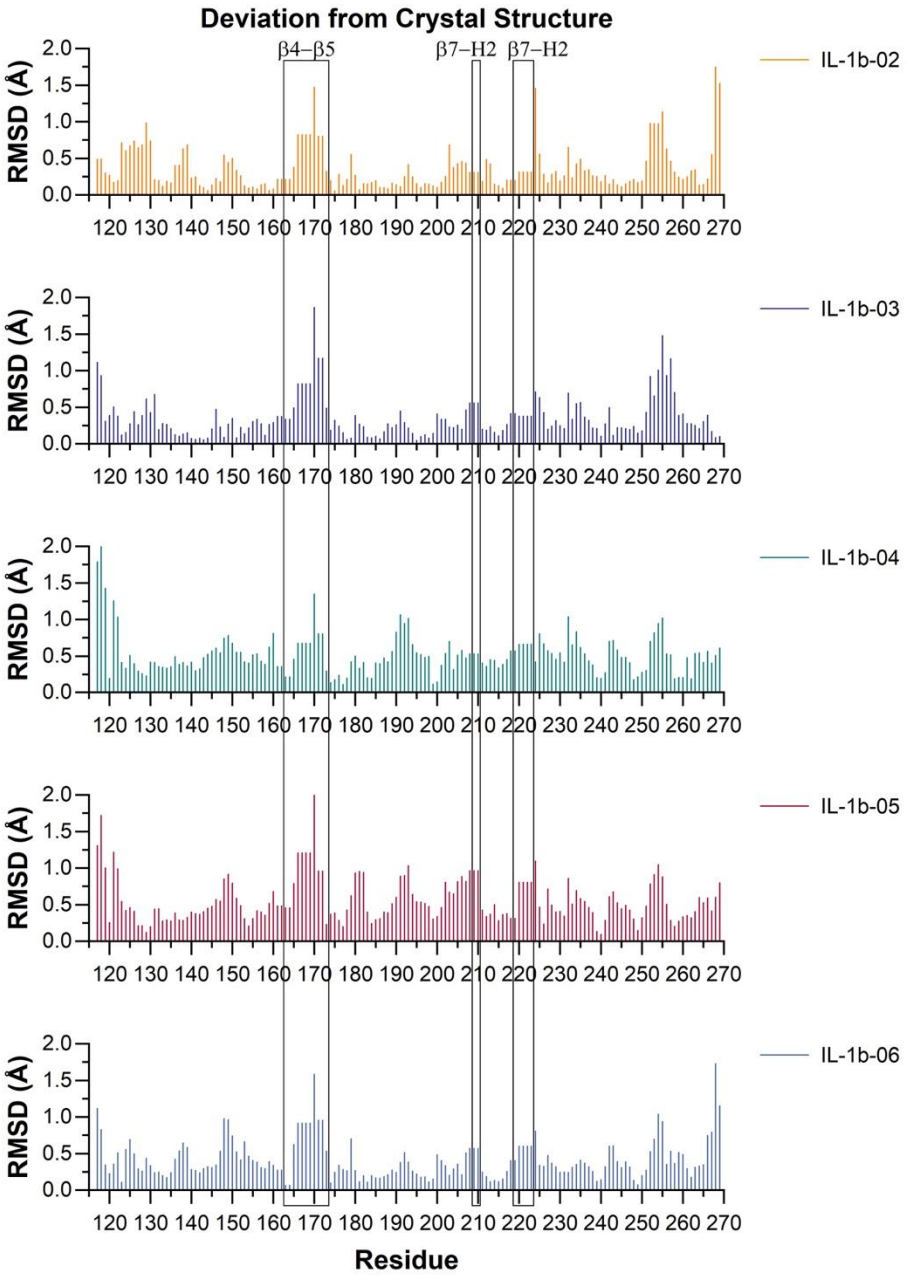

Figure 2.9 – Amplitude of backbone RMSD for selected models. Maximum backbone (C_α) RMSD calculated with reference to the relaxed crystal structure of IL-1β. Black rectangles indicate mutated segments.

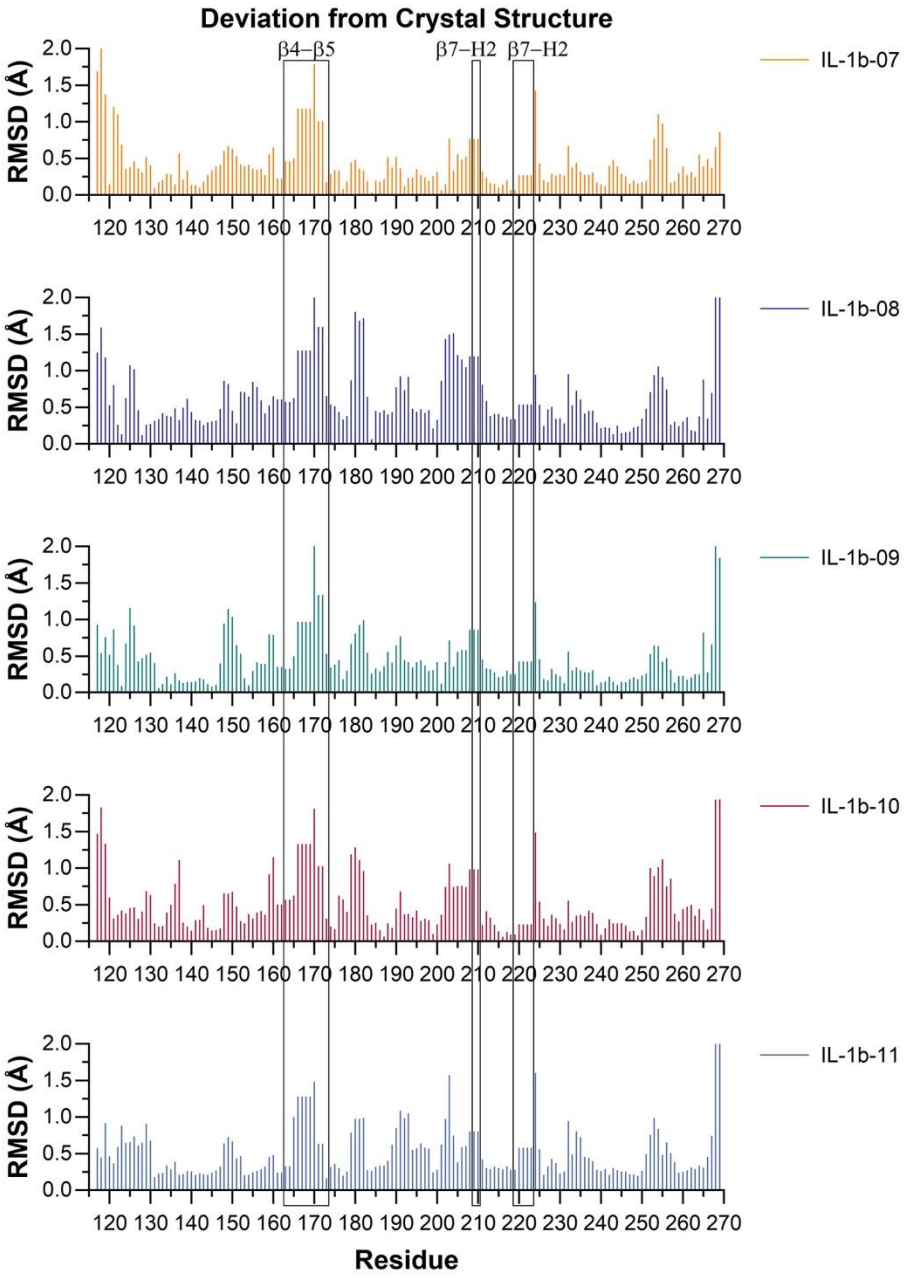

Figure 2.10 – Continuation.

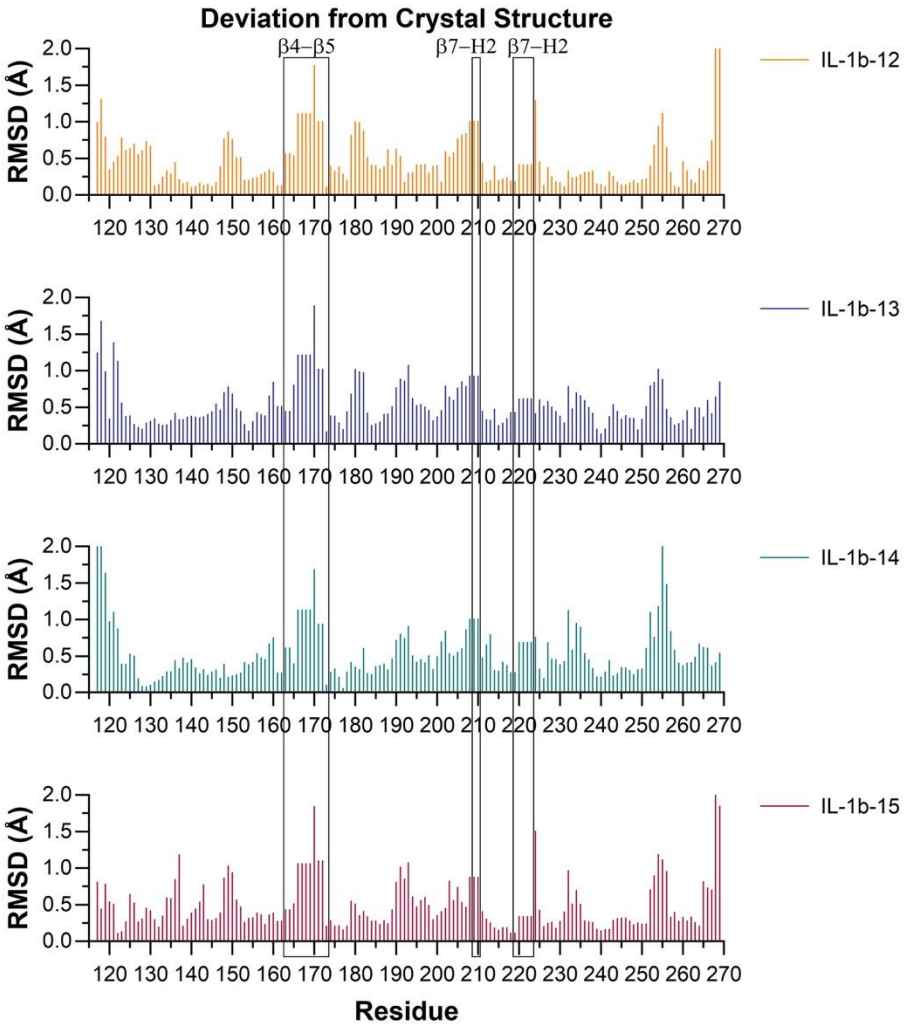

Figure 2.11 – Continuation.

These results indicate that both the native cytokine and designed mutants are remarkably stable at ordinary conditions of temperature (300 K, or 26.85 °C) and pressure (1.0 bar, or 0.99 atm), with average C_α RMSD (calculated from 1.0 to 100.0 ns) oscillating around 1.5 Å. More interestingly, these results are consistent across all models, suggesting that the designed mutations had minimal effect on their conformational stability in solution, even around the mutated segments.

2.4. Conclusions

This chapter described in depth the methodology conceived for the *in-silico* design of improved IL-1β-based antigens, a computational framework consisted of two major steps: sequence generation (driven by stochastic energy minimisation); and stability

analysis (performed on results of molecular dynamics simulations). Despite being devised as an iterative process of design and refinement, this pipeline yielded satisfactory results were obtained from the first production simulations, as summarised below.

In the first step, ≈ 81 % of a total of 25,000 generated sequences passed a set of stringent filters embedded in the design protocol (section 2.2.2). This large proportion suggests a high tolerance for IL-1β to receive surface modifications, particularly in the flexible segments that form its outermost structure (section 2.1.1). The calculations performed by these filters show most of the designed structures to deviate only slightly from IL-1β's, with backbone (C_α) and side chain (C_β) RMSD values, rarely surpassing 0.6 Å from that measured for the relaxed template structure (section 2.3.1). These filters also pointed to a tendency for the modified structures to assume a more compact conformation with lower numbers of solvent-inaccessible internal pockets. Finally, a significant increase in hydrophobicity of the exposed surface was also measured for the designed sequences.

Based on their structural features, 14 of the 21,793 models yielded by the production simulation on Rosetta were selected for assessment of their conformational stability by molecular dynamics (see section 2.2.3). With their RMSD and radius of gyration almost unaltered throughout the MD simulations (see section 2.3.2), the selected models displayed a level of conformational stability equivalent to that observed for the template structure under the same conditions, indicating that the overall structure of the cytokine was conserved in the designed muteins despite the large number of surface modifications. Considering this result, all 14 mutated sequences were selected for expression and biophysical characterisation.

Although these MD simulations assisted in asserting the likelihood of the designed sequences to retain their predicted conformations when exposed to the same conditions as IL-1β, they provided no additional information on the thermostability or tendency of the muteins to aggregate. Although feasible, measuring these properties via molecular

dynamics would require long and computationally costly simulations, hence all 14 sequences were selected for *in vitro* characterisation.

Chapter III. Biophysical characterisation of selected designs

3.1. Introduction

Despite the positive results obtained from the molecular dynamics simulations performed on the selected designs (described in chapter II, section 2.3.2), experimental verification of the binding properties, conformational accuracy, and thermodynamic stability of these muteins was required. To this end a number of biophysical assays were used. These easily obtainable measurements were instrumental for the rapid assessment of the initial design strategy and its implementation methods (which, as discussed in section 2.4, did not require refinement). They also provided the parameters for selection of the most promising candidates to be tested *in vivo*, greatly reducing the number of animals necessary for immunisation assays.

The first of these high throughput (HTP) *in vitro* screenings consisted in measuring, by biolayer interferometry (BLI), the binding affinities between canakinumab or gevokizumab and IL-1β or several IL-1β-derived mutant designs selected for expression and characterisation. Although aimed primarily at assessing the effects of the mutations on the integrity of the neutralising epitopes for the two clinically relevant monoclonal antibodies (mAbs), these assays (described in section 3.2.2.1) were also conceived as a quick way of screening for grossly misfolded muteins, which would result in aberrant binding kinetics. Interestingly, the results discussed in section 3.2.2.1 showed that all the expressed muteins (IL-1b-02 to IL-1b-15) bind the Fab fragments of both mAbs with similar kinetics as that of unmodified IL-1β, which provided experimental evidence that the designed mutations did not significantly affect the overall structure of the template protein, in particular these two neutralising epitopes.

The second HTP-BLI screening (also described in section 3.2.2.1) focused on determining the binding affinity between IL-1β or the expressed muteins and the soluble form of type 2 IL-1 receptor (sIL-1R2), an important parameter for evaluating the relative success of the design strategy. The results (also discussed in section 3.2.2.1) showed

that all but three (IL-1b-02, IL-1b-06, and IL-1b-07) of the mutants interacted with the receptor with an affinity of ≈ 3-4 orders of magnitude lower than that of the WT cytokine (K_D ≈ 0.5-1.0 nM and K_D ≤ 1.0 pM, respectively). With values of K_D considered low enough to bypass the inhibitory effects of sIL-1R2 *in vivo*, three muteins, IL-1b-09, IL-1b-13, and IL-1b-15, were selected for further biophysical characterisation, including measurements of melting temperature (T_m) and chemical shift perturbation (CSP).

The T_m of a protein is the median temperature at which it undergoes a major conformational change resulting from heat-induced denaturation.[67] It is an easy-to-acquire measurement of thermostability, frequently employed in assessing the tendency of some proteins to unfold or aggregate when exposed to non-native conditions. In this sense, to evaluate the impacts of the surface modifications on the conformational stability of the selected muteins, their T_ms were determined (as described in section 3.2.2.2) and compared with that of the native cytokine. Interestingly, the results of these assays (discussed in section 3.3.3) showed IL-1b-13 and IL-1b-15 to be similarly stable, with their T_ms differing from IL-1β's by only 1.2 ± 1.0 °C. IL-1b-09, on the other hand, appeared to have suffered a significant loss in thermostability, with its T_m varying by -3.9 ± 1.4 °C). The potential implications of these findings on the immunogenicity of the muteins are discussed in section 4.4, chapter 4.

Using 2D nuclear magnetic resonance spectroscopy (NMR), the conformational accuracy of five selected muteins were analysed at atomic resolution, as described in section 3.2.2.3. As anticipated, the results of these analyses revealed only minimal structural disparities, that occurred at the immediate vicinity of the mutated segments, with no significant backbone movement detected in the rest of the structure (irrespective of core or surface). By demonstrating that the selected muteins assumed IL-1β's native conformation, these results (discussed in section 3.3.4) confirmed that the differences observed in their binding affinities for sIL-1R2 were due solely to the nature of the substitutions, not to longer range structural changes caused by them. This high level of

conformational fidelity may very likely be the reason the polyclonal antibodies raised against the muteins cross reacted almost perfectly with the non-mutated areas of the cytokine (including part of its interface with sIL-1R1, see section 4.3.2 of chapter IV). Collectively, these results appear to confirm the success of the design protocol in maintaining high levels of cross-reactivity between the muteins and the wildtype cytokine.

3.2. Materials & methods

3.2.1. Gene cloning, protein expression and purification

3.2.1.1. Native IL-1β and selected muteins

Sequences of native IL-1β and selected designs flanked by an initiator methionine and a C-terminal hexahistidine fused to a GGSC tag (peptide designed to facilitate chemical cross-linking with virus-like particles, see below) were back translated and codon-optimised for expression in *Escherichia coli*. These constructs were then synthesised and cloned (via NcoI/XhoI restriction-ligation sites) by Twist Biosciences (San Francisco, CA – USA) into the publicly available pET-28a(+) vector. DNA purification and verification by next-generation sequencing (NGS) were also performed by the company.

After resuspension in nuclease-free water, the plasmids were transformed into T7 Express competent *E. coli* cells (New England Biolabs, Ipswich, MA – USA) according to the recommended protocol. The transformed cells were then pre-cultured overnight (ON) in 30 mL of LB medium containing 100 $\mu g \cdot mL^{-1}$ of kanamycin at 37 °C and 200 rpm in a 1.0” orbital shaking incubator. The next morning, the cultures were scaled up to 500 mL with the same medium and left to grow at the same conditions for 2 h 30 min (time to reach the mid-point of the log phase, measured in growth dynamics assays). At this point, IPTG was added to a final concentration of 1.0 mM, after which the temperature was lowered to 18 °C (determined in expression optimisation assays) for ON incubation. The following day, the cells were harvested and pelleted by centrifugation at

4,500 g for 15 min. The pellets were then resuspended in 40 mL of lysis buffer (10 mM HEPES pH 7.5; 500 mM NaCl; 0.5 mM TCEP; 25 $U \cdot mL^{-1}$ benzonase; 50 $U \cdot mL^{-1}$ lysozyme) and incubated for 30 min at room temperature (RT) under mild agitation. After the addition of 5 mL of 10 % v/v triton X-100 (1% v/v final concentration), the cells were incubated again for 30 min at the same conditions. Lysis was completed with a single cycle of freezing at -80 °C and thawing at RT, followed by centrifugation at 25,000 g for 30 min.

Proteins were initially purified by nickel ion metal affinity chromatography (IMAC) using His-GraviTrap disposable columns (Cytiva, Uppsala, Sweden). Briefly, the columns were equilibrated with 10 mL of binding buffer (10 mM HEPES pH 7.5; 500 mM NaCl; 20 mM imidazole; 0.1 % triton X-100), loaded with the lysates and washed with 10 mL of the same buffer. Moved to new tubes, these columns were then eluted with 3 mL of IMAC elution buffer (10 mM HEPES pH 7.5; 500 mM NaCl; 500 mM imidazole). Finally, excess salt and imidazole were removed from the eluates by size-exclusion chromatography (SEC), using PD-10 disposable desalting columns (Cytiva). This process started with the columns being equilibrated with 10 mL of storage buffer (10 mM HEPES pH 7.5; 150 mM NaCl; 5 % glycerol), after which the samples were loaded and immediately eluted with 6 mL of the same buffer. Finally, to ensure maximum accuracy of the binding assays and biophysical characterisation of the different mutants, the proteins were further purified by SEC against phosphate buffer saline pH 7.4 (PBS) using a Sephadex75 Increase 10/300 GL prepacked column (Cytiva). In each step, the proteins were checked for purity and concentration via sodium dodecyl sulphate–polyacrylamide gel electrophoresis (SDS-PAGE) and bicinchoninic acid (BCA) protein quantitation assay (ThermoFisher, Waltham, MA – USA), respectively. The results of these assays are discussed in section 3.3.1.

3.2.1.2. IL-1 receptors and anti-IL-1β monoclonal antibodies

For the IL-1 receptors, three constructs were designed to express a μ-phosphatase signal peptide (SP) followed by the ectodomains of either IL-1R1, IL-1R2 or IL-1R3.

These sequences were then C-terminally fused to a tobacco etch virus (TEV) protease site for optional cleavage, followed by an AviTag biotin-acceptor peptide (BAP) for *in vivo* biotinylation, and a terminal C-tag (EPEA) for immunoaffinity purification. The resulting sequences were then synthesised and cloned (via NotI/XbaI restriction-ligation sites) by Twist Biosciences into their proprietary vector pTwist-CMV-BetaGlobin-WPRE-Neo. Similarly, genes coding for the light and heavy chains of anti-IL-1β mAbs (both full-length and Fab fragments of hκIgG1) fused to an IL-2 SP and a C-tag were codon-optimised for low GC content, synthesised, and cloned into pTwist-CMV-BetaGlobin-WPRE-Neo vector by Twist. In both cases, plasmid purification and NGS sequencing were also performed by the company.

Upon arrival, these plasmids were directly transformed into DH5α *E. coli* cells (New England Biolabs), amplified, and purified by midiprep with an additional endotoxin removal step (Zymo Research, Irvine, CA – USA). Transfection into HEK293F cells was carried out using the Expi293 system as instructed by the manufacturer (ThermoFisher), with sIL-1R1 and sIL-1R2 constructs co-transfected with a BirA-coding vector for *in vivo* biotinylation through their AviTag BAP. The cells were then incubated in Erlenmeyer flasks gently shaken (125 rpm) at 37 °C in presence of 8 % CO_2. Expression enhancers were added 16 hours post transfection, with the supernatants harvested 56 hours later by centrifugation at 4,000 g for 10 min.

All proteins expressed by this method were purified by immunoaffinity chromatography (IAC) followed by SEC. Briefly, these proteins were recovered from the supernatants by immunoaffinity using a CaptureSelect CtagXL column (ThermoFisher) with PBS running buffer according to the manufacturer's instructions. Following isocratic elution with 2.0 M $MgCl_2$, the protein-containing fractions were immediately loaded into a Sephadex200 Increase 10/300 GL prepacked SEC column (Cytiva) running on PBS. The major absorption peaks were then collected and analysed by SDS-PAGE for purity assessment. The results of these assays are also discussed in section 3.3.1.

3.2.2. Biophysical characterisation of expressed muteins

3.2.2.1. Protein-protein interaction assays

As an initial check for conformational accuracy, binding affinity of IL-1β and the 14 designed muteins (IL-1b-02 to IL-1b-15) for the Fab fragments of canakinumab and gevokizumab were measured by BLI using an Octet RED96e interferometer (Sartorius, Wokingham RG – UK). Briefly, anti-5xHis HIS1K sensors (Sartorius) were loaded until saturation (t = 180 s) with either the native cytokine or the designed mutants diluted to 25 $\mu g \cdot mL^{-1}$ in kinetic buffer (KB, composed of 0.02 % Tween 20 and 0.1 % BSA in PBS). After a 60 s-baseline with KB, association was performed with the Fabs diluted 6x1:2 in KB, from 50.0 down to 1.6 nM. An extra well with buffer only was added for drift control. The 50 nM curve reached saturation within 300 s, after which dissociation was carried out in KB for 600 s. The results of this screening are discussed in section 3.2.2.1.

With a slightly modified set up, binding affinity measurements of native IL-1β and designed mutants for sIL-1R2 were also assessed by BLI. In this case, however, the receptor was immobilised on the tips, with the cytokine and muteins kept in solution. For that, streptavidin-coated SAX sensors (Sartorius) were loaded with biotinylated sIL-1R2 at 1 $mg \cdot mL^{-1}$ for 1,800 s, the point of saturation (higher concentration of ligand and longer loading time were necessary due the low biotin/sIL-1R2 ratio obtained from *in vivo* biotinylation). After a 60 s-quenching step with biocytin (ThermoFisher) dissolved in KB and a second baseline step with KB only, association was carried out for 600 s with the native IL-1β or designed mutants diluted 5x1:2 in KB, from 100 down to 6.25 nM. Here too an extra well containing KB only was added to account for drift (although no significant drifting was observed with these sensors). Finally, a 600 s dissociation step was performed with KB only. The results of this screening are also discussed in section 3.2.2.1.

3.2.2.2. Differential scanning calorimetry

To assess the effects of the designed mutations on the cytokine's thermostability, melting temperatures of both native IL-1β and selected mutants were determined by differential scanning calorimetry coupled to circular dichroism spectroscopy at the far UV range (CD-DSC). As a preparation for these measurements, the proteins were dialysed in 10 mM sodium phosphate buffer pH 7.8 and concentrated to ≈ 250 $\mu g \cdot mL^{-1}$ (higher concentrations resulted in fast HT voltage saturation). Using a ChirascanV100 spectrophotometer (Applied Photophysics, Leatherhead – UK), absorption of polarised light in the far UV region (λ = 203 to 253 nm) was then measured for each protein at temperatures (T) ranging from 20 to 94 °C in 2 °C-step increase. Upon visual analysis of the resulting ellipticity-to-wavelength curves ($\theta_{(\gamma)}$), θ values obtained for three specific wavelengths (λ = 220, 225, and 230 nm) were extracted, normalised ($\tilde{\theta}_{(\gamma)}$) and plotted against the entire temperature range ($\tilde{\theta}_{(\gamma, T)}$). Finally, T_m values were calculated for each protein as the average of the inflexion points (T) of its three $\tilde{\theta}_{(\gamma, T)}$ curves. These results are discussed in section 3.3.3.

3.2.2.3. Nuclear magnetic resonance spectroscopy

For nuclear magnetic resonance spectroscopy (NMR) measurements of conformational accuracy, IL-1β, IL-1b-02, IL-1b-07, IL-1b-09, IL-1b-13, and IL-1b-15 were expressed in ^{15}N-enriched M9 minimum medium supplemented with trace elements, as well as biotin and thiamine (for a more detailed recipe, see Appendix A2), according to a procedure similar to the one employed for the expression of the cytokines in complex medium (see section 3.2.1.1). Minor adjustments to this protocol included extending the time to induction (3 h 20 min instead of 2 h 30 min), increasing the incubation temperature (20 °C instead of 18 °C), and delaying the time for IPTG induction (48 h instead of ON). The purification steps also followed the process described in section 3.2.1.1, with the difference that SEC was performed with low-salt buffer (LSB, 10 mM HEPES pH 7.4, 100 mM NaCl) instead of ordinary PBS. The purified cytokines were

concentrated to a minimum of 200 μM and stored at -20 °C until required. Whereupon they would be thawed and supplemented with 10 % D_2O (deuterium oxide, heavy water) prior to the NMR measurements.

These measurements were carried out in an 18.8 T (800 MHz 1H Larmor frequency) Bruker (Billerica, MA – USA) spectrometer equipped with a CPTC ^{1}H, ^{13}C, ^{15}N 5.0 mm cryoprobe and an Avance III console. ^{1}H-^{15}N heteronuclear single quantum coherence (HSQC) spectra were acquired with 256 increments in the indirect dimension and a relaxation delay of 1.0 second, with 8-64 scans depending on concentration and spectral quality. All spectra were acquired and processed using Bruker's Topsin 4.0 software and manually analysed using CCPN 3.0 suite.[68,69]

Backbone ^{1}H and ^{15}N assignments for IL-1β were retrieved from Driscoll *et al*, 1990[70] (BMRB entry 435), and transferred, via pH/T titration, to a new spectrum collected at pH 7.27 and temperature of 298 K. These conditions were also applied to the measurement of ^{1}H-^{15}N HSQC resonances of the five muteins mentioned above, which allowed for the assessment of their conformational accuracy via chemical shift perturbation analysis (a method through which the movements of a residue's peak in the ^{1}H-^{15}N plane are traced as the environmental conditions change. For further information, see Williamson's review on CSP[71]). The results of this analysis are discussed in section 3.3.4.

3.3. Results & discussion

3.3.1. Mutein expression

To address potentially deleterious effects of the extensive surface modifications on the expression of the cytokine, some special filters were added to the design protocol to restrict the output of the program to only muteins with hydrophobicity profiles similar to IL-1β's (see section 2.2.2). As a way of validating this strategy, all selected designs (IL-1b-02 to IL-1b-15) were expressed under the exact same conditions as those

established for the template protein (see section 3.2.1.1), with their yields compared after complete purification. Interestingly, no significant differences were observed in the yields of the 15 antigens (achieving ≈ 15 mg of protein per litre of cell culture, as estimated by BCA quantitation after SEC). This result confirms the effectiveness of the design strategy in preserving the solubility of the WT cytokine across the muteins.

As illustrated in Figure 3.1, all muteins eluted at retention volumes almost identical to that of the template protein (13.1-13.9 mL, measured in a Superdex 75 column), indicating that the modifications carried out on IL-1β's surface also had minimal impact on its hydrodynamic profile as judged by SEC. This result corroborates the assumption that any differences observed in the binding properties of the cytokines (wildtype and muteins, see next section) are not a product of gross changes in their biophysical properties (e.g., hydrophobicity), an unlikely but real possibility in BLI assays.

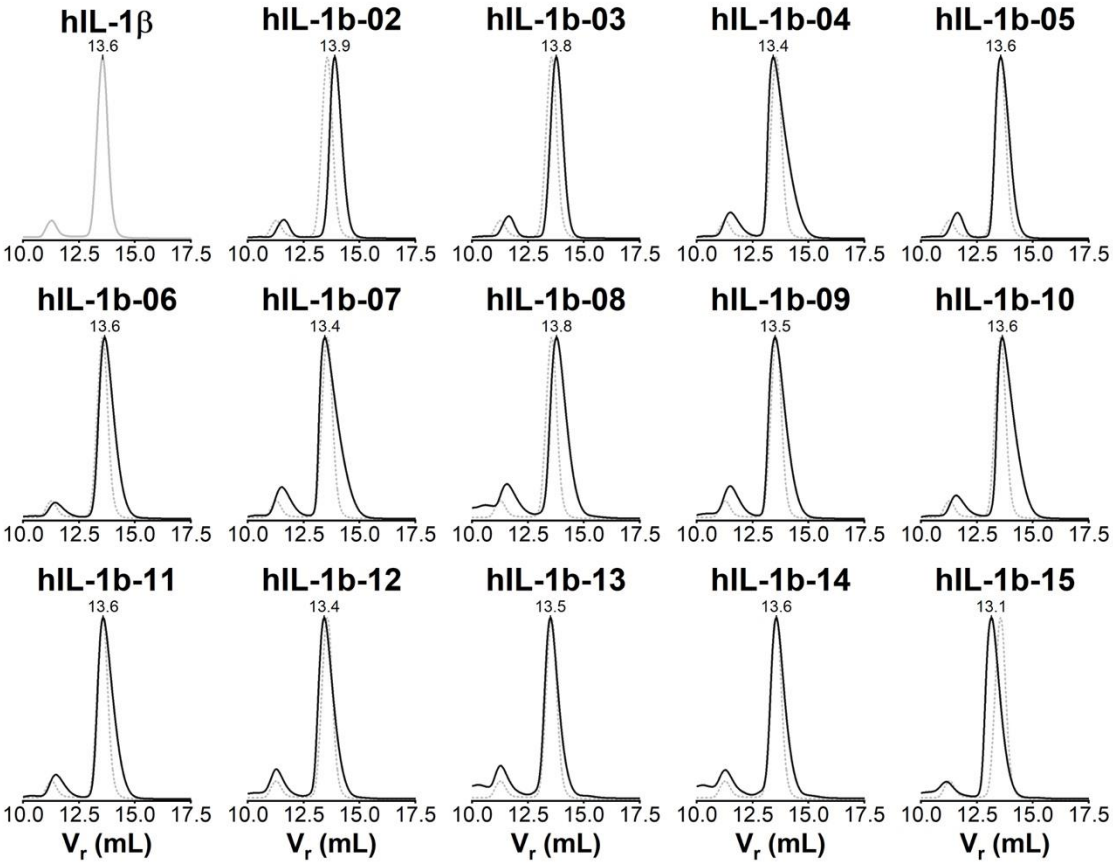

Figure 3.1 – SEC purification of IL-1β and expressed muteins. Normalised absorbances (280 nm) obtained for wildtype IL-1β (grey solid line in top-left panel, and grey dotted lines in the remaining panels) and designed muteins (black solid lines) in SEC purifications performed in a Superdex 75 column. Each peak is annotated for its respective retention volume (V_r).

Figure 3.1 also shows that a small amount of host proteins (short peaks between 10.0 and 12.5 mL) co-eluted with the tagged proteins (larger peaks between 12.5 and 15 mL) in the initial affinity purification. Most of these impurities were removed by high-resolution fractionation, in which only the fractions collected at the centres of the target peaks (≈ 75 % AUC) were submitted to subsequent analysis. As demonstrated by the SDS-PAGE reproduced in Figure 3.2, this procedure resulted in ≈ 98% purity for all proteins.

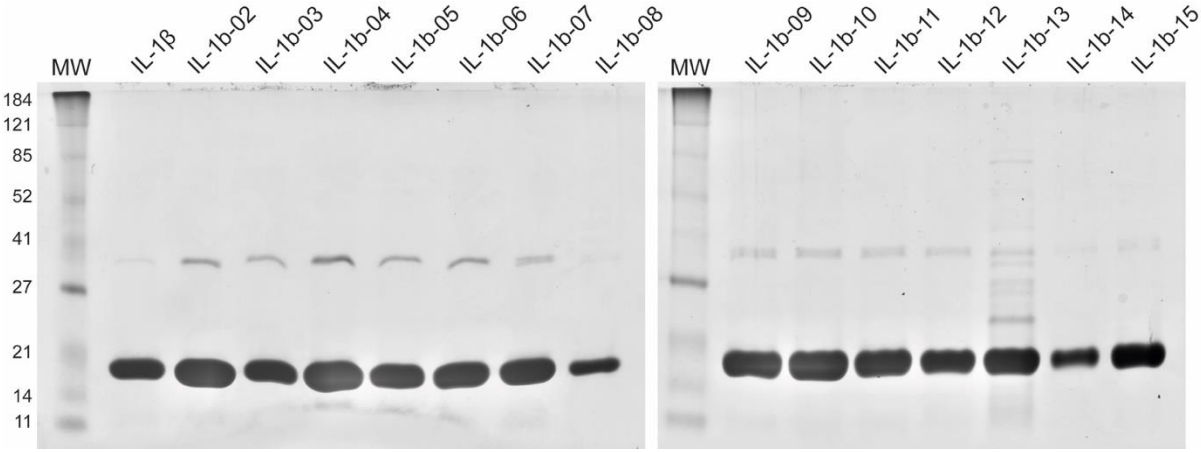

Figure 3.2 – SDS-PAGE of IL-1β and the 14 muteins. Expected molecular weight of ≈ 18 kDa. The samples were overloaded for better visualisation of impurities. MW, molecular weight marker.

Given that all proteins expressed with similar yields, and no significant changes in hydrodynamic behaviour was observed, the 14 muteins were selected for BLI screenings to evaluate their binding properties for canakinumab (CKB), gevokizumab (GKB), and sIL-1R2 (see section 3.2.2.1).

Expression of the mAbs and receptors in mammalian cells (see section 3.2.1.2) produced more heterogeneous results than those obtained for IL-1β and the muteins in *E. coli*. While the full-length hκIgG1 chains of CKB and GKB yielded ≈ 0.8 and ≈ 25 mg of purified protein per litre of cell culture ($mg_{prot.} \cdot L_{cult.}^{-1}$), respectively, the Fab fragments of the same mAbs expressed in the same system under the same conditions both resulted in yields of ≈ 30 $mg_{prot.} \cdot L_{cult.}^{-1}$. The sIL-1R1, sIL-1R2 and sIL-1R3 all expressed with similar efficiency, in the range of ≈ 40-50 $mg_{prot.} \cdot L_{cult.}^{-1}$. No aggregation and/or precipitation occurred during purification of the mAbs and receptors. Purities

after SEC were estimated in the order of ≈ 99 % for the mAbs and ≈ 95 % for the receptors, with some host proteins appearing to elute with the recombinant candidates.

3.3.2. Binding properties

The first two of the BLI assays described in section 3.2.2.1 measured the binding affinities of the Fab fragments of canakinumab (CKB) and gevokizumab (GKB) for IL-1β and all the 14 expressed muteins, which resulted in the sensograms illustrated on Figure 3.3 and Figure 3.4 below (measurement statistics listed in Appendix A6).

It is apparent from these results that the two mAbs interact differently with IL-1β and its designed muteins. An analysis of the association phase of these interactions shows canakinumab to bind the ligands significantly faster than gevokizumab, with association rates (k_{on}, filled vertical bars on Figure 3.5) averaging more than double those of GKB, although with greater variability ($2.90 \cdot 10^5 \pm 4.33 \cdot 10^4$ and $1.36 \cdot 10^5 \pm 1.98 \cdot 10^4$ $M^{-1}s^{-1}$, respectively). The opposite is observed for the dissociation rates (k_{off}, empty vertical bars on Figure 3.5), with CKB's varying less than gevokizumab's around a much lower average ($6.45 \cdot 10^{-4} \pm 1.17 \cdot 10^{-4}$ and $12.00 \cdot 10^{-4} \pm 5.13 \cdot 10^{-4}$ s^{-1}, respectively).

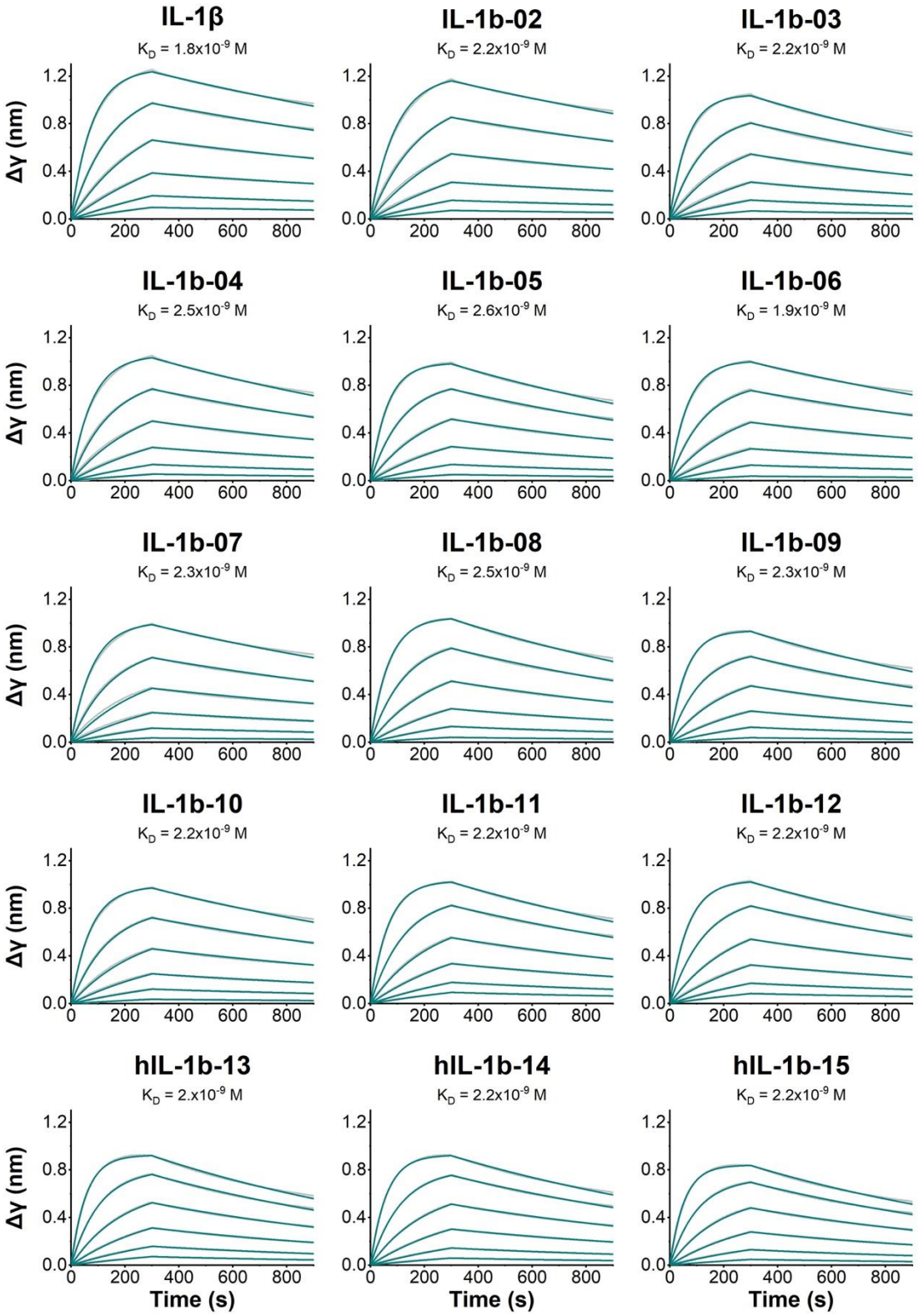

Figure 3.3 – Binding to canakinumab (CKB). Sensograms from an HTP-BLI assay performed with IL-1β or the selected muteins as ligands and canakinumab Fab fragment as analyte. From the highest to the lowest response: 50, 25, 12.5, 6.3, 3.1, and 1.6 nM of analyte.

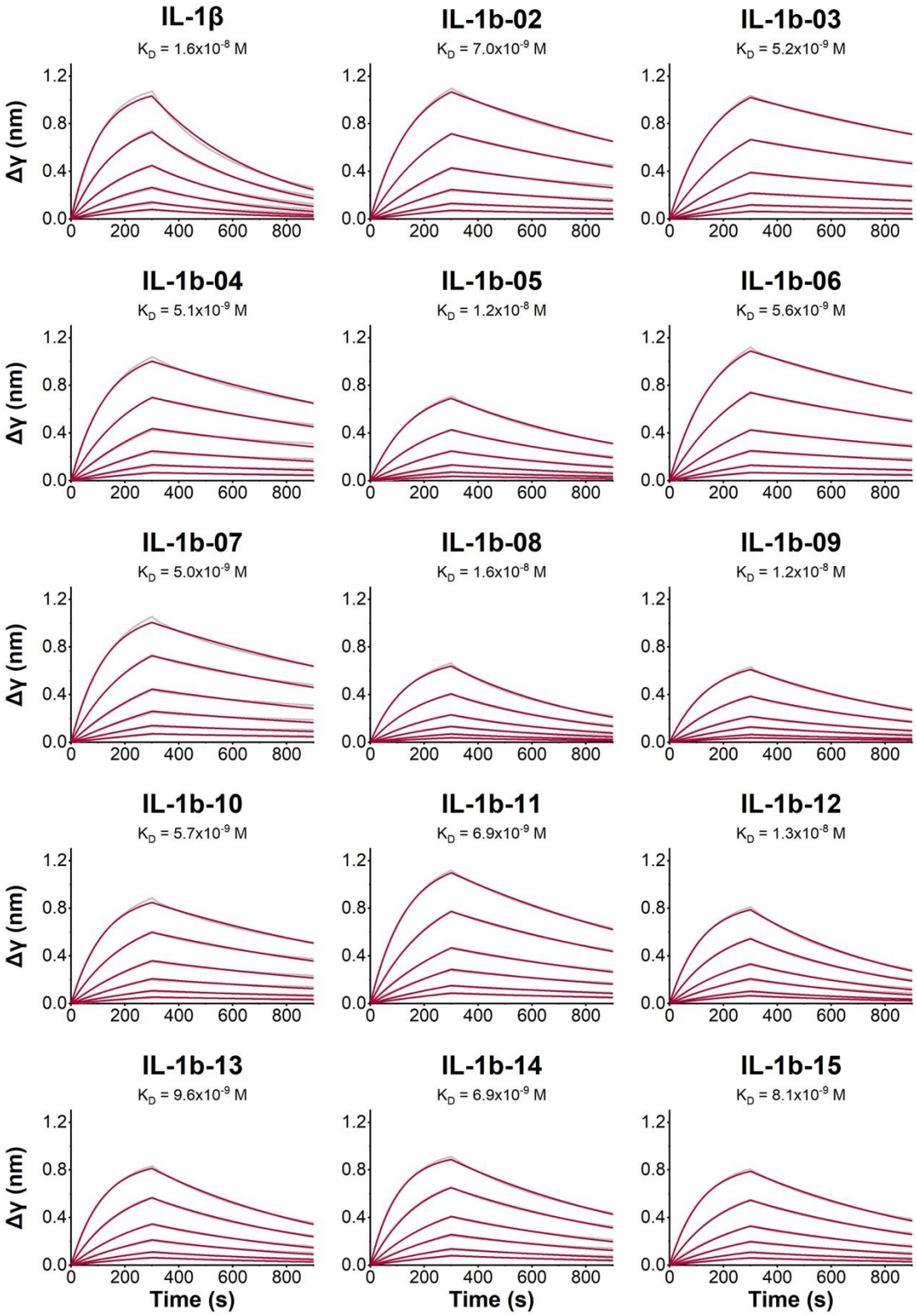

Figure 3.4 – Binding to gevokizumab (GKB). Sensograms from an HTP-BLI assay performed with IL-1β or the selected muteins as ligands and gevokizumab Fab fragment as analyte. From the highest to the lowest response: 50, 25, 12.5, 6.3, 3.1, and 1.6 nM of analyte.

Another difference in the kinetics of the two antibodies is related to their recorded maximum responses ($R_{(t, M)}$, Not to be confused with R_{max}, which is not dependent on time or concentration), measured at the limit of the association time for the highest concentration of analyte. Observing the equivalent peaks of the highest curves (50 nM) illustrated in Figure 3.3 and Figure 3.4, particularly at the association phase (symbols and lines in Figure 3.5), canakinumab's $R_{(300\ s,\ 50\ nM)}$ averaged slightly higher than gevokizumab's, however GKB's peak responses varied more broadly across the muteins (1.01 ± 0.10 versus 0.91 ± 0.17 nm, respectively). Considering that both assays were performed with ligands at the exact same concentration (25 $\mu g \cdot mL^{-1}$) and that there is no significant difference in the molecular weights of the two analytes (≈ 47 kDa), three hypothesis could explain the observed discrepancies. *i)* Loss in sensor capacity after multiple regenerations; *ii)* conformational disruptions at GKB's binding site; *iii)* differences in the nature of mutated residues.

As described in section 3.2.2.1, the HIS1K employed in the mAbs BLI screening were regenerated up to four times before being replaced by new ones. Therefore, a modest decline in $R_{(300\ s,\ 50\ nM)}$ (in fact, for any tested concentration at any timepoint) would be expected within each set of sensors (indicated by upper red brackets in Figure 3.5), and was observed for CKB. This tendency, however, is not clear for GKB, which exhibited abrupt declines in peak responses before sensor exhaustion (e.g., when measuring IL-1b-08, IL-1b-09, IL-1b-12, and IL-1b-13), which rules out the first hypothesis. The general decline in $R_{(300\ s,\ 50\ nM)}$ observed for both mAbs over the 15 ligands likely results from analyte consumption over repeated measurements rather than the binding properties of the cytokines.

The second hypothesis (conformational disruptions at GKB's binding site) would only be plausible if conformational changes were detected and restricted to GKB's binding site, since otherwise, canakinumab's responses to the misfolded proteins would also be affected. As confirmed by the NMR results, however, no major disruption occurred in the overall structure of the four tested muteins (see in section 3.3.4), including IL-

1b-09, which, as mentioned above, exhibited aberrant kinetics for GKB but not for CKB. Therefore, the higher variability observed in GKB's maximum apparent responses is most likely due to its dissociation rates (as mentioned above, higher and more disperse than canakinumab's), which in turn, are associated to the nature of the residues involved in the respective interactions (supporting the third scenario).

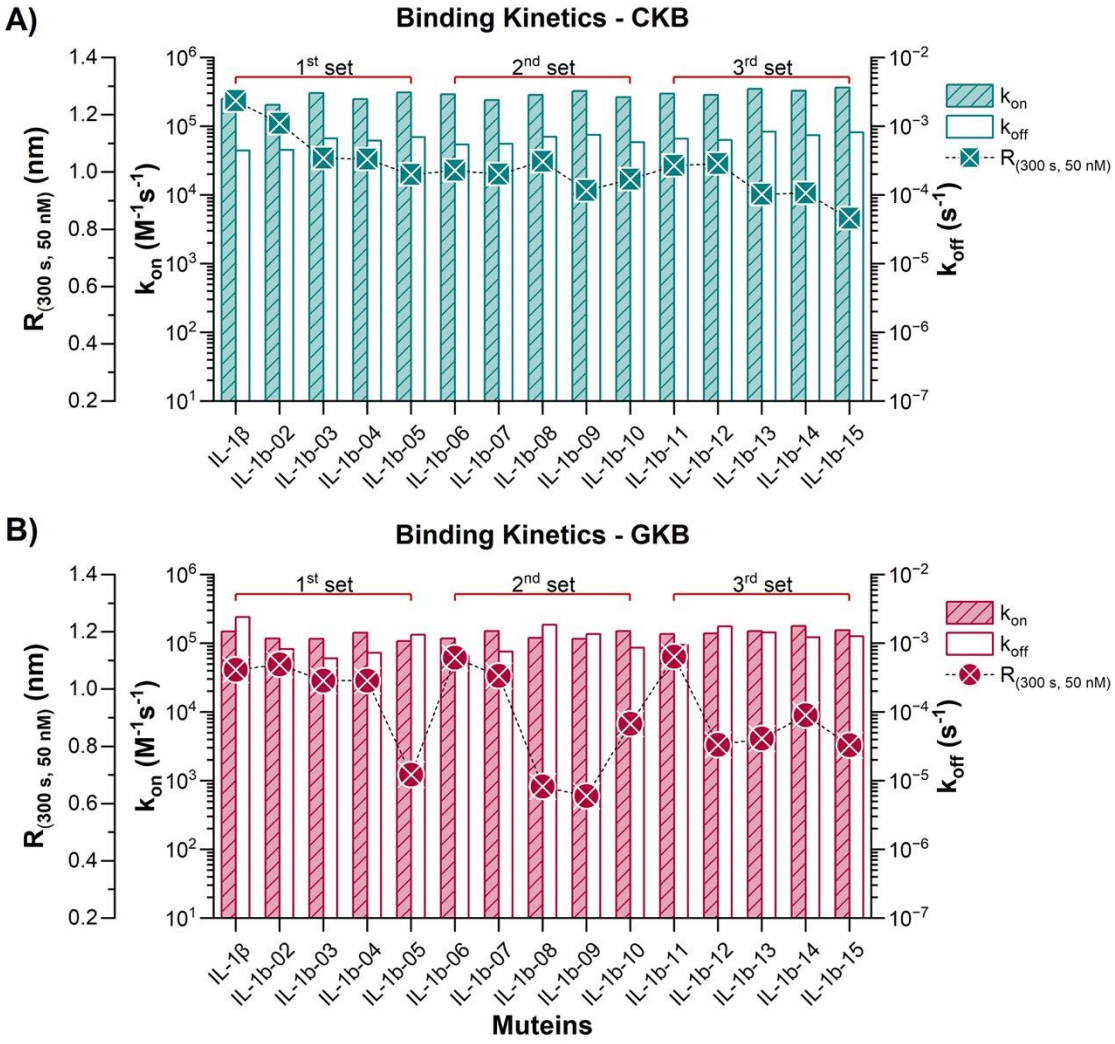

Figure 3.5 – Summary of kinetic parameters. k_{on}, k_{off}, and $R_{(300\ s,\ 50\ nM)}$ for the interactions between IL-1β and the 14 expressed muteins with **A)** canakinumab (CKB) or **B)** gevokizumab (GKB). Dashed lines do not indicate any relationship among the samples.

This effect is also observed in the dissociation constants (K_D, symbols and lines in Figure 3.8) calculated for each ligand and both Fabs, which average higher and vary more for GKB then for CKB (8.12 ± 3.85 and 2.22 ± 0.19 nM, respectively). The reason for these wider variations in gevokizumab's kinetic parameters across the tested ligands is likely the close proximity between this mAb's epitope and I222 and N223, mutation

points located far from canakinumab's binding site (see section 2.1.2, chapter II). As discussed in the next chapter (see section 4.3.3), these mutations may also have had an impact on the capacity of the polyclonal antibodies raised against IL-1b-09, IL-1b-13, and IL-1b-15 to neutralise IL-1β *in vitro*.

Finally, the third BLI assay described in section 3.2.2.1 compared the interaction between sIL-1R2 (soluble receptor) and IL-1β with those between the receptor and the expressed muteins. As shown in Figure 3.6 and Figure 3.7, whilst the designed antigens bound sIL-1R2 at association rates (k_{on}, filled bars in Figure 3.7) similar to that of the wildtype cytokine ($4.95 \cdot 10^{4} \pm 4.78 \cdot 10^{1}$ $M^{-1}s^{-1}$), they differ more significantly in the speed with which the muteins detach from the receptor, all but three (IL-1b-02, IL-1b-06, and IL-1b-07, red arrows) exhibiting dissociation rates (k_{off}, empty bars) at least two orders of magnitude higher than that measured for IL-1β ($1.00 \cdot 10^{7}$ s^{-1}, the lower limit of the instrument's detection range). Interestingly, these discrepancies in k_{off} are not reflected in the maximum apparent responses ($R_{(600\ s,\ 100\ nM)}$, symbols and lines) obtained throughout the 15 measurements, which deviated little from their average value (0.50 ± 0.06 nm).

More interestingly, the results from this assay also show that with the exception of three of the designed muteins (IL-1b-02, IL-1b-06, and IL-1b-07), all bind sIL-1R2 with appreciably lower affinity than the native cytokine. Three muteins (IL-1b-09, IL-1b-13, and IL-1b-15) exhibiting dissociation constants ≈ 4 orders of magnitude lower than IL-1β's (symbols and lines in Figure 3.8). These results indicate that the strategy of concentrating the mutations around the interface with domain D3 and far from domains D1/D2 may have succeeded in abrogating the second step of the ligand-receptor interaction model, i.e., the stabilisation of the heterodimeric complex IL-1β-IL-1R1/2 via association with the affinity-enhancing domains of the receptors (see section 2.1.1, chapter 2).

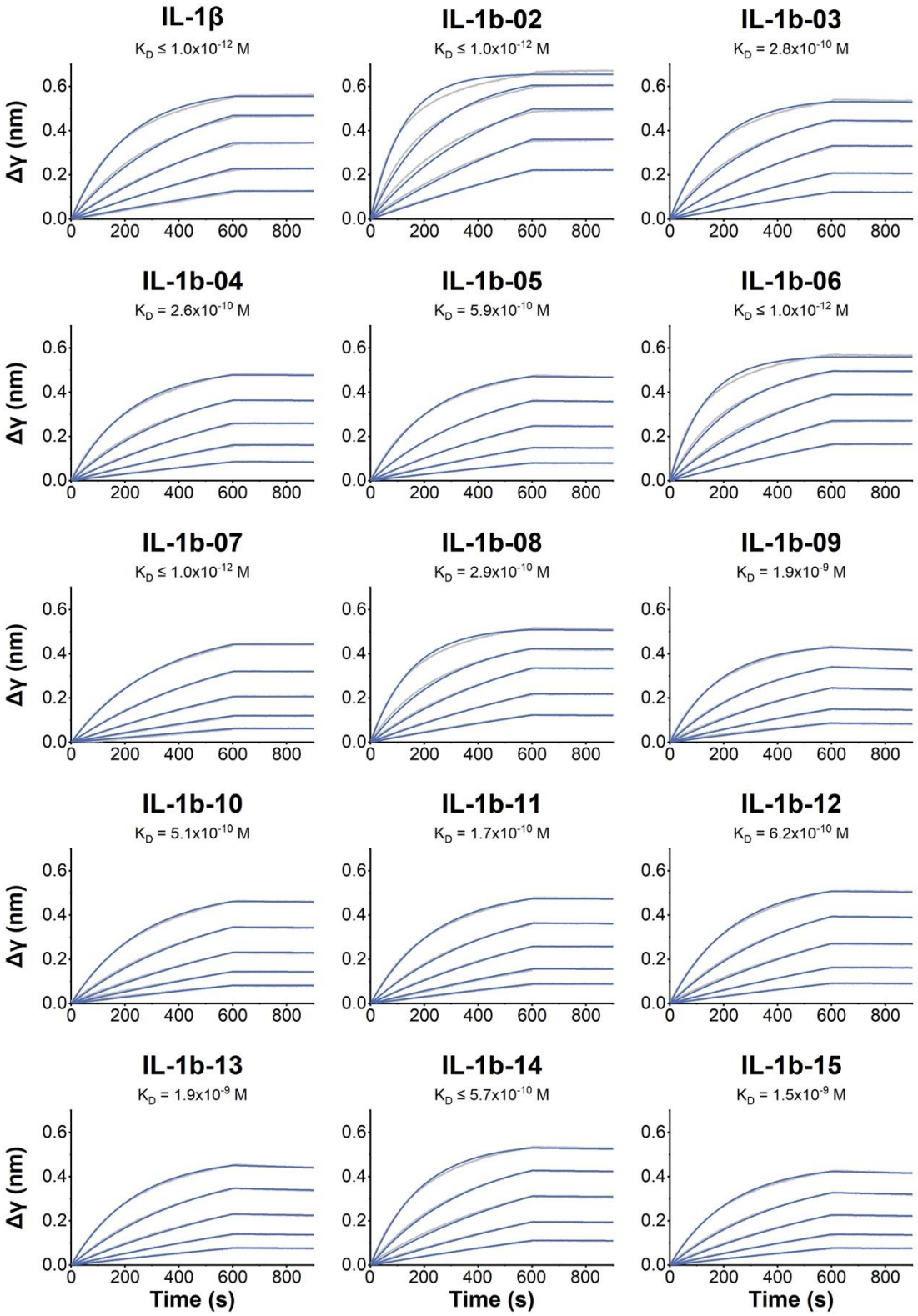

Figure 3.6 – Binding to sIL-1R2 (immobilised soluble receptor). Sensograms from BLI assays performed with sIL-1R2 as ligand and IL-1β or the selected muteins as analytes. From the highest to the lowest response: 100, 50, 25, 12.5, and 6.3 nM of analyte.

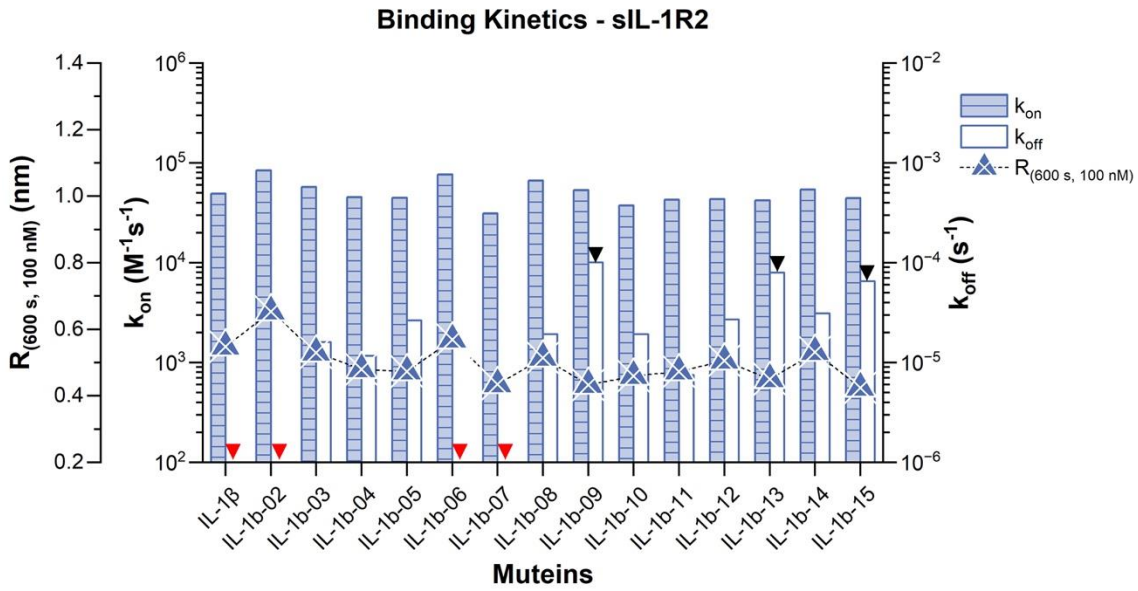

Figure 3.7 – Summary of kinetic parameters. k_{on}, k_{off}, and $R_{(600\ s,\ 100\ nM)}$ for the interactions between sIL-1R2 and IL-1β or the 14 expressed muteins. Dashed lines do not indicate any relationship among the samples.

To confirm that the mutein's binding properties were the result of the nature of the substitutions and not of major disruptions in the structure of the native cytokine, CSP analyses were performed for five selected muteins (highlighted in Figure 3.8): two with the highest affinity for sIL-1R2 (IL-1b-02 and IL-1b-07); and three with the lowest (IL-1b-09, IL-1b-13, and IL-1b-15).

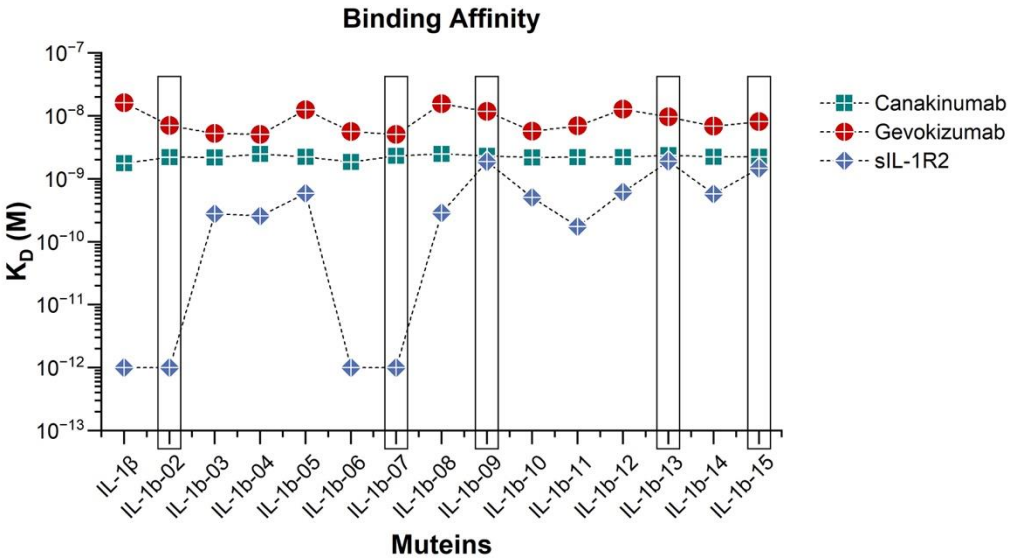

Figure 3.8 – Summary of BLI results. A) K_D measured for interaction between the cytokines and F_{ab} fragments of canakinumab (green circles) and gevokizumab (purple squares), as well as the ectodomain of sIL-1R2 (blue triangles). **B)** k_{on} and k_{off} of selected interactions. Dashed lines do not indicate any relationship among the samples.

IL-1b-09, IL-1b-13, and IL-1b-15 were also evaluated for their thermostability by means of CD-DSC. As previously mentioned, the aims of these assays were *1)* to ensure that potential differences observed in the immunogenicity of the three selected antigens were not the result of disturbances in conformational stability caused by the designed mutations; and *2)* to assess the adequacy of the design strategy in containing these structural disturbances to the mutated areas only. The results from these analyses are discussed in the following section.

3.3.3. Thermal stability

To rule out the possibility that the decrease in binding affinity between the selected muteins and sIL-1R2 occurred due a loss in conformational stability, the melting temperatures (T_m, an indirect reading of thermal stability)[72] of IL-1b-09, IL-1b-13, and IL-1b-15 (see previous section) were determined by CD-DSC and compared, as described in section 3.2.2.2, to that of IL-1β. For all proteins, the spectra collected at low-to-mild temperatures (i.e., $T < \approx 40$ °C, blue curves in the left panels of Figure 3.9) exhibited similar CD signatures as one reported by Hailey *et al* at comparable conditions.[73] Interestingly, up to the temperature of ≈ 70 °C, measured ellipticity behaves as what is typically observed for globular proteins, i.e., $\theta_{(\gamma)}$ steadily decreases as T is raised. At higher temperatures, however, the signal seems to recover its intensity (dark red curves in the left panels of Figure 3.9), an effect more pronounced at wavelengths lower than ≈ 230 nm.

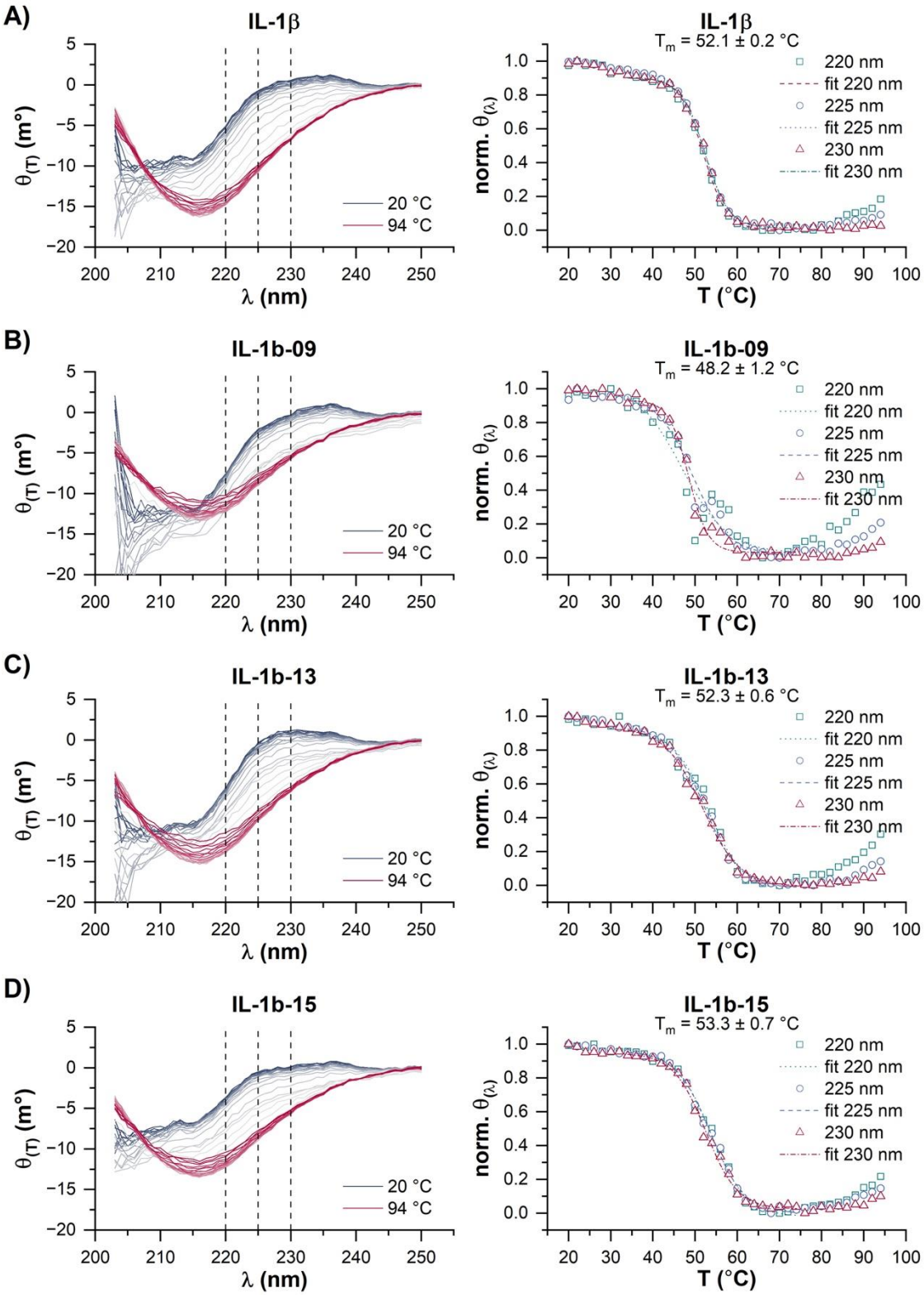

Figure 3.9 – Melting temperatures (T_m) of (A) IL-1β and (B-D) selected muteins. ($\theta_{(T)}$) Circular dichroism ellipticity measured at temperatures ranging from 20 to 94 ° C in 2 ° C-step (blue-to-purple gradient). Vertical dashed lines mark specific wavelengths from which θ values were extracted, normalised (norm. $\theta_{(\gamma)}$ or $\tilde{\theta}_{(\gamma)}$) and plotted against temperature (right panels).

To bypass this effect and capture most of the protein's conformational movements, three wavelengths (220, 225, and 230 nm, indicated by vertical dashed lines in the left panels of Figure 3.9) were selected in the range where ellipticity varies most widely, and, for each of these λ values, the $\theta_{(\gamma)}$ curves were normalised and plotted against the entire temperature range (right panels of Figure 3.9). Superimposition of the resulting curves showed no significant variability between the 3 selected wavelengths, with the exception of IL-1b-09, which $\tilde{\theta}_{(\gamma, T)}$ exhibited higher dispersion at temperatures above ≈ 45 °C. The T_m of each protein was calculated as the average of the inflexion points of a Boltzmann function fitted between 34 and 74 °C (range with the lowest dispersion) of the three plotted $\tilde{\theta}_{(\gamma, T)}$ curves. The results reveal a slight reduction in thermal stability for IL-1b-09; no effect on IL-1b-13's T_m; and a slight increase in temperature resistance for IL-1b-15, therefore demonstrating that the design strategy was generally successful in preserving IL-1β's conformational stability across the selected muteins.

With a ΔT_m of ≈ 4 °C, one could expect IL-1b-09 would exhibit the lowest level of cross-reactivity with IL-1β antibody, since it was the least stable of the three selected muteins. It happened, however, that this mutein produced, as discussed in section 4.3.3, the highest *in-vitro* neutralisation titres against the wildtype cytokine (IL-1b-15 yielded the lowest). Therefore, it is reasonable to assume that the mild changes in thermostability produced by the designed mutations had minimum effect on the cross-reactivity between the muteins and IL-1β.

3.3.4. Conformational accuracy

The SEC and BLI screenings described in sections 3.2.1.1 and 3.2.2.1 indirectly served as an HTP method for efficiently screening grossly misfolded muteins. In a more detailed structural analysis, however, backbone movements were measured, by means of ^{1}H-^{15}N nuclear magnetic resonance spectroscopy (2D-NMR, described in section 3.2.2.3), for five selected muteins with reference to an assigned spectrum obtained for native IL-1β (Figure 3.10). Measured under the same conditions as those employed on

the BLI assays (i.e., pH 7.3, 298 K), this reference spectrum had its assignments transferred from a publicly available ^{1}H-^{15}N HSQC dataset collected at higher temperature and more acidic conditions (i.e., pH 5.4, 309 K, see BMRB entry 435). In total, 129 out of 144 assignments (≈ 90 %) were transferred via a pH/T titration that also took into consideration spectral changes observed in the muteins' NMR frequencies. Nine of these (connected by red lines in Figure 3.10) correspond to the residues chosen to be substituted by the design protocol (F162, Q164, S168, I172, K209, K210, E221, I222, N223), while the assignments for the three remaining mutation points (E167, N169, and K219, see section 2.2.1) were lost during the titration process.

Figure 3.11 to Figure 3.15 below illustrate the spectra collected for IL-1b-02, IL-1b-07, IL-1b-09, IL-1b-13, and IL-1b-15, respectively, all superimposed on IL-1β's. They show the mutein's resonance frequencies to peak in the same range as those measured for the wildtype cytokine (i.e., 6-11 ppm ^{1}H and 107-135 ppm ^{15}N), with no large movements observed in the original traces. As expected, the peaks corresponding to the mutated residues were not mapped in the mutein's spectra (indicated by the red lines in in Figure 3.11).

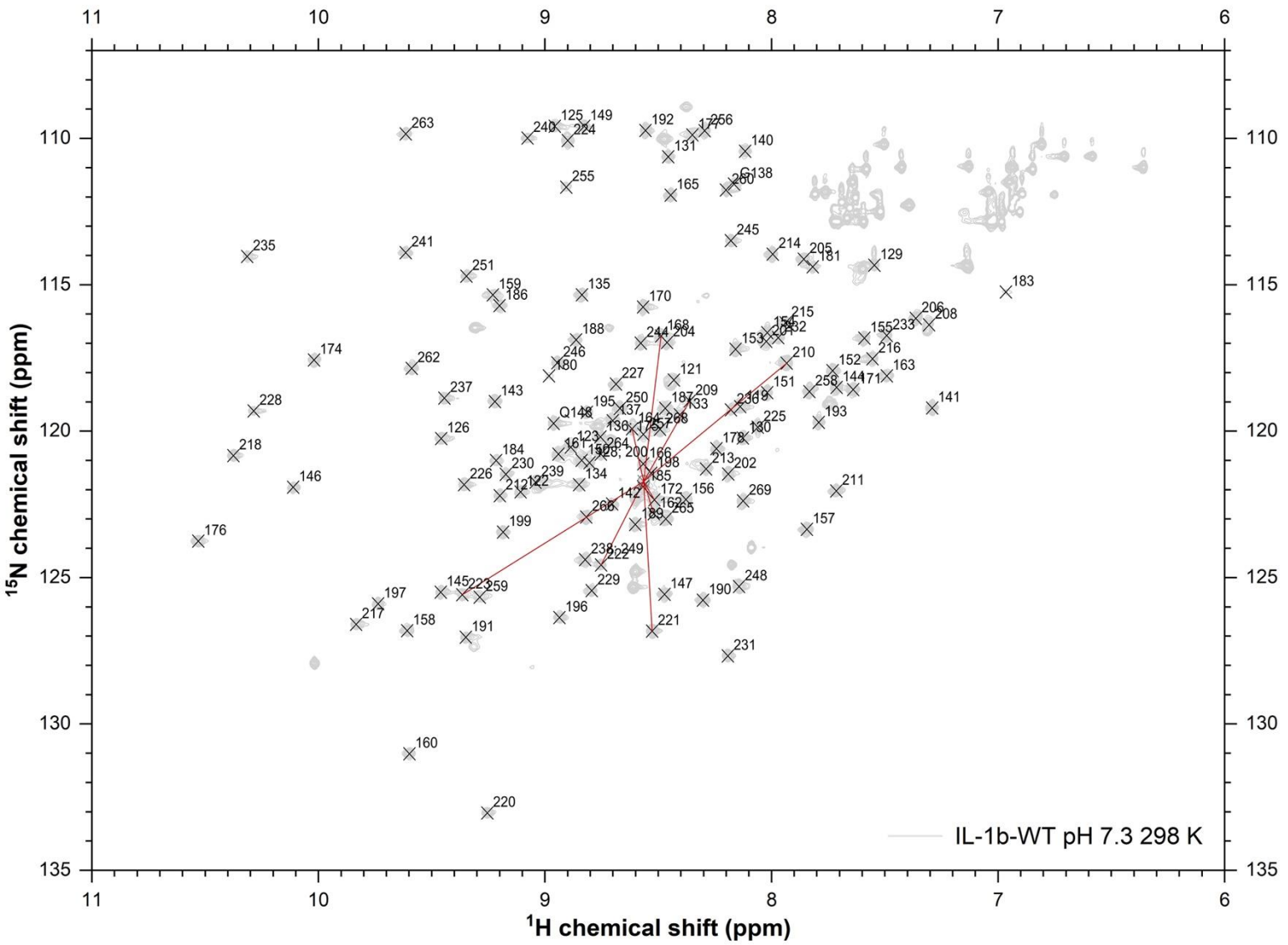

Figure 3.10 – ^{1}H-^{15}N HSQC spectrum collected for IL-1β at pH 7.3 and temperature of 298 K. Assignments transferred from BMRB entry 435.

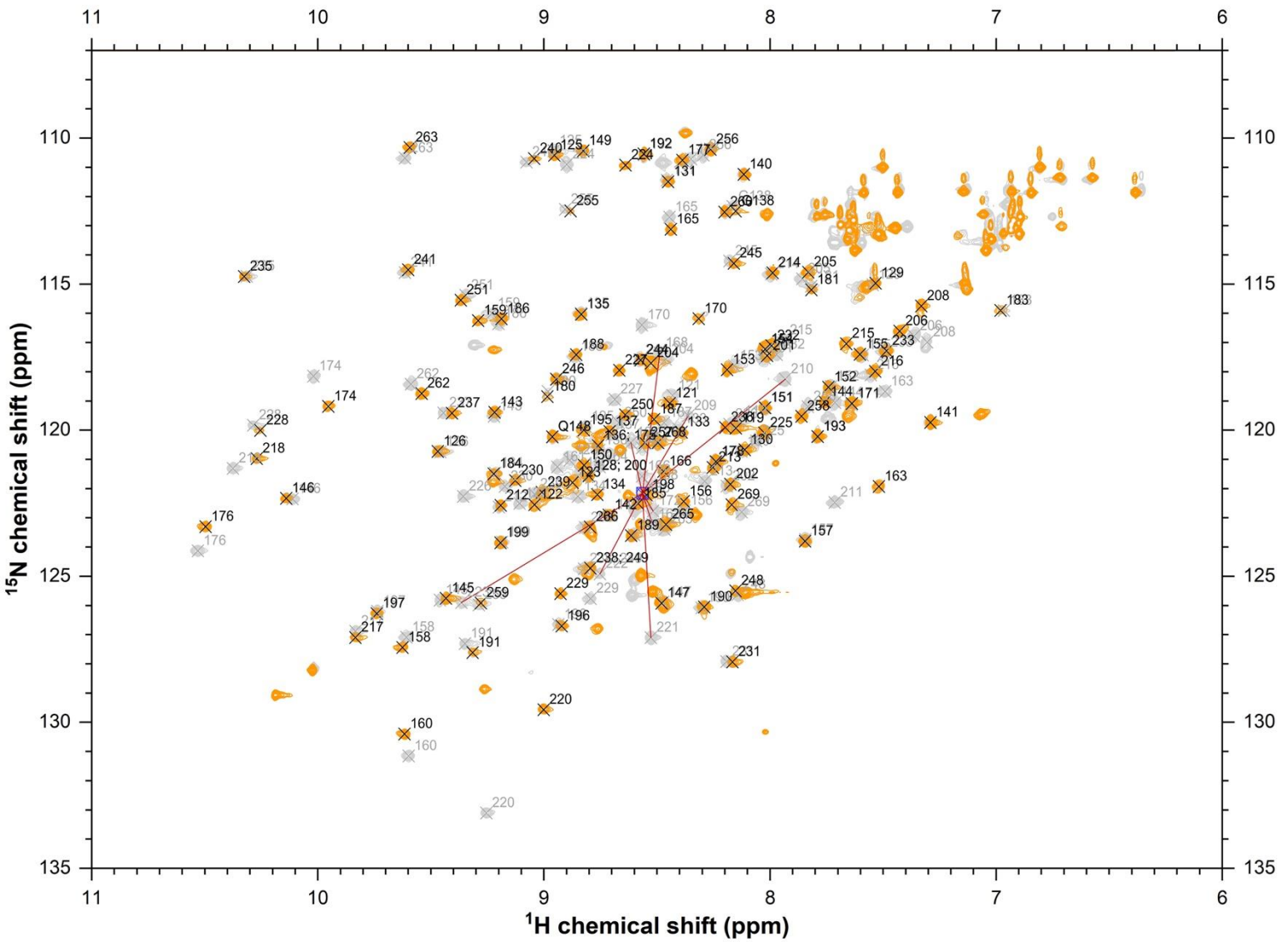

Figure 3.11 – ^{1}H-^{15}N HSQC spectrum collected for IL-1b-02 at pH 7.3 and temperature of 298 K. Assignments transferred from wildtype IL-1β.

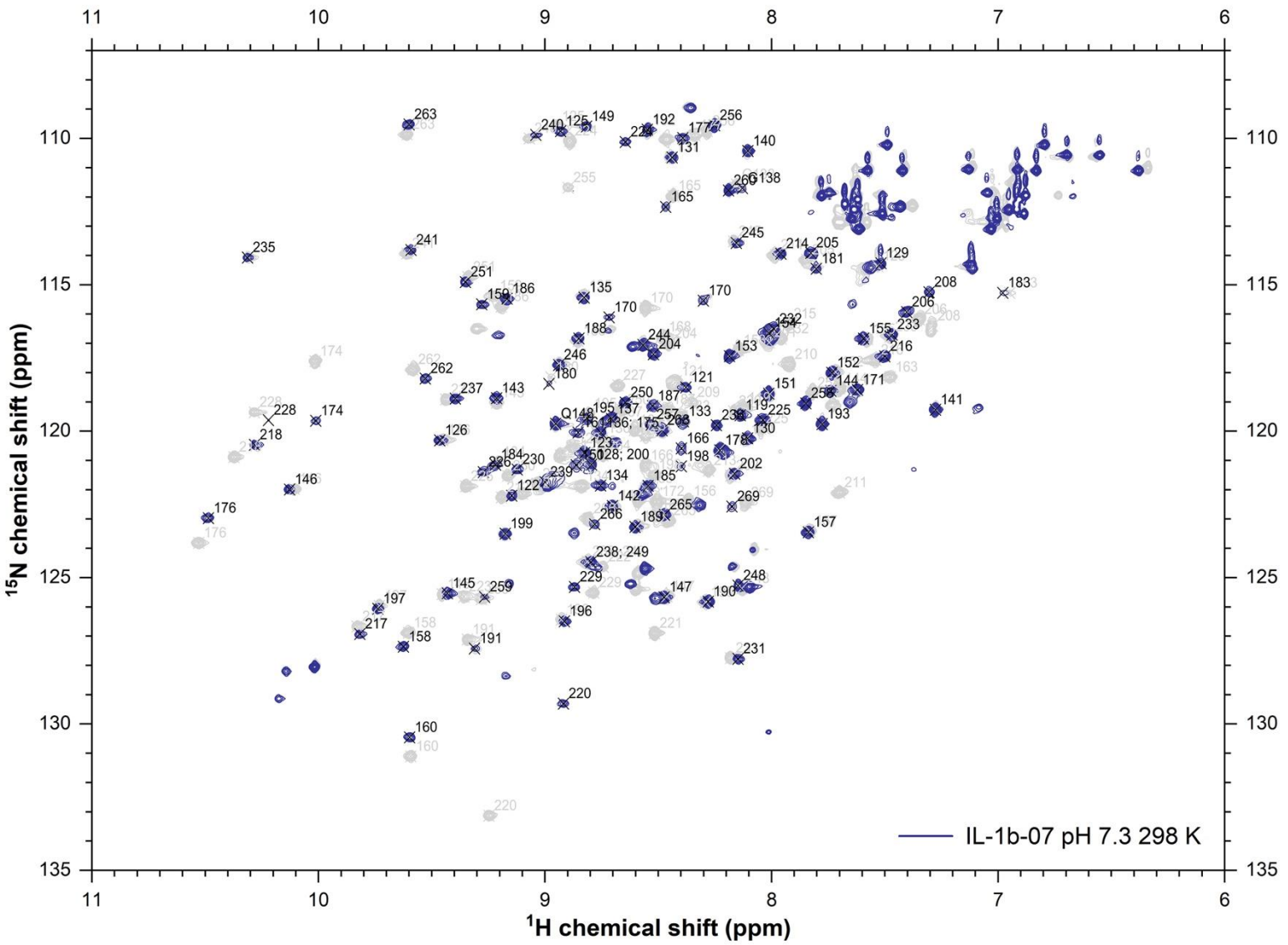

Figure 3.12 – ^{1}H-^{15}N HSQC spectra collected for IL-1b-07 at pH 7.3 and temperature of 298 K. Assignments transferred from wildtype IL-1β.

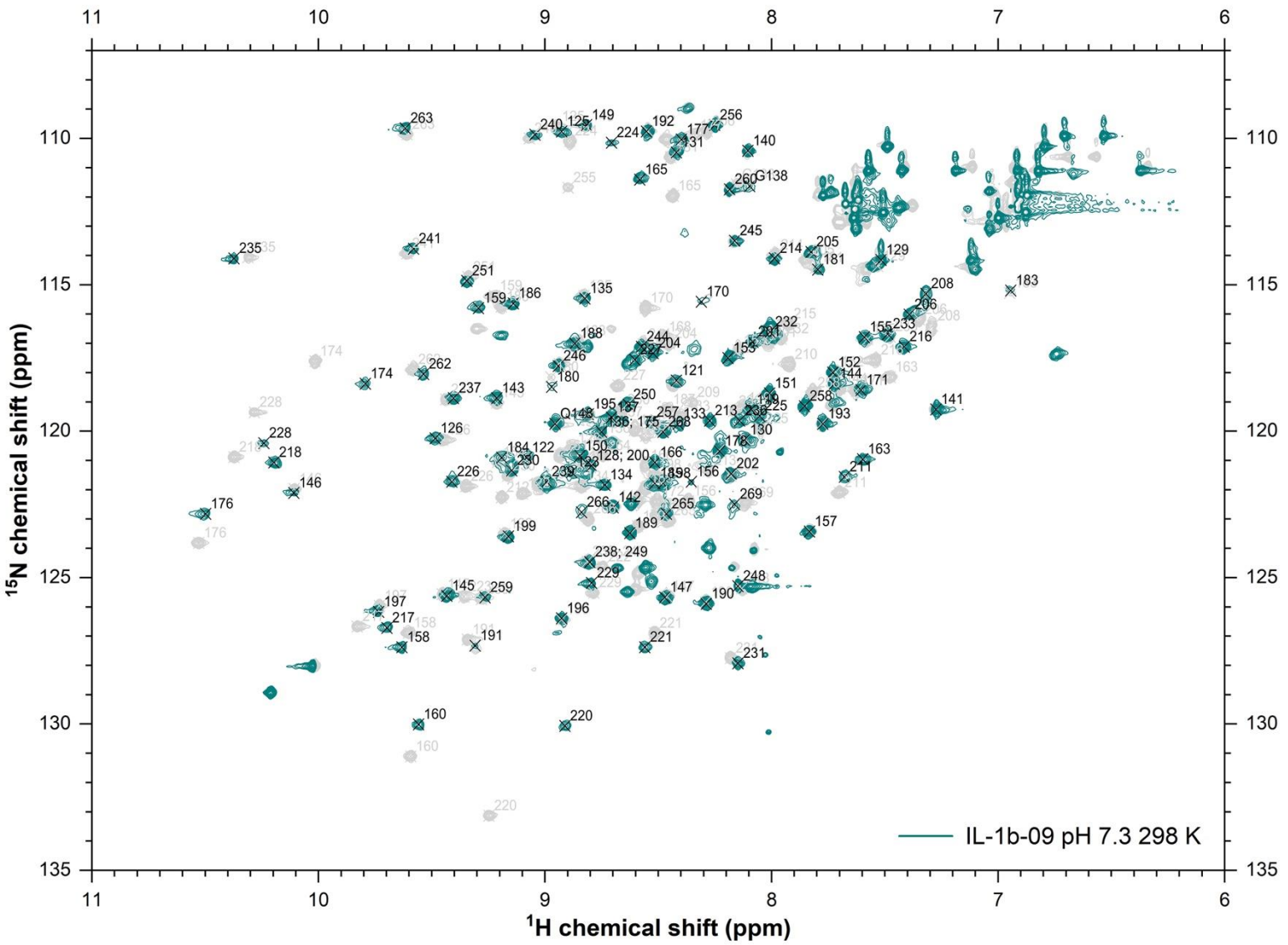

Figure 3.13 – ^{1}H-^{15}N HSQC spectrum collected for IL-1b-09 at pH 7.3 and temperature of 298 K. Assignments transferred from wildtype IL-1β.

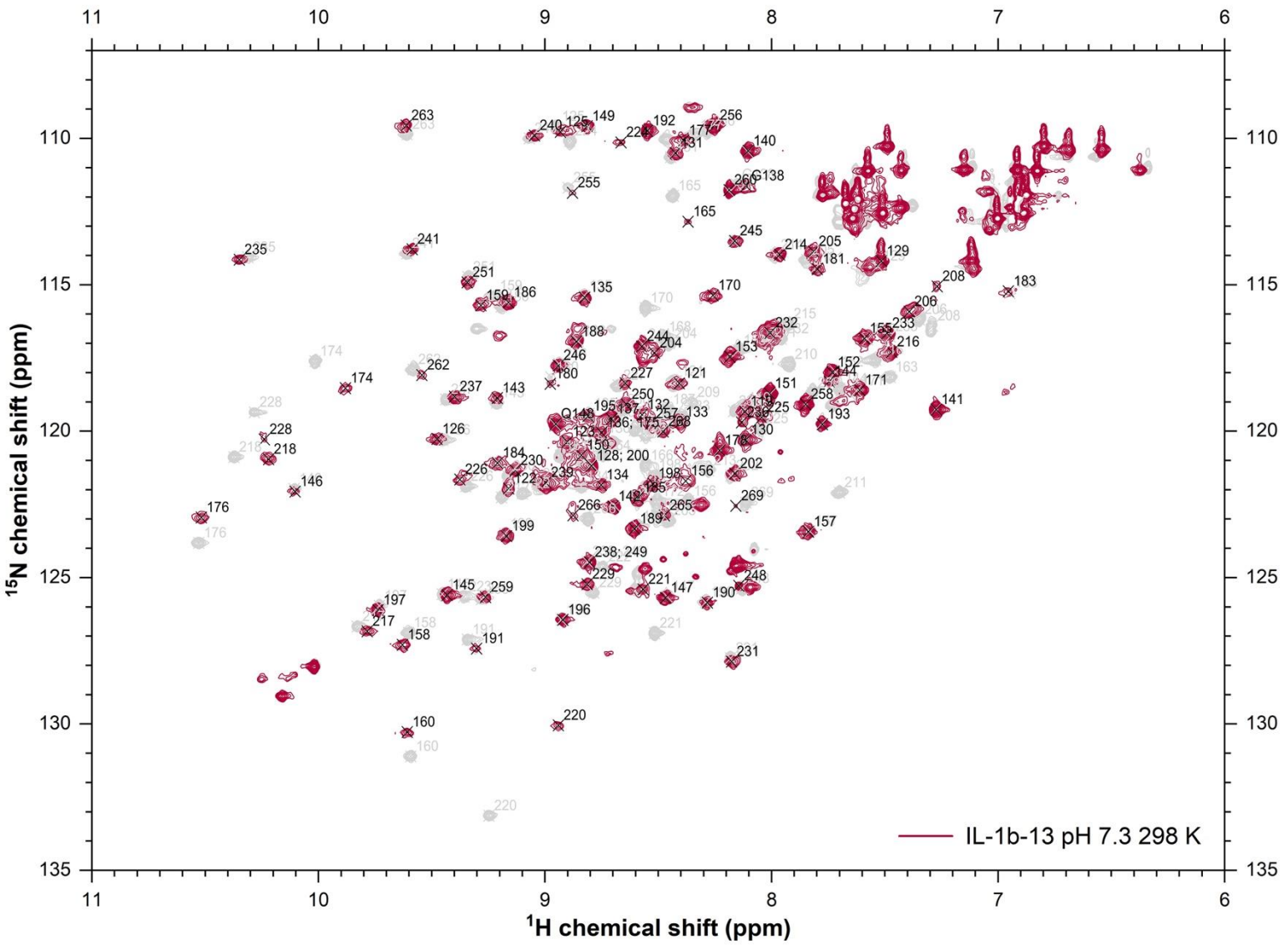

Figure 3.14 – ^{1}H-^{15}N HSQC spectrum collected for IL-1b-13 at pH 7.3 and temperature of 298 K. Assignments transferred from wildtype IL-1β.

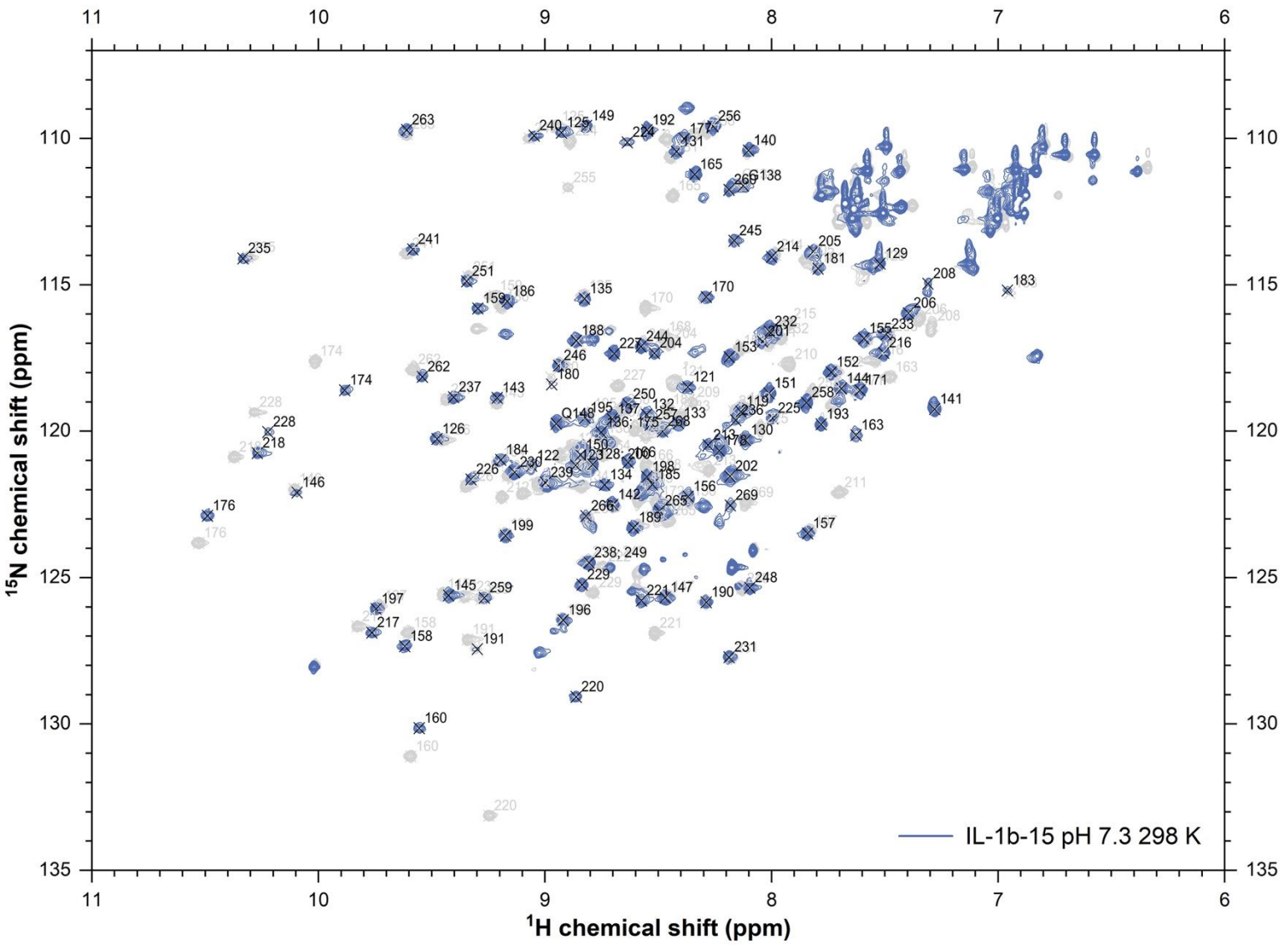

Figure 3.15 – ^{1}H-^{15}N HSQC spectrum collected for IL-1b-15 at pH 7.3 and temperature of 298 K. Assignments transferred from wildtype IL-1β.

In addition to those attributed to the mutation points, a few other assignments were not transferred to the muteins, mainly because their movements in the HSQC plane exceeded the pre-established cut-off (≤ 5.0 ppm straight line, see section 3.2.2.3). All these assignments missing from IL-1β's spectrum are indicated by grey vertical bars in Figure 3.16, which, together with the largest CSPs are concentrated on, or in the vicinity of the mutated loops (black rectangles, see section 2.2.1). This result demonstrates the efficacy of the *in-silico* design strategy in restraining potential conformational disturbances to the modified sites only.

More interestingly, the results obtained for IL-1b-02 and IL-1b-07 are nearly identical to those produced by the other tested muteins, which further supports the conclusion that the differences observed in binding kinetics of IL-1b-09, IL-1b-13, and IL-1b-15 for sIL-1R2 (see section 3.3.2) were a product of the intrinsic properties of the replaced residues rather than an effect of structural disruptions caused by particular surface substitutions.

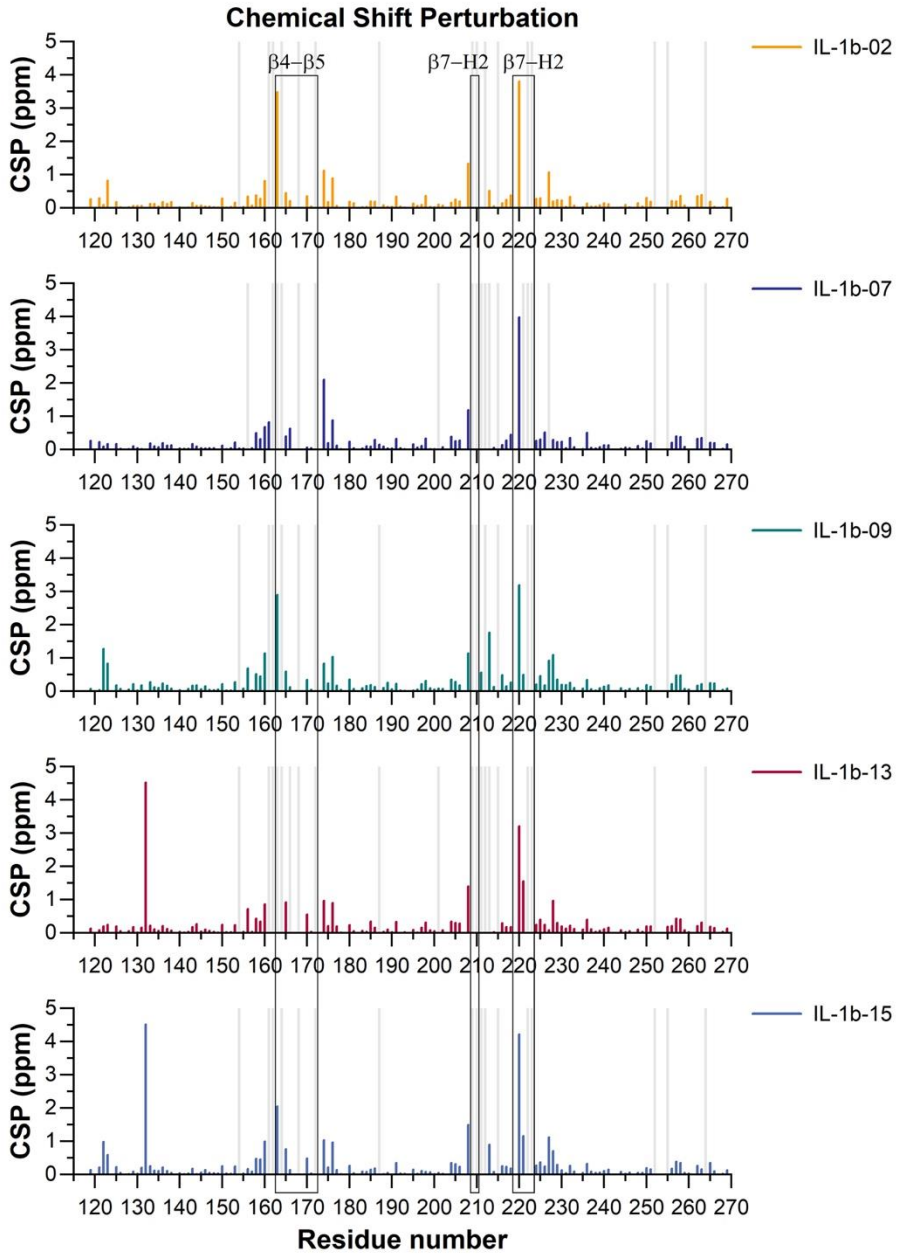

Figure 3.16 – CSPs. Chemical shift perturbations (coloured bars) measured for IL-1b-02, IL-1b-07, IL-1b-09, IL-1b-13, and IL-1b-15 in reference to IL-1β's spectrum (Figure 3.10). Assignments not transferred are indicated by grey bars.

3.4. Conclusions

The experiments described in this chapter aimed at assessing, via several biophysical methods, the accuracy of the predicted models of 14 designed sequences selected according to methods described in the previous chapter (see section 2.2.2 and 2.3.1). Expression of these mutant sequences in conditions identical to the template protein resulted, as predicted by the MD simulations described in section 2.2.3 and discussed

in section 2.3.2, in yields and hydrodynamic profiles nearly identical to IL-1β's (see section 3.3.1). Furthermore, similarity in the affinities with which these muteins bound to canakinumab and gevokizumab corroborated to the conclusion that the designed mutations produced minimal effects on the overall structure of the cytokine (see section 3.3.2).

More importantly, a subsequent binding assay showed that three of the expressed muteins possess binding affinities for sIL-1R2 at least 50,000 times lower than that of IL-1β (see also section 3.3.2), confirming that the proposed property-based design approach succeeded in disrupting the interaction between the cytokine and its decoy receptor. Due this characteristic, IL-1b-09, IL-1b-13, and IL-1b-15 were selected for further biophysical and immunological analyses.

This chapter also investigated a question not addressed by the abovementioned MD simulations, namely whether the designed mutations had an impact on the thermostability of the modified antigen, a surrogate measurement of conformational stability. For this purpose, the melting temperature of the three selected muteins were determined and compared with IL-1β's, resulting in an absolute difference of ≤ 4 °C/52 °C (see section 3.3.3), later shown to be insufficient to alter the immunogenicity of the cytokine, as demonstrated by the experiments discussed in the next chapter. The fact that IL-1β's T_m was conserved among the selected muteins also attest to the adequacy of the design strategy in maintaining the stability of the antigen despite the large number of residues replaced.

Finally, a detailed structural analysis of the selected muteins (discussed in section 3.3.4) showed no significant changes in the cytokine's core, a possibility considering the extensiveness of the performed surface modifications. As it is also discussed in the next chapter, this conformational resemblance may had been key for the high level of cross-reactivity observed among the total anti-IL-1β antibody responses elicited by the three most promising muteins in mice, which was also the aim of the proposed design strategy.

Chapter IV. Immunological characterisation of selected muteins

4.1. Introduction

The binding assays discussed in section 3.3.2 showed IL-1β's ability to form a ternary complex with IL-1R1 and IL-1R3 to have been abolished by the substitutions borne by IL-1b-09, IL-1b-13, and IL-1b-15. To confirm that this result indeed translates into less toxic antigens, as intended (see section 1.4.2.1), the IL-1 activity of the three selected muteins were measured by cell activation assay and compared with that of the wildtype cytokine (as described in section 4.2.1). As expected, the results (discussed in section 4.3.1) showed an almost complete abrogation of cytokine activity in two muteins, while the third exhibited several orders of magnitude lower activity than that measured for IL-1β.

The most important properties of the designed antigens, however, were assessed from a simple immunisation assay performed on wildtype C57 BL/6 mice (described in section 4.2.2). Quantitation of total and neutralising antibody titres (described in section 4.2.2.4) raised by IL-1β or the selected muteins conjugated to $CuMV_{tt}$ virus-like particle (as described in 4.2.2.2) showed the muteins to elicit levels of total anti-IL-1β muIgG responses equivalent to that obtained from immunisation against the WT cytokine (see section 4.3.2), although with significantly neutralising capacity (see section 4.3.3).

To better understand how the antibodies raised against the four antigens block IL-1β from interacting with IL-1R1 and IL-1R3, biolayer-interferometry (BLI) competition assays were performed with sera collected from fully immunised mice (see section 4.2.2.5). Discussed in section 4.3.4, the results show that the reduction in neutralisation titres caused by the extensive modifications performed on IL-1β's surface may be a consequence of a lower number of high-affinity antibodies cross-reacting with neutralising sites of the wildtype cytokine.

As discussed in section 4.3.5, however, this reduction in neutralising cross-reactivity between the muteins and the wildtype cytokine did not translate into lower

protection against the systemic effects of IL-1β. In fact, the animals immunised with IL-1b-09, IL-1b-13, and IL-1b-15 coupled to $CuMV_{tt}$ resisted to cytokine challenge (also described in section 4.2.2.3) in the same way as those vaccinated against IL-1β (see section 4.3.5). More importantly, none of the muteins seemed to have induced disease-enhancing antibodies, a safety issue encountered in a previous attempt.[58]

4.2. Materials & methods

4.2.1. Bioactivity assays

IL-1β, IL-1b-09, IL-1b-13, and IL-1b-15 were produced as described in section 3.2.1.1 with the addition of a further anion-exchange chromatography step for endotoxin removal using a Proteus midi kit according to the manufacturer's instructions (Bio-Rad, Hercules, CA – USA). Cytokine activity was measured using the HEK-blue IL-1 system (Invivogen, San Diego, CA – USA). Briefly, adherent HEK293 cells modified to express AP-1-inducible secreted embryonic phosphatase (SEAP) were cultured at 37 °C, 5 % CO_2, and 90 % humidity in DMEM-GlutaMAX (ThermoFisher, Waltham, MA – USA) supplemented with 10 % v/v heat-inactivated FBS, 100 $U \cdot mL^{-1}$ penicillin-streptomycin, and 100 $\mu g \cdot mL^{-1}$zeocin. At ≈ 80-90 % confluence, the cells were detached with 5 mM EDTA in PBS, pelleted by centrifugation at 300 g for 5 min, resuspended in growth medium without zeocin, and filtered with 70-µm cell strainers. With their concentration adjusted to $\approx 1.0 \cdot 10^6$ $cells \cdot mL^{-1}$, 50 µL per well of the reporter cells were transferred to a 98-well assay plate and incubated for 20 h at 37 °C and 5 % CO_2.

In a separate plate, 1:3 serial dilutions of wildtype cytokine and the selected muteins were performed in triplicate in growth medium, with IL-1β's initial concentration at 10.0 $ng \cdot mL^{-1}$ and IL-1b-09's, IL-1b-13's, and IL-1b-15's at 10.0 $\mu g \cdot mL^{-1}$. PBS was used as negative control. 50 µL per well of the dilutions were then transferred to the cell plate, which was returned to the incubator for additional 24 h. Finally, 20 µL of supernatant were collected and mixed with 180 µL of Quanti-blue developing reagent (Invivogen) and incubated for 3h at 37 °C, period after which absorbance of polarised

light at 620 nm was measured for each well. Measurements from the negative control were subtracted in a per-dilution factor basis from the absorbance values obtained from each protein serial dilution. The resulting $OD_{620(C)}$ curves for each cytokine were then globally (i.e., all replicates included) fitted via an asymptotic-symmetry-based method into a 4-variable polynomial dose-response model with χ^2 tolerance of $1.0 \cdot 10^{-9}$ and no weighting. The results are discussed in section 4.3.1.

4.2.2. Immunisation assays

4.2.2.1. Ethics statement

No human samples were used in the assays described in this chapter. Experiments performed on mice were conducted at the Experimental Animal Centre of the University of Bern according to the directives of the Swiss Animal Welfare Act of 16 December 2005 (version 1 January 2022) and under cantonal ethics approval BE81/2021, national number 34085.

4.2.2.2. Antigen-VLP conjugation

Recombinant IL-1β and selected muteins IL-1b-09, IL-1b-13, and IL-1b-15 were produced as described in section 4.2.1. Cucumber mosaic virus-derived VLP particles genetically fused to an immunodominant tetanus toxoid T-cell epitope ($CuMV_{tt}$) were produced as described by Zeltins and colleagues,[74] and conjugation between the antigens and VLP particles was performed via chemical cross-linking with SMPH (ThermoFisher). For that, 1.0 mL of $CuMV_{tt}$ at 1.0 $mg \cdot mL^{-1}$previously dialysed in coupling buffer (CB, 5 mM $NaPO_4$, 2 mM EDTA, pH 7.4) was mixed with 15.5 µL of SMPH at 10.0 $mg \cdot mL^{-1}$ in DMSO (10:1 SMPH to VLP subunit molar ratio) and incubated in a thermoblock at 25 °C, 400 rpm, for 30 min. Excess SMPH was then removed by size-exclusion chromatography (SEC) using 0.5 mL-, 40 kDa MWCO-spin desalting columns (ThermoFisher) pre-equilibrated with CB according to the manufacturer's instructions.

With the eluate split in equal fractions of 200 µL, the antigens were added at a 1:1 antigen to VLP subunit molar ratio (the fifth fraction served as negative control in the immunisation assays). To complete the mix, the reducing agent TCEP (ThermoFisher) was added to each sample at 10:1 TCEP to VLP subunit molar ratio. Finally, after 3 h of incubation in a thermoblock at 25 °C, 400 rpm, non-conjugated antigen molecules were removed by dialysis in PBS using a 100 kDa membrane. The conjugation process was assessed by SDS-PAGE, as described by Vogel and colleagues.[75]

4.2.2.3. Mice immunisation and cytokine challenge

For the immunisation assay, 5 groups of 5 female, 10-week old, C57 BL/6 mice were received 10 µg of either $CuMV_{tt}$ (negative control), $CuMV_{tt}$-IL-1β (positive control), $CuMV_{tt}$-IL-1b-09, $CuMV_{tt}$-IL-1b-13, or $CuMV_{tt}$-IL-1b-15 intraperitoneally at day 0, and a second IP injection with also 10 µg of the same immunogens at day 14. Blood samples were collected every 7 days. At days 35 or 42 (first and second immunisation attempts, respectively), the animals were IP injected with 1.0 µg of IL-1β in PBS, and blood samples were taken at every 3 hours (Figure 4.1). A second immunisation attempt was needed due a failure in the challenge step of the first one, which required the experiment to be repeated.

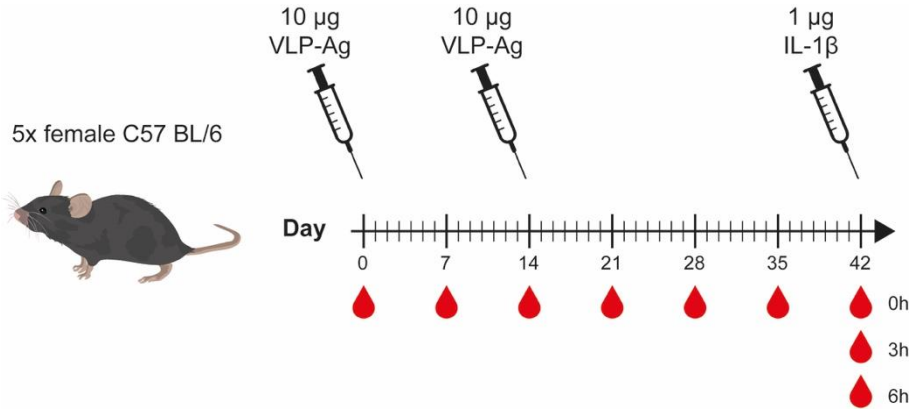

Figure 4.1 – **Immunisation assay.** Each group of 5 female C57 BL/6 mice was injected with 10 µg of IL-1β or each of the three selected muteins coupled to $CuMV_{tt}$ virus-like-particle at days 0 and 14 ($CuMV_{tt}$ alone was used as negative control). The animals were then challenged at day 42 (35 in the first attempt) with 1 µg of IL-1β. Blood samples were collected once a week during the immunisation period and at every 3 hours post-challenge.

The sera were immediately separated from the other components of the blood by centrifugation at 13,000 g for 10 minutes in Microtainer tubes (BD, Franklin Lakes, NJ – USA) and stored at -20 °C until further analysis. Samples collected during cytokine challenge, in particular, were submitted to muIL-6 and circulating IL-1β quantitation by qPCR using ProQuantum High-Sensitivity Immunoassays (ThermoFisher).

4.2.2.4. Total and neutralising antibody titres

Total muIgG antibody titres were determined by indirect ELISA from pooled sera, with the plates coated with 1.0 $\mu g \cdot mL^{-1}$ of IL-1β or each of the three selected muteins diluted in PBS, all blocked with 1 % of casein also in PBS. Goat anti-mouse IgG poly-clonal antibodies conjugated to horseradish peroxidase (HRP) were used for muIgG detection. Absorbance measurements as a function of dilution factor were fitted to the Boltzmann sigmoidal model through the Levenberg-Marquardt algorithm over 400 points and a maximum 500 iterations. Conversion tolerance was set to $1 \cdot 10^{-6}$. Titres were taken as the midrange points ("EC50") of the fitted curves. The measurements were obtained in triplicates, and the results are discussed in section 4.3.2.

For measurement of neutralising antibody titres, HEK-blue IL-1 cells (Invivogen) were cultured in 96-well plates as described in section 4.2.1. In separate plates, sera collected at day 42 before challenge (i.e., from second immunisation attempt only) were serially diluted at a 1:2.5 v/v in 1 $ng \cdot mL^{-1}$ of IL-1β in growth medium. After incubation at 1,000 rpm for 1 h, at RT, the dilutions were then added to the growing cells at 1:1 v/v, which were then returned to incubation at 37 °C, 5 % CO_2, and 90 % humidity for additional 24 h. SEAP activity was measured from the supernatants also as described in section 4.2.1. Analogously, neutralising antibody titres were then taken as the midrange point of the 4-variable polynomial dose-response function fitted to the resulting $OD_{620(\text{dil. fac.})}$ curves. The assay was performed in triplicate, and the results are discussed in section 4.3.3.

4.2.2.5. IL-1β binding inhibition

Inhibition of IL-1β binding to sIL-1R1 and recruitment of sIL-1R3 by high-affinity antibodies raised against the cytokine or each of the three selected muteins was measured by BLI using an Octet RED96e interferometer (Sartorius, Wokingham RG – UK). Anti-5xHis HIS1K sensors (Sartorius) were loaded with 25 $\mu g \cdot mL^{-1}$ IL-1β in kinetic buffer (KB, composed of 0.02 % Tween 20 and 0.1 % BSA in PBS) until saturation (150 s). After a 60 s-baseline with KB only, association with the antibodies elicited by each tested immunogen was carried out for 150 s with sera collected at day 42 of the second immunisation attempt diluted 1:20 in KB. A second baseline was established with the dissociation of the low-affinity pAbs in KB for 150 s. Finally, a second association step was performed with the receptors diluted at an equimolar total concentration of 1.0 $\mu g \cdot mL^{-1}$. Figure 4.2 below illustrates the assay's settings, as well as the typical Δγ curves obtained.

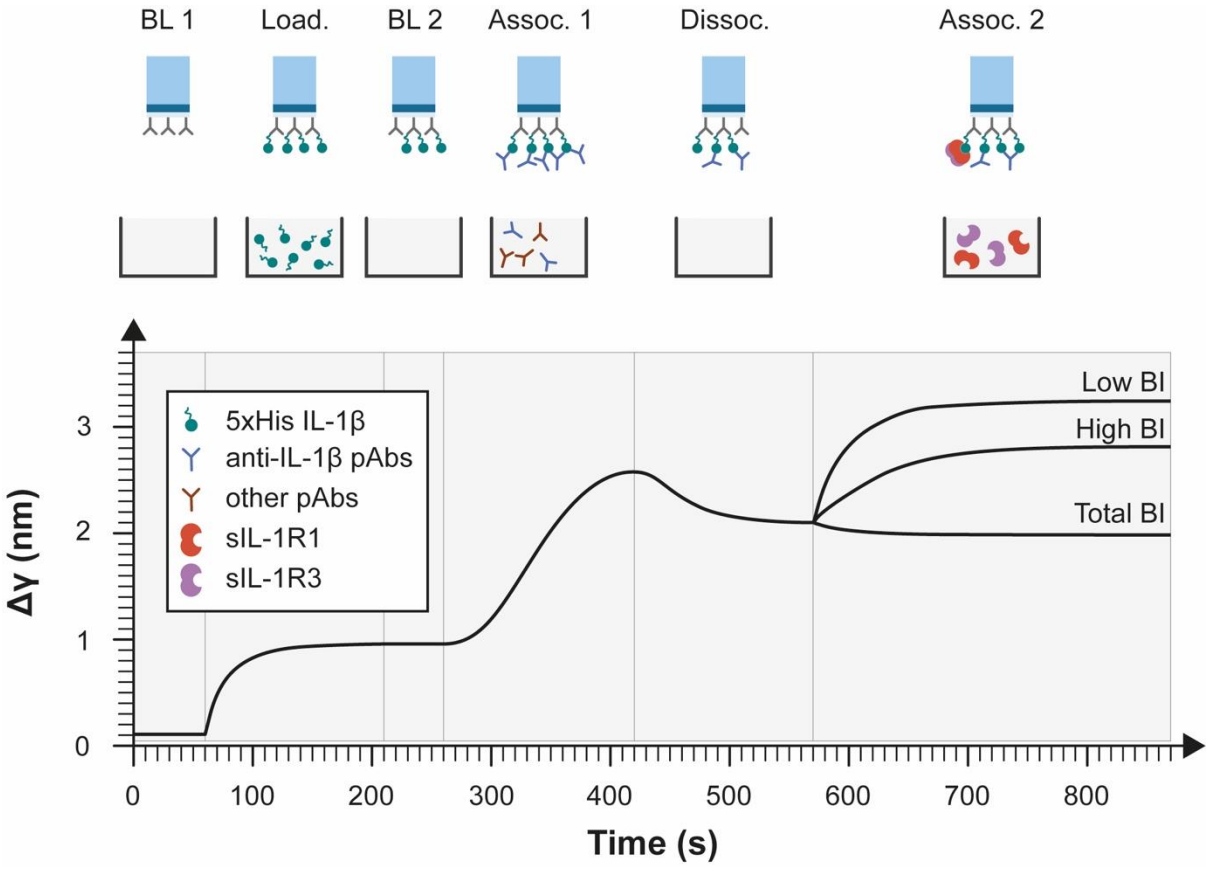

Figure 4.2 – IL-1β binding inhibition assay. (top) Schematical representation of the sensors' state at each step of the assay. (bottom) Typical interference pattern of three conditions: low, high, and total inhibition.

The binding inhibition (BI) indexes were calculated as the proportional reduction in AUC of the interference curves obtained at the receptor association step ("Assoc. 2" in Figure 4.2) between no inhibition (e.g., only KB in "Assoc. 1") and maximal cytokine blocking or no receptor binding (e.g., sera from $CuMV_{tt}$-IL-1β-immunised mice in "Assoc. 1" or no receptor in "Assoc. 2," respectively). The results are discussed in section 4.3.4.

4.3. Results & discussion

4.3.1. Cytokine bioactivity

As described in section 4.2.1, the capacity of the designed muteins to elicit a typical interleukin 1 response was indirectly measured through the alkaline phosphatase activity of AP-1-inducible SEAP reporter gene stably transfected into IL-1R2 knocked-out HEK293 cells. The results, illustrated in Figure 4.3, below, show IL-1β's activity to have been nearly abolished by the designed modifications, with the most reactive of the three selected muteins – IL-1b-13 – exhibiting an IL-1 activity level ≈ 50,000 times lower than that of the wildtype cytokine (midrange points of 1.35 $\mu g \cdot mL^{-1}$ and 27 $pg \cdot mL^{-1}$, respectively). No peak signal was achieved for IL-1b-09 and IL-1b-15 within the tested concentration range.

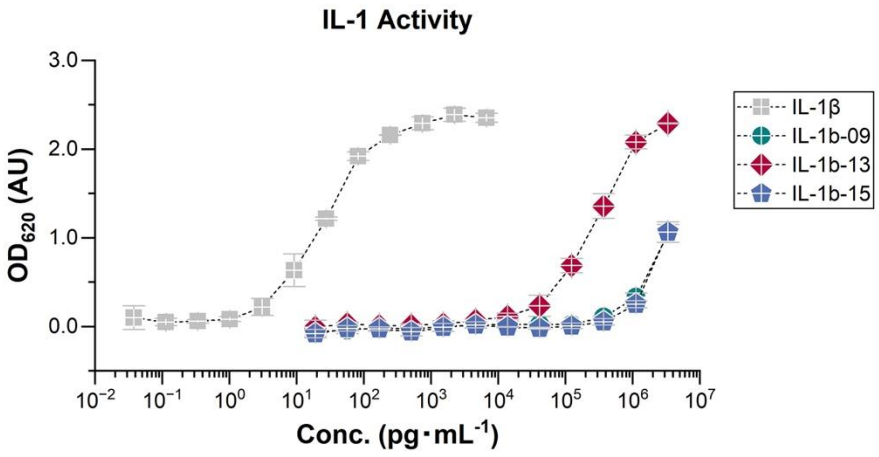

Figure 4.3 – IL-1 activity of recombinant IL-1β and designed muteins. 620-nm absorbance measurements of AP-1-inducible SEAP activity from HEK-blue IL-1 cells incubated in the presence of either recombinant IL-1β or each of the three selected muteins IL-1b-09, IL-1b-13, and IL-1b-15. Error bars representing the standard deviation of three technical replicates.

Interestingly, as discussed in section 4.3.4, no correlation was found between the bioactivity of the tested muteins and the capacity of the antibody responses raised against them to block the effects of IL-1β *in vitro*, with $CuMV_{tt}$-IL-1b-13 producing neutralising titres significantly lower than that of IL-1b-09 conjugated to the same VLP.

4.3.2. Antigen immunogenicity

As mentioned in section 4.2.2.3, two attempts of an immunisation assay conceived to assess the quality of the antibody responses against the selected muteins in comparison with IL-1β were performed in wildtype C57 BL/6 mice. Figure 4.4 to Figure 4.7 illustrate the absorbance measurements from ELISA assays performed with plates coated with each of the four antigens, and the primary antibodies specific to all subclasses of muIgG (see section 4.2.2.4). Total muIgG titres calculated from these curves are plotted against time of first injection in Figure 4.8. These results show all tested immunogens to have raised strong antibody responses with no detectable cross-reactivity between the carrier ($CuMV_{tt}$ VLP) and the antigens (IL-1β and the muteins IL-1b-09, IL-1b-13, and IL-1b-15), confirming what has been observed for similar constructs.[53,54] They also confirmed the adequacy of the chosen prime-and-boost regimen, given that maximum muIgG titres were reached in ≤ 7 days after the second injection and remained at the same level for the duration of the experiment.

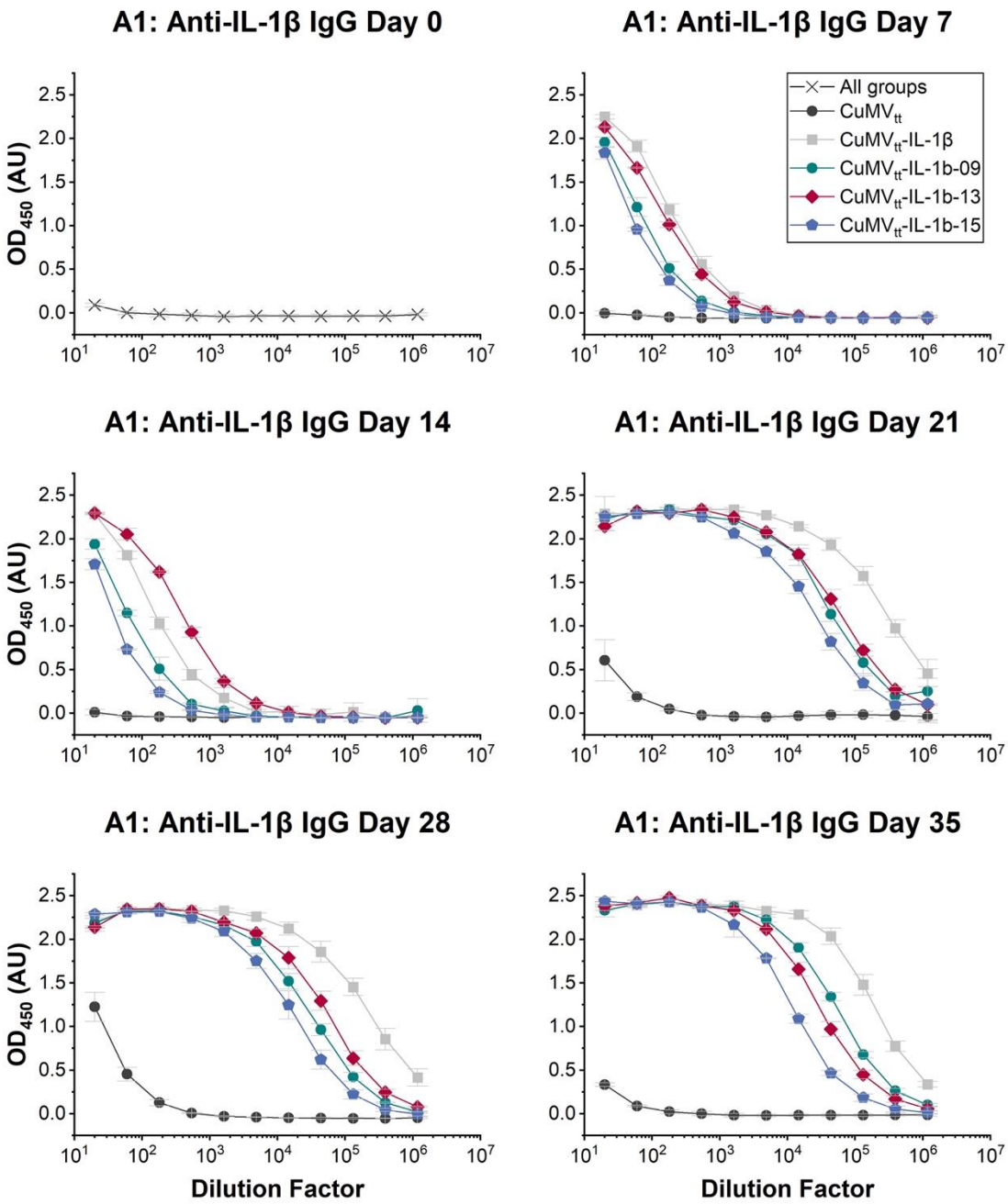

Figure 4.4 – Total anti-IL-1β muIgG from first immunisation attempt. 450-nm absorbance measurements of total anti-IL-1β muIgG detected by goat anti-mouse IgG polyclonal antibodies conjugated to horseradish peroxidase. Error bars representing the standard deviation of three technical replicates.

Curiously, Figure 4.8 also shows the anti-IL-1β response to be more intense than those raised against IL-1b-09, IL-1b-13, or IL-1b-15, a discrepancy apparently independent of cross-reactivity between the antigens. Therefore, this difference in muIgG titres more likely results from heterogeneities produced by the conjugation process (see section 4.2.2.2) than from distinct levels of target immunogenicity. This conclusion is

reinforced by the observation that this difference almost disappears when the same data are plotted for each immunisation group (Figure 4.9) instead of each ELISA specificity.

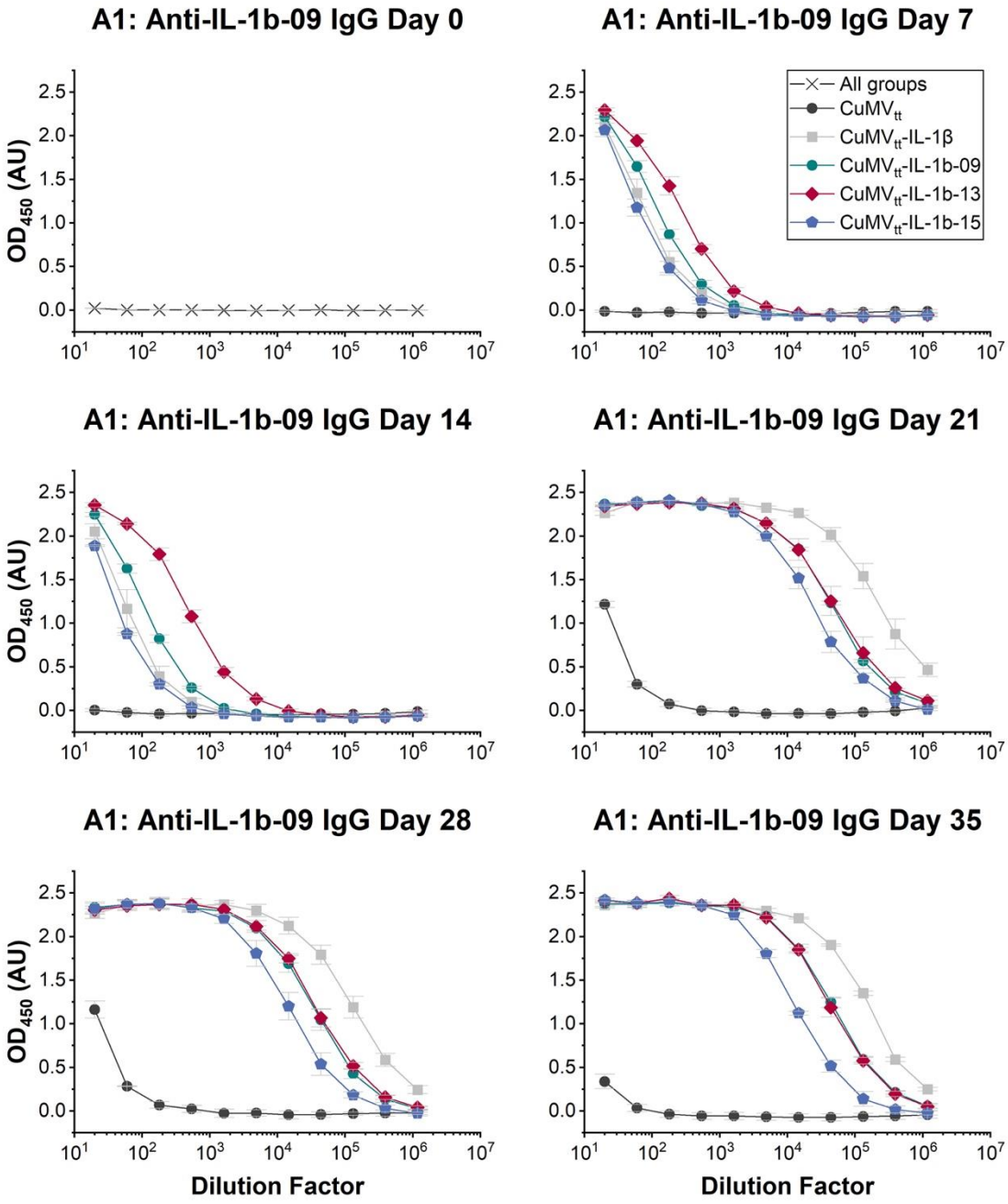

Figure 4.5 – Total anti-IL-1b-09 muIgG from first immunisation attempt. 450-nm absorbance measurements of total anti-IL-1b-09 muIgG detected by goat anti-mouse IgG polyclonal antibodies conjugated to horseradish peroxidase. Error bars representing the standard deviation of three technical replicates.

Figure 4.9 also shows the elicited muIgG responses to equally recognise the four tested antigens, an evidence that the designed mutations had a minimum effect on the

non-neutralising epitopes of the cytokine, which, as discussed in section 4.3.5, contributed for the fast clearance of IL-1β in a second attempt of cytokine challenge.

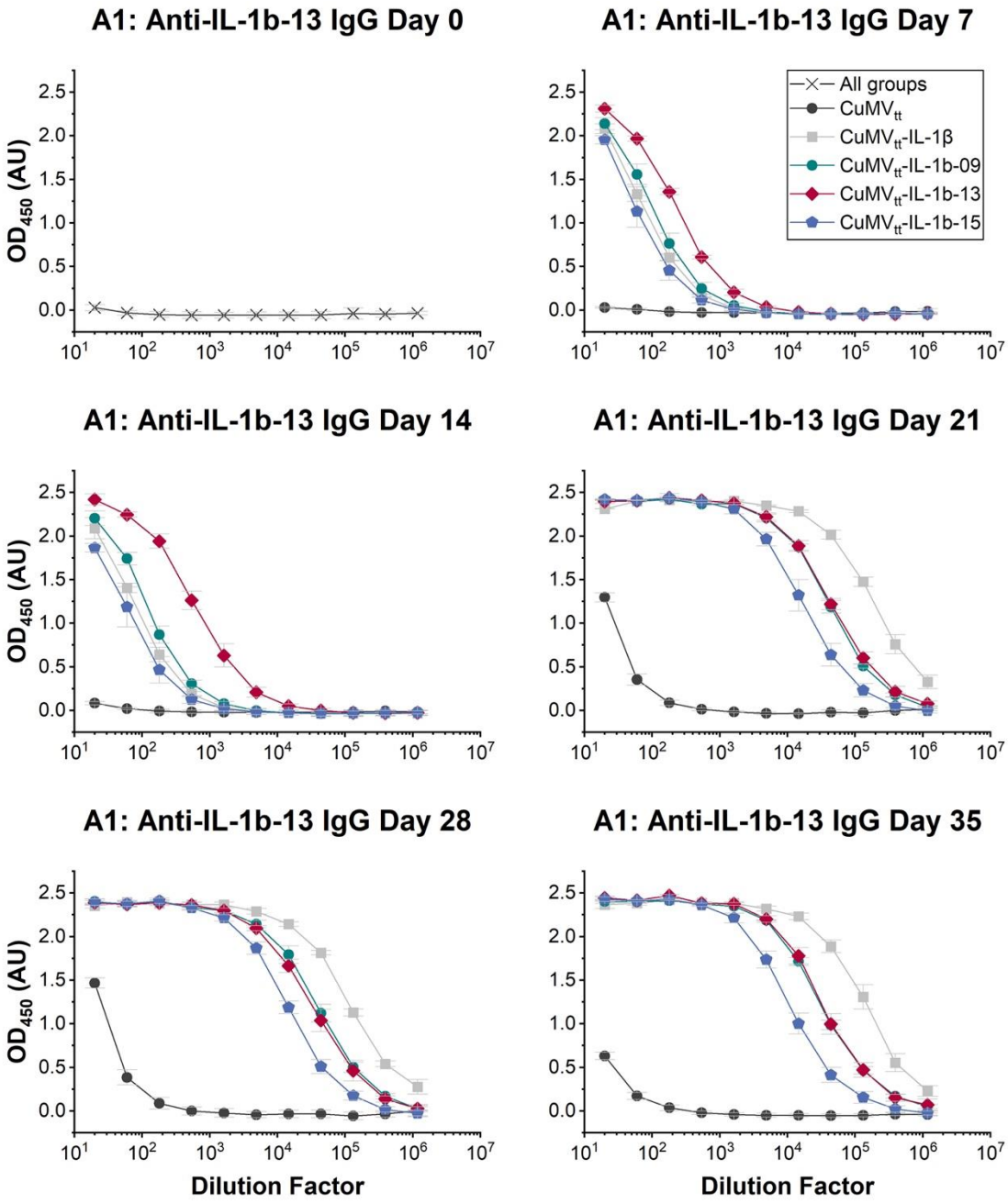

Figure 4.6 – Total anti-IL-1b-13 muIgG from first immunisation attempt. 450-nm absorbance measurements of total anti-IL-1b-13 muIgG detected by goat anti-mouse IgG polyclonal antibodies conjugated to horseradish peroxidase. Error bars representing the standard deviation of three technical replicates.

As explained in section 4.2.2.3, the first challenge attempt failed due to the high dose of IL-1β used (10 µg per animal), which induced severe IgG-mediated anaphylaxis in the groups immunised against the cytokine or the muteins (the control group did not

display symptoms characteristic of anaphylactic shock, e.g., abrupt drop in core body temperature), forcing the experiment's termination. Therefore, to assess the level of protection conferred by the antibody responses against the systemic effects of IL-1β, the immunisation assay was repeated, and a milder challenge (1 µg per animal) was performed at the end of the observation period. Absorbance from IL-1β-specific ELISA assays and their respective muIgG antibody titres over time are plotted in Figure 4.10 and Figure 4.11 (lower panel) below.

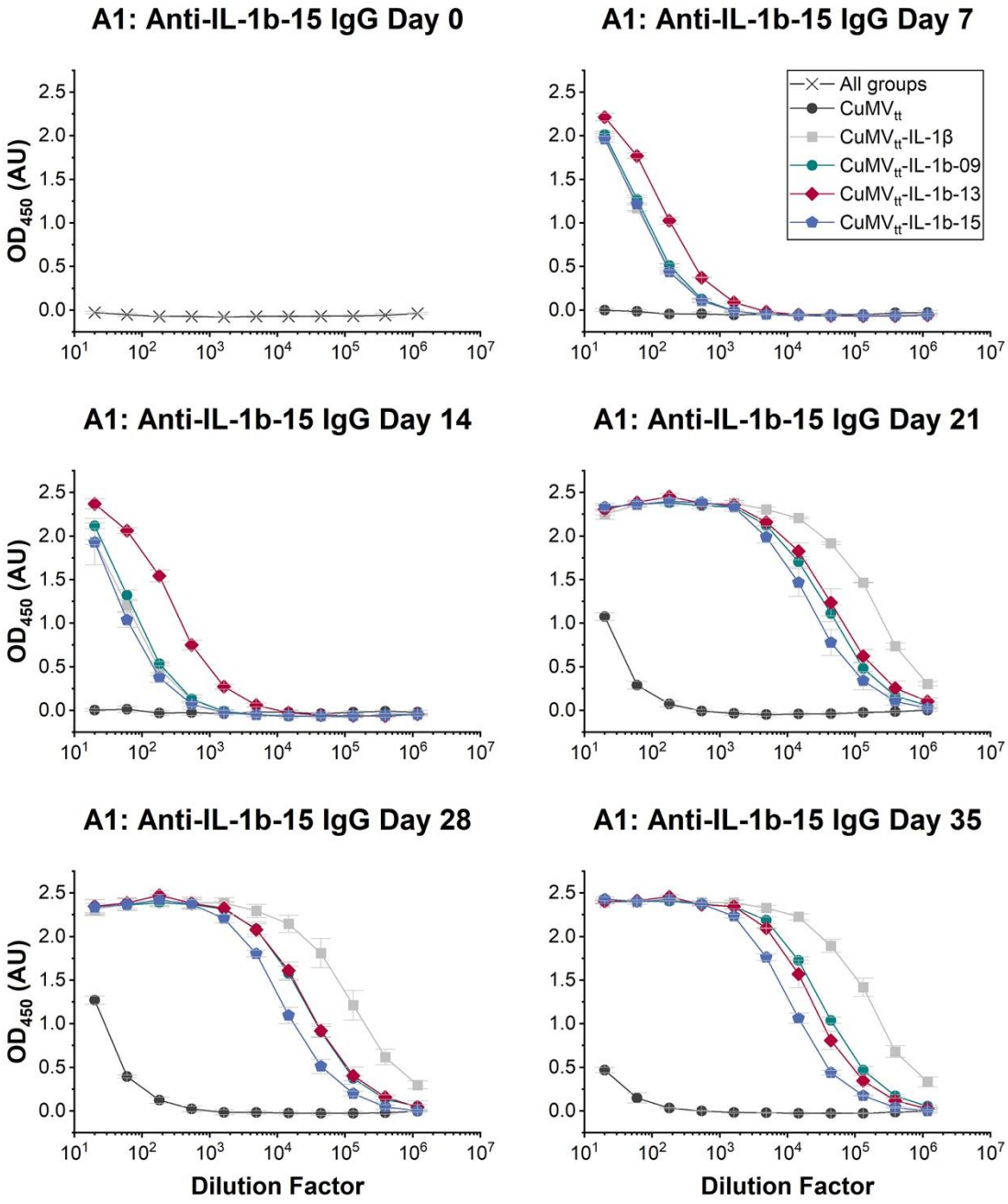

Figure 4.7 – Total anti-IL-1b-15 muIgG from first immunisation attempt.

450-nm absorbance measurements of total anti-IL-1b-15 muIgG detected by goat anti-mouse IgG polyclonal antibodies conjugated to horseradish peroxidase. Error bars representing the standard deviation of three technical replicates.

Figure 4.11 also shows the antibody responses to follow a similar pattern between the two immunisation attempts, with total anti-IL-1β muIgG titres produced by vaccination against the wildtype cytokine consistently higher than those yielded by the muteins coupled to the same VLP.

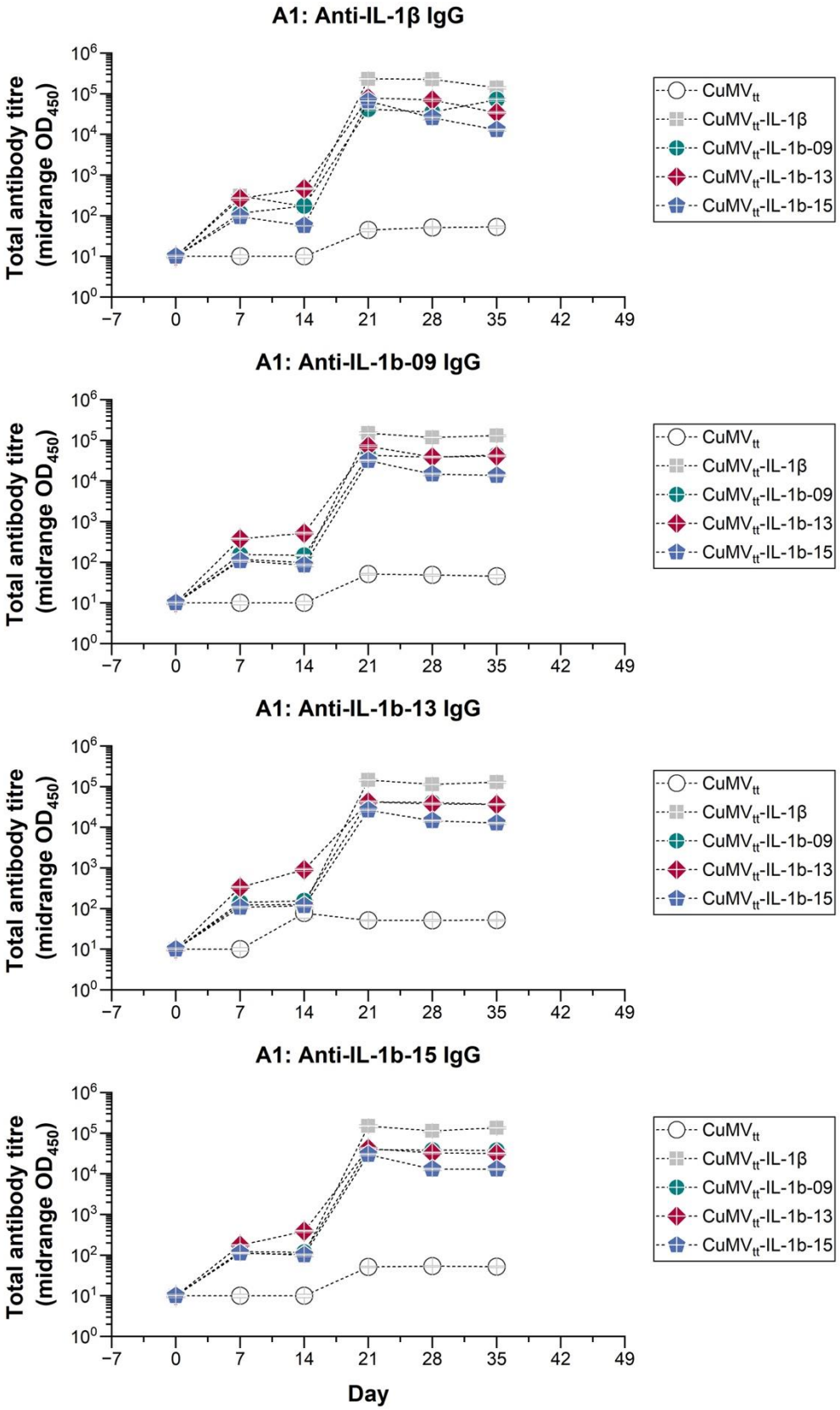

Figure 4.8 – Total mulgG titres from first immunisation attempt. Antibody titres calculated as the midrange point of the OD_{450} measurements shown in Figure 4.4 to Figure 4.7 fitted to the Boltzmann sigmoidal function and plotted for each ELISA specificity. Time counted from first injection. Error bars representing the standard deviation of three technical replicates.

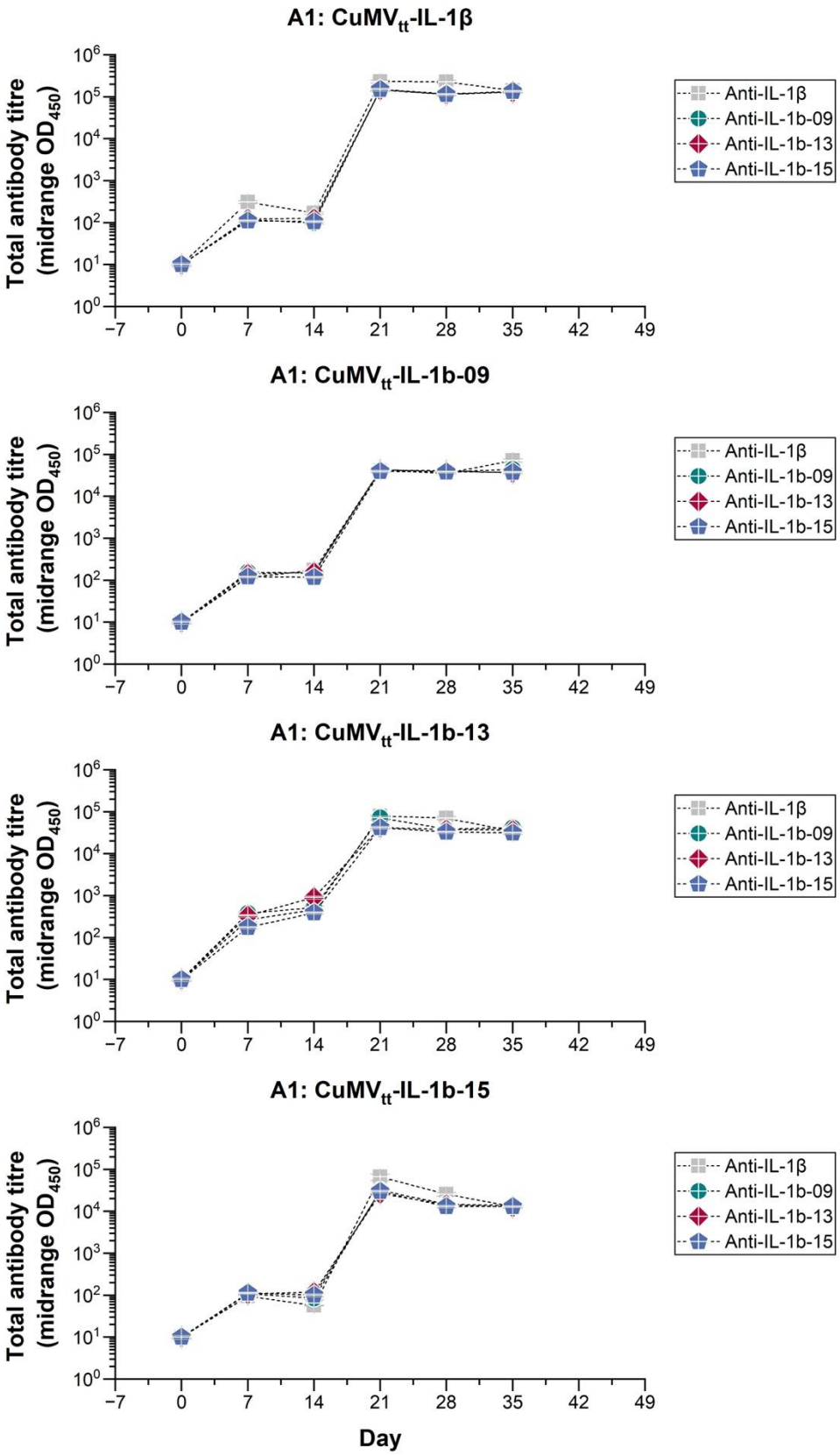

Figure 4.9 – Total mulgG titres from first immunisation attempt. Antibody titres calculated as the midrange point of the OD_{450} measurements shown in Figure 4.4 to Figure 4.7 fitted to the Boltzmann sigmoidal function and plotted for each immunisation group. Time counted from first injection. Error bars representing the standard deviation of three technical replicates.

The dynamics of the curves illustrated in Figure 4.11 also suggests a sustained anti-IL-1β antibody response from the four antigen-immunised groups, although a more reliable conclusion on this question could only be drawn from an experiment performed over a longer period of observation, also having $CuMV_{tt}$-muIL-1β included as homology control.

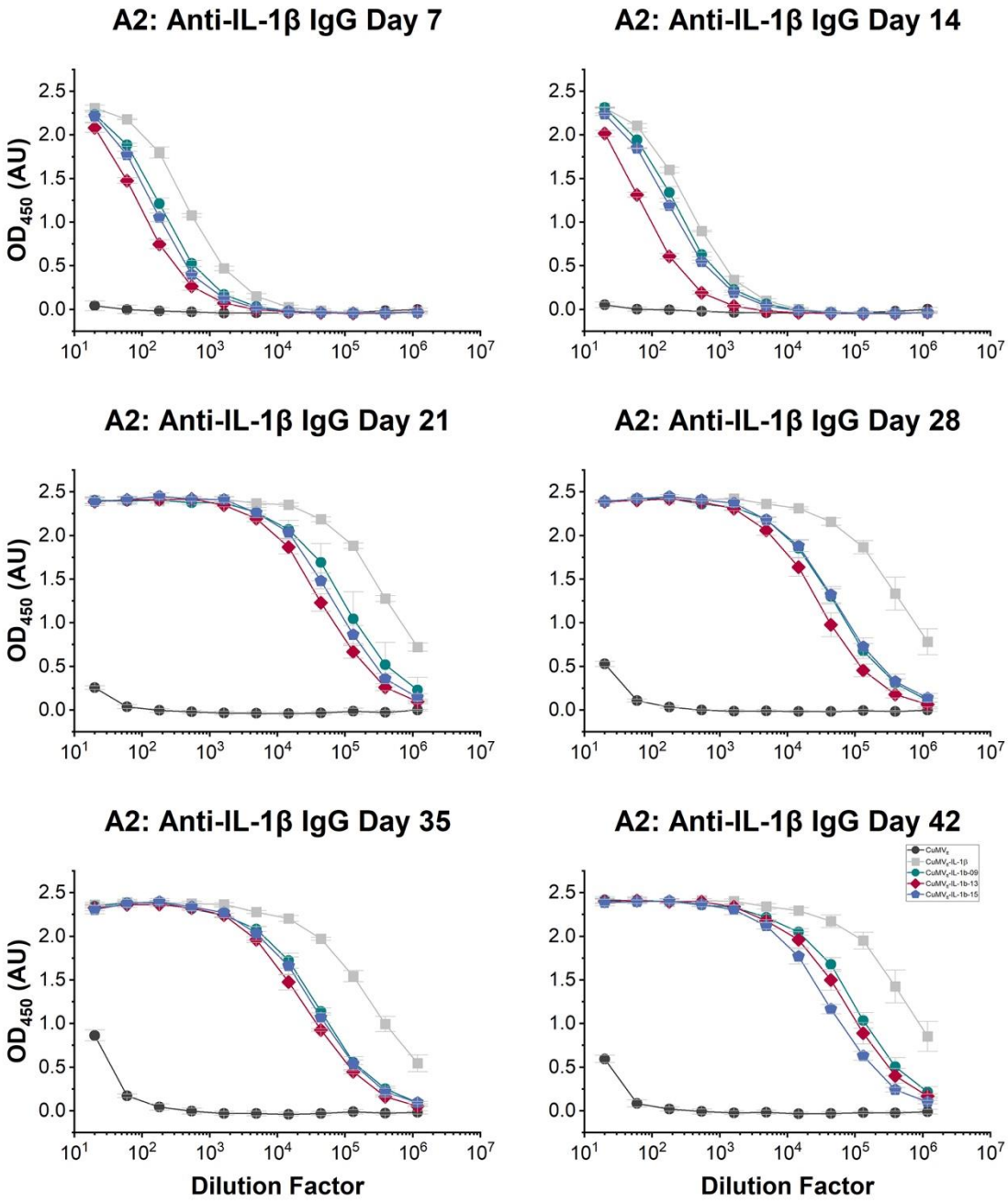

Figure 4.10 – Total anti-IL-1β muIgG from second immunisation attempt. 450-nm absorbance measurements of total anti-IL-1β muIgG detected by goat anti-mouse IgG polyclonal antibodies conjugated to horseradish peroxidase. Error bars representing the standard deviation of three technical replicates.

Finally, some oscillations can be observed in the overall tendency for a plateau of muIgG titres after day 21, which are more pronounced in the results from the second immunisation assay (lower panel of Figure 4.11). These variations, rather than indicating sudden changes in B-cell responses, may instead reflect errors in the measurement procedure (e.g., pipetting during sera pooling) not accounted for in the calculation of the results' dispersity.

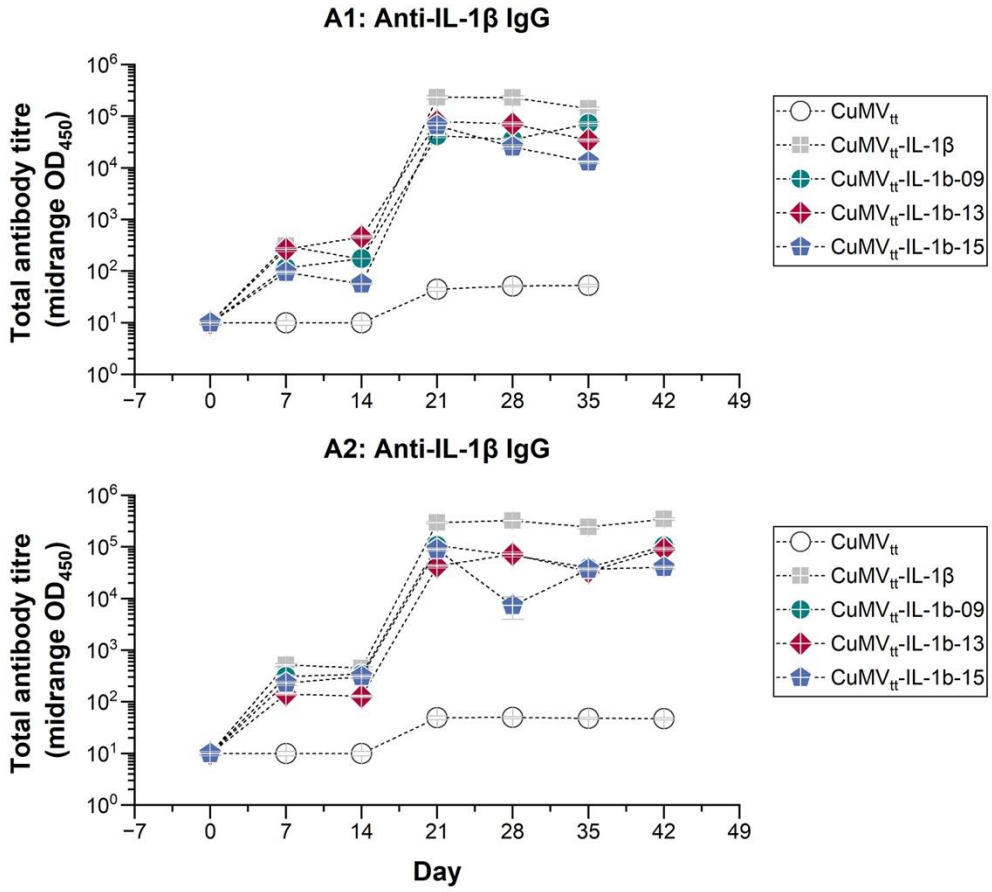

Figure 4.11 –Total anti-IL-1β muIgG antibody titres from first and second immunisation attempt. Antibody titres calculated as the midrange point of the OD_{450} measurements shown in Figure 4.4 (upper panel) and Figure 4.10 (lower panel) fitted to the Boltzmann sigmoidal function and plotted for their ELISA specificity. Time counted from first injection. Error bars representing the standard deviation of three technical replicates.

4.3.3. *In vitro* neutralisation

As the data illustrated in Figure 4.12 show, the antibodies elicited against the designed muteins exhibited a significantly lower capacity for *in vitro* neutralisation of IL-1β (assay performed with pooled sera from day 42 of the second immunisation attempt,

as described in section 4.2.2.4), in particular those from IL-1b-15-immunised animals, which failed to completely block the cytokine from activating the reporter cells. Nonetheless, measurable neutralising antibody titres were obtained from both IL-1b-09- and IL-1b-13-immunised groups, demonstrating the success of the strategy of concentrating the modifications on the interface with D3 of IL-1R2 (see section 2.2.1) in maintaining a degree of cross-reactivity between the muteins and the conserved neutralising sites of IL-1β, e.g., the interface with D1/D3.

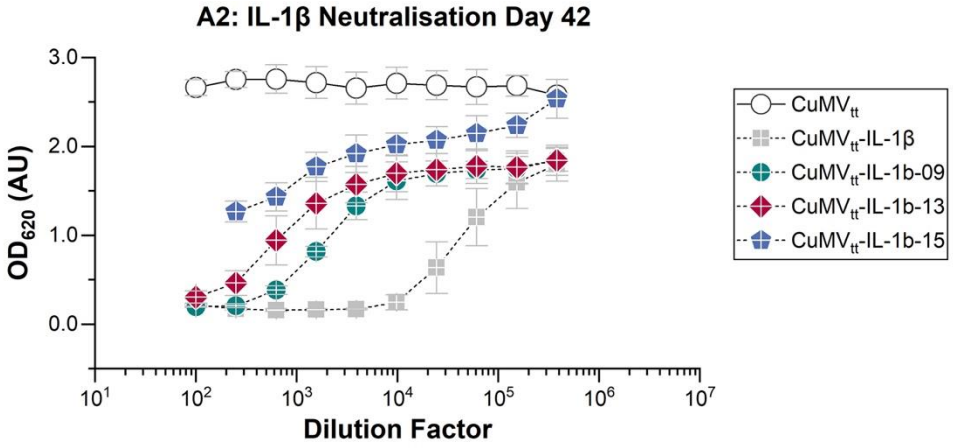

Figure 4.12 – ***In vitro* neutralisation of IL-1β.** 620-nm absorbance measurements of AP-1-inducible SEAP activity from HEK-blue IL-1 cells incubated in the presence of recombinant IL-1β and sera pooled from mice immunised against IL-1b-09, IL-1b-13, IL-1b-15, or the wildtype cytokine. Blood samples collected at day 42 of the second immunisation attempt. Error bars representing the standard deviation of three technical replicates.

The downside of this design approach is the near absence of high-affinity antibodies against the heavily modified areas on the target, thereby not entirely blocking its association with endogenous binding partners, which likely results in residual *in vitro* bioactivity.

4.3.4. Receptor blocking

To further explore this hypothesis, a competition assay (see section 4.2.2.5) was conceived to measure the capacity of the high-affinity antibodies raised against the four tested antigens to block the formation of the ternary complex (IL-1β-sIL-1R1)-sIL-1R3 (see section 2.1.1), a surrogate for signal transduction initiation. Figure 4.13 to Figure 4.15 below illustrate the BLI measurements for the association of both sIL-1R1 and sIL-

1R3 (in solution) to IL-1β (on the sensor) bound to high-affinity antibodies raised against the wildtype cytokine and muteins.

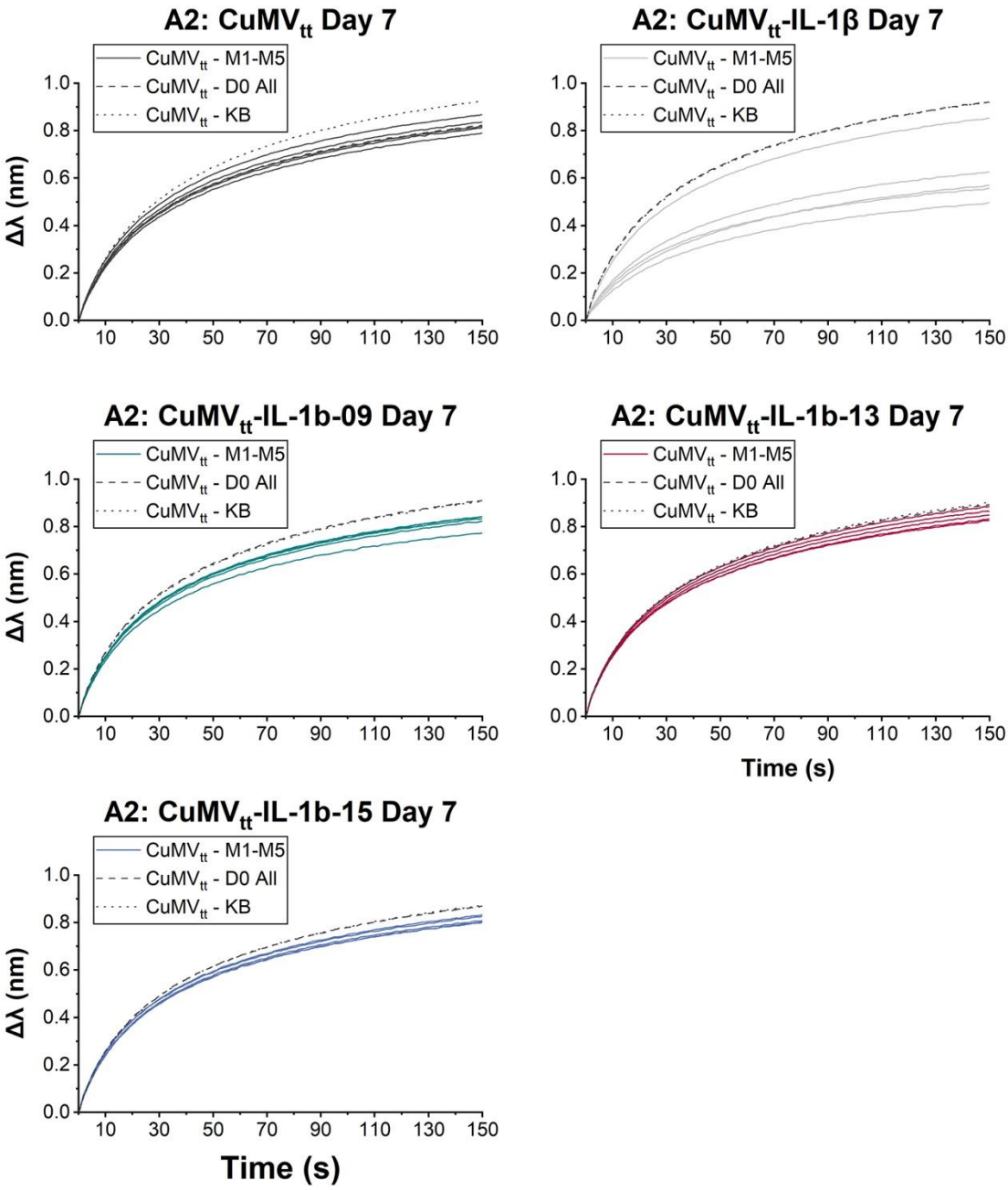

Figure 4.13 – Inhibition of (IL-1β-sIL-1R1)-sIL-1R3 complex assembly by post-prime sera (day 7). Biolayer interferometry measurements from interaction between IL-1β (ligand) and both sIL-1R1 and sIL-1R3 (analyte) after association of high-affinity antibodies from sera collected at day 7 of the second immunisation attempt. Free IL-1β (KB) used as negative control (i.e., 0 % inhibition). Absence of receptors (not shown) used as drift control.

Noticeable in Figure 4.13, (IL-1β-IL-1R1)-IL-1R3-blocking antibodies appeared immediately after the prime injection in the CuMV$_{tt}$-IL-1β-immunised animals,

whereas these pAbs were detected in the other groups only after a boosting shot (Figure 4.14 and Figure 4.15). This result, not observed in the total anti-IL-1β muIgG titres (Figure 4.11, lower panel), indicates an important change in the composition of the antibody responses elicited against the muteins, with a lower number of high-affinity antibodies recognising the neutralising sites of the wildtype cytokine.

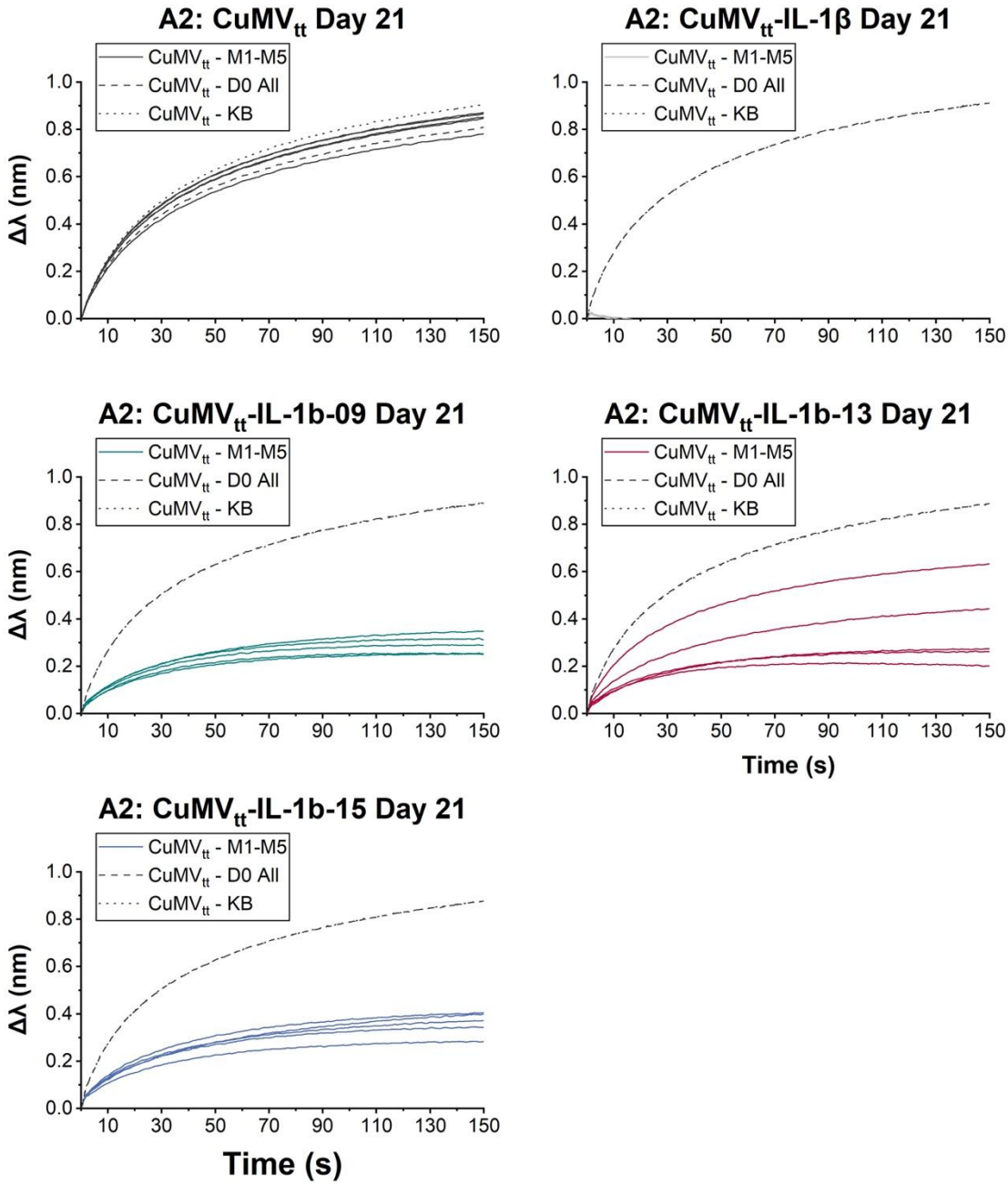

Figure 4.14 – Inhibition of (IL-1β-sIL-1R1)-sIL-1R3 complex assembly by post-boost sera (day 21). Biolayer interferometry measurements from interaction between IL-1β (ligand) and both sIL-1R1 and sIL-1R3 (analyte) after association of high-affinity antibodies from sera collected at day 21 of the

second immunisation attempt. Free IL-1β (KB) used as negative control (i.e., 0 % inhibition). Absence of receptors (not shown) used as drift control.

More interestingly, as shown in Figure 4.16, the capacity of the antibodies raised against the muteins to block the assembly of the (IL-1β-IL-1R1)-IL-1R3 complex under the assay conditions reaches a plateau of ≈ 60 % at day 21, suggesting that part of the cytokine (likely the one bearing the surface modifications) remained free to interact with the signalling-competent receptors, which may explain the lower neutralising titres measured for the muteins *in vitro* (Figure 4.12).

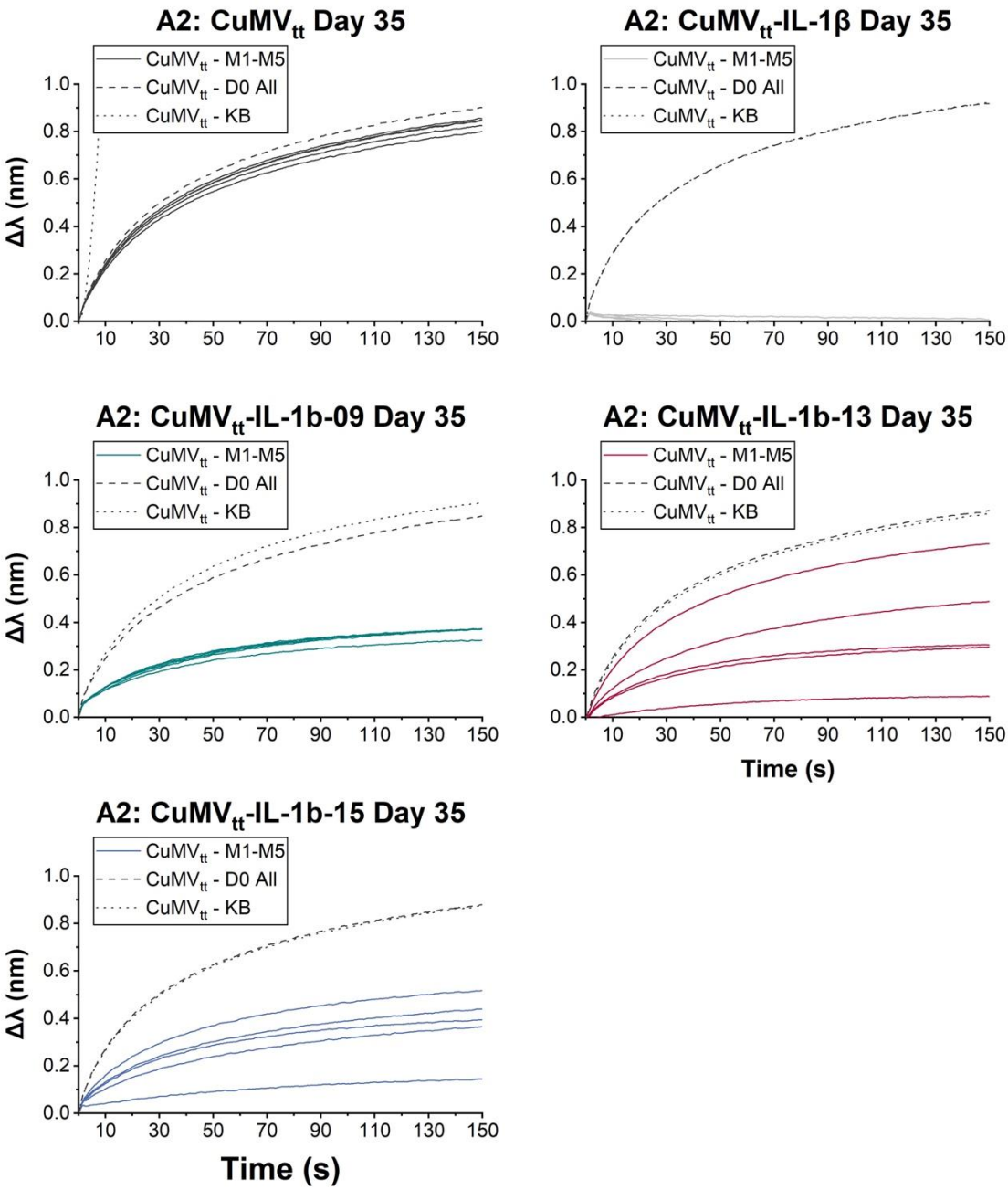

Figure 4.15 – Inhibition of (IL-1β-sIL-1R1)-sIL-1R3 complex assembly by post-boost sera (day 35). Biolayer interferometry measurements from interaction between IL-1β (ligand) and both sIL-1R1 and sIL-1R3 (analyte) after association of high-affinity antibodies from sera collected at day 35 of the second immunisation attempt. Free IL-1β (KB) used as negative control (i.e., 0 % inhibition). Absence of receptors (not shown) used as drift control.

Although not totally expected, this result illustrates well how surface redesigning can bias the B-cell response towards particular sites of the modified antigens, therefore bypassing others. A potential application of this technique would be the elimination of undesired cross-reactivity between similar antigens (e.g., the four serotypes of dengue virus),[76] preventing the emergence of disease-enhancing antibodies upon vaccination.

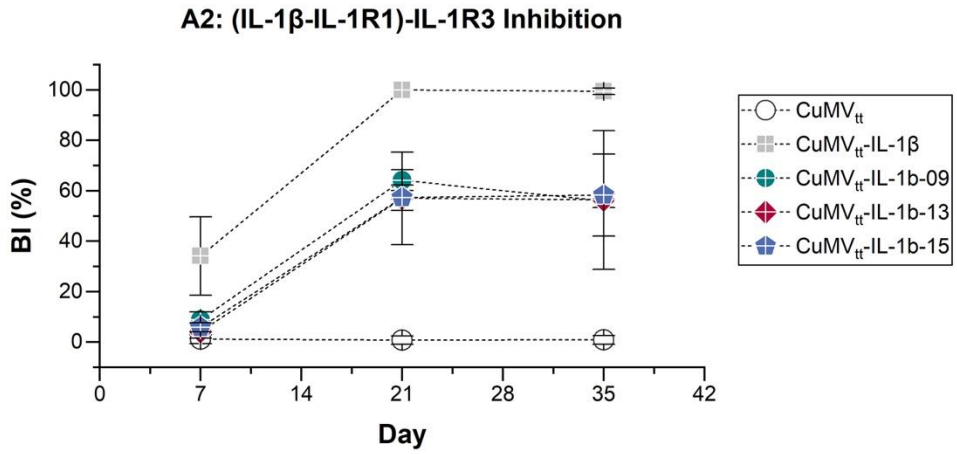

Figure 4.16 – (IL-1β-sIL-1R1)-sIL-1R3 complex assembly inhibition. BI index calculated as the proportional reduction in the maximum association of sIL-1R1 and sIL-1R3 to IL-1β ($\Delta\gamma$ curves of antibody-free ligand, KB) by sera collected across the second immunisation assay. Error bars representing the standard deviation of 4-5 biological replicates.

Finally, it is important to notice the small deviation in BI indexes for $CuMV_{tt}$-IL-1β, significantly lower than the variability calculated for the other sera, indicating that the detection range of the assay may had been insufficient to captured the true difference between the groups.

4.3.5. Immune protection

Contrasting with what would be expected from the previously discussed results, immunisation against all three selected muteins provided the animals full protection against the proinflammatory effects of IL-1β (Figure 4.17, upper panel), verified by the negligible increases in muIL-6 secretion upon cytokine challenge (described in section 4.2.2.3). This apparent enhancement in cytokine neutralisation by the antibodies raised against the muteins may actually be a consequence of fast target clearance driven by the phagocytosis of the instantly formed immunocomplexes. Such effect (not measured in the *in vitro* assays discussed in sections 4.3.3 and 4.3.4) may have been potentiated by a large number of antibodies (including non-blocking IgGs) – cross-reacting against the wildtype cytokine, as suggested by the high muIgG responses obtained from all groups.

More importantly, these results do not show the presence of "disease-enhancing" antibodies in the animals immunised against the muteins, an issue previously observed by Spohn and colleagues[58] for variants IL-1β bearing a smaller number of mutations.

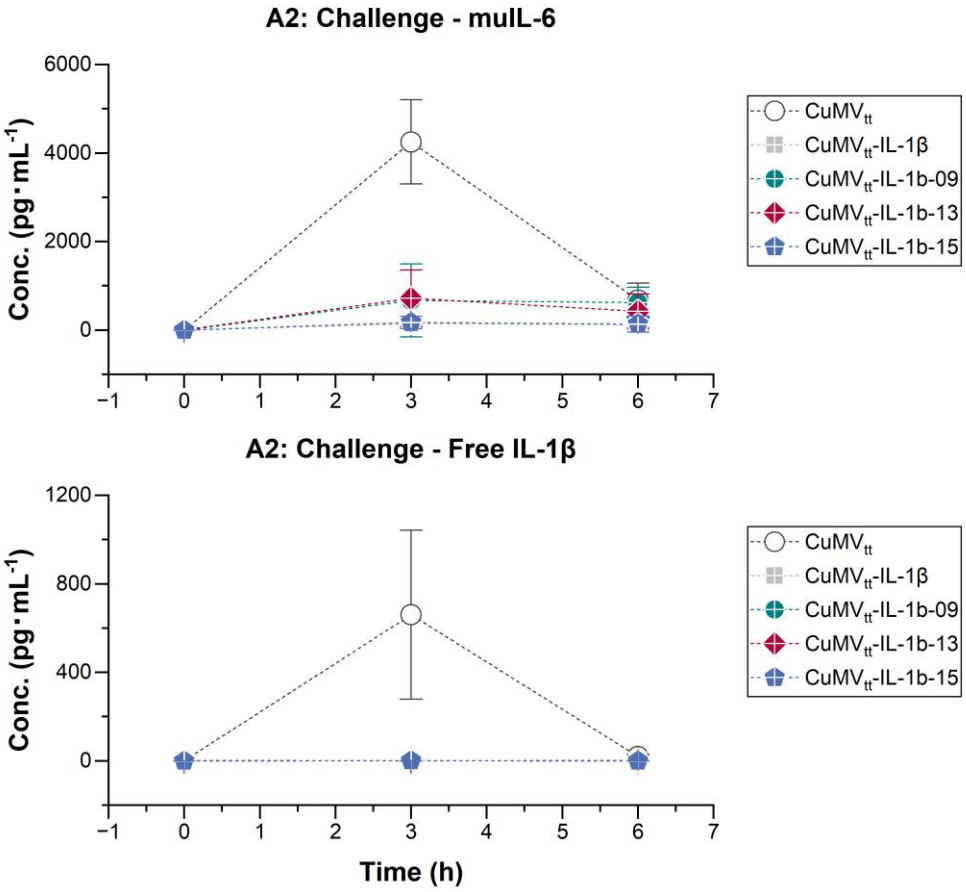

Figure 4.17 – In vivo neutralisation of IL-1β. Quantitation of mu-IL-6 (upper panel) and immunologically available (i.e., not bound to antibodies) IL-1β (lower panel) after intraperitoneal injection of 1.0 µg of the cytokine. Challenge performed at day 42 of the second immunisation attempt. PBS as negative control. Error bars representing the standard deviation of 4-5 biological replicates.

Finally, as shown in the lower panel of Figure 4.17, no immunologically available IL-1β was detected throughout the challenge, which suggests that patients of SAIDs vaccinated against one of the tested muteins could be immune to the effects of residual IL-1β activity even in the event of a severe flare (see section 0).

4.4. Conclusions

In this chapter, the effects of the designed mutations on the detoxification of IL-1β and on the capacity of the antibody responses raised in mice against the muteins to

recognise and neutralise the cytokine both *in vitro* and *in vivo* were assessed. To this end, the muteins IL-1b-09, IL-1b-13, and IL-1b-15 as well as wiltype IL-1β were tested for their bioactivity in a cell-based assay. The results, discussed in section 4.3.1, showed IL-1β's potent pro-inflammatory activity to be almost entirely absent in the selected muteins, demonstrating the efficacy of the chosen surface re-design approach in altering the cytokine's endogenous interaction patterns.

Discussed in section 4.3.2, multi-target ELISA screenings showed the total muIgG antibodies raised against the muteins to recognise IL-1β nearly at the same level as those elicited against the WT cytokine itself. This high level of cross-reactivity, however, did not translate into complete neutralisation of the target *in vitro*, given that residual cytokine activity was detected in both cell-based (see section 4.3.3) and protein-protein interaction (section 4.3.4) assays. Interestingly, the BLI assays also showed the high-affinity portion of the anti-mutein antibodies to only partially block IL-1β from interacting with sIL-1R1 and sIL-1R3, suggesting that the mutated area of the cytokine remained free to bind and recruit the two signalling-competent receptors.

Interestingly though, the animals immunised against IL-1b-09, IL-1b-13, and IL-1b-15 exhibited similar levels of protection against the systemic inflammatory effects of the cytokine as those who were administered the $CuMV_{tt}$-IL-1β conjugate instead. Discussed in section 4.3.5, this result suggests that the losses in *in-vitro* neutralisation caused by the designed mutations may have been compensated by fast target clearance promoted by the large number of antibodies cross-reacting against the non-neutralising sites of the cytokine. Unfortunately, a few attempts to test this hypothesis (by passively immunising naïve mice with canakinumab, gevokizumab, or a combination of both 24 h prior to IL-1β challenge) failed due low reproducibility.

Finally, a concern raised during the elaboration of the design strategy was the possibility that the modifications performed on IL-1β's surface could lead to the production of non-neutralising antibodies that, when bound to the endogenous cytokine, would potentiate its already strong pro-inflammatory activity. As the results discussed in section

4.3.5 demonstrate, however, this disease-enhancing effect, previously observed for a version of IL-1β containing a single point mutation (see section 1.4.1), was not detected in the immunisation assay performed with IL-1b-09, IL-1b-13, and IL-1b-15.

Chapter V. Conclusions and outlook

Through a computational approach, this thesis explored potential solutions to issues hampering the development of a virus-like particle (VLP)-vectored therapeutic vaccine targeting interleukin 1β, the key mediator in the pathogenesis of systemic autoinflammatory diseases (SAIDs). More specifically, this project aimed at bypassing, via antigen optimisation, potential interactions between the IL-1β molecules displayed by the carrier and the cytokine's endogenous receptors, in particular the soluble version of IL-1R2, a negative regulator of IL-1α/β (see section 0). The desired result of this process is a safer and more immunogenic vaccine suitable for the treatment of SAIDs and other chronic inflammatory diseases.

In previous attempts of developing an IL-1β-based vaccine (see section 1.4.1), the authors report having reduced the risk of vaccine-induced systemic inflammatory reactions by mutating the cytokine's surface so that its affinity for the primary receptor IL-1R1 remains below the threshold for triggering a cellular response. Though effective in improving the safety profile of the vaccine, these modifications proved insufficient to overcome the high immunotolerance exhibited by humans against IL-1β, which has rendered its use as therapeutic immunogen unviable. Based on the hypothesis that interactions with other endogenous receptors, in particular IL-1R2, are the main cause of IL-1β's poor antigenicity in primates (see section 1.4.2), a new design strategy was proposed so that large areas of the antigen's surface could be altered without compromising its cross-reactivity with the wildtype cytokine.

This strategy consisted of disrupting these interactions by substituting key residues for others with distinct biochemical properties, for instance, replacing a histidine participating in a salt bridge with a non-polar or negatively charged amino acid of similar size. Since the number of possible combinations of mutations that could be performed on the 12 residues selected for substitution was vast (see section 2.2.1), a computational design framework was applied so that only the sequences with a reasonable probability of presenting the desired properties would be selected for subsequent *in vitro*

and *in vivo* studies. The resulting pipeline makes use of two well-established methods of molecular modelling – namely stochastic energy sampling and molecular dynamics – to determine the combination of mutations that result in minimal disturbances in the overall structure of the cytokine, particularly in the regions kept unchanged for better antibody cross-reactivity (see section 2.2.1).

The Monte Carlo-based sampling simulations described in section 2.2.2 yielded a large number of sequences that passed a set of stringent design filters (see section 2.3.1). Of those, only 14 were selected, based on their predicted structural properties, for an *in-silico* analysis of their stability in solution under standard conditions of temperature, pressure, and ionicity (see section 2.2.3). The results of the performed molecular dynamics simulations (discussed in section 2.3.2) showed all selected designs to retain their predicted conformations in the emulated environment, displaying structural movements no broader than those observed for the design template. In practical terms, this meant that the modelled muteins were unlikely to precipitate and/or aggregate when exposed to the same ordinary conditions in which IL-1β was expressed and purified. In this way, all 14 sequences were carried forward for biophysical characterisation, the second major step in the design process.

The 14 designed muteins were then expressed in *E. coli* under the same conditions as IL-1β, yielding, as predicted, similar amounts of purified protein (3.3.1). Further evidencing the accuracy of the designed models, results from size-exclusion chromatography – the last step of the purification process – showed the hydrodynamic profiles of the muteins to be nearly identical to that of the wildtype cytokine (section 3.3.1). The purified muteins were then submitted to a series of kinetics assays aimed at assessing their interaction with neutralising monoclonal antibodies and IL-1β's decoy receptor IL-1R2.

Biolayer interferometry (BLI) assays demonstrated that, as intended (see section 2.1.2), the modifications performed on IL-1β's surface had minimal impact on the binding kinetics between the cytokine and canakinumab, a clinically relevant monoclonal

antibody. Higher variability was observed in the measurements of affinity with which gevokizumab – another anti-IL-1β neutralising mAb – interacts with the muteins (section 3.3.2). This increased heterogeneity was expected due the proximity of two mutation points (K209 and K210) to gevokizumab's binding site (see section 2.1.2).

Another series of BLI assays measured the affinity of the muteins for the ectodomain of IL-1R2. With the exception of IL-1b-02, IL-1b-06, and IL-1b-07, all modified versions of IL-1β exhibited considerably lower affinities for the decoy receptor than the wildtype cytokine, resulting from a sharp increase in their dissociation rates. Of those, IL-1b-09, IL-1b-13, and IL-1b-15 yielded values of K_D at least 50,000 times lower than IL-1β's, to a range of the receptors IL-1R1 and IL-1R3 (see section 3.3.2). In theory, this reduction in binding affinity should suffice to bypass the inhibitory effects of sIL-1R2, improving the immunogenicity of the cytokine when presented in the context of a vaccine for humans.

To investigate if these differences in binding affinity were due to the nature of the substitutions or to minor conformational disruptions not detected in the previous assays, the structures of two muteins with the highest affinities for sIL-1R2 were compared, together with IL-1b-09, IL-1b-13, and IL-1b-15, to a structure of IL-1β determined by nuclear magnetic resonance spectroscopy. To this end, chemical shift perturbation analyses were performed on ^{1}H-^{15}N HSQC spectra acquired for the five muteins, showing that IL-1b-02 and IL-1b-07 as well as the muteins with the lowest affinities for sIL-1R2 underwent only minor structural movements in the vicinity of the mutated residues (see section 3.3.4). These results confirmed the success of the design strategy in altering the binding kinetics of the cytokine while preserving its native conformation.

To ensure that the loss in cross-reactivity between IL-1b-09, IL-1b-13, and IL-1b-15 and IL-1β would not be due to instabilities not predicted by the MD simulations, the melting temperatures of the three selected muteins were determined by differential scanning calorimetry coupled to circular dichroism and compared to that of the wildtype cytokines. The resulting spectra indicated that the four proteins are equally stable across

a range of temperatures of up to ≈ 40 °C, irreversibly denaturing at ≈ 53 °C and above (see section 3.3.3). With their T_ms almost identical to IL-1β's, any difference in the immunological properties of the muteins was considered unlikely to be due to stability issues.

These immunological properties were then assessed in the final step of the design process: an immunisation assay in which wildtype mice were administered, in a prime-boost regimen, each of the three selected muteins conjugated to the virus-like particle $CuMV_{tt}$. Analysis of the total antibody titres (section 4.2.2.4) revealed a high level of cross-reactivity between the muteins and IL-1β (see section 4.3.2), which, unexpectedly, did not translate into similarly high neutralising antibody titres (sections 4.3.3). Nonetheless, the immune responses elicited against the three muteins proved equally protective *in vivo* against the pro-inflammatory effects of IL-1β as that raised against the cytokine itself (see section 4.3.5), suggesting that fast target clearance – characteristic of polyclonal responses – may have compensated for the observed decrease in the number of cross-reactive neutralising antibodies.

Conceived to emulate a severe disease flare, the cytokine challenge performed at the end of the immunisation assay also confirmed the absence a of a disease-enhancing effect caused by non-neutralising antibodies cross-reactive against IL-1β. This effect, also not detected in the *in vitro* neutralisation assays (see section 4.3.3), had previously been observed by Spohn and colleagues for a version of the cytokine bearing just a single mutation close to the protein's C-terminus.[58] These results support the assumption that either IL-1b-09, IL-1b-13, or IL-1b-15 would exhibit a favourable safety profile in more advanced pre-clinical studies (e.g., immunisation of non-human primates), especially considering that none of the three muteins exhibited significant IL-1 activity *in vitro* and, therefore, cannot induce a pro-inflammatory response characteristic of IL-1β (see section 4.3.1).

In summary, this project has demonstrated the feasibility of a structure-guided surface re-design approach for the optimisation of a therapeutic antigen based on IL-1β.

The strategy, which focused on maintaining the structural characteristics of the wildtype cytokine while implementing numerous surface modifications with potential to disrupt its interactions with endogenous receptors, proved successful in yielding candidates with satisfactory biophysical and immunological properties. To demonstrate the viability of these vaccine candidates as therapeutics against SAIDs and other chronic inflammatory diseases, however, new immunisation assays performed in presence of human IL-1 receptors are required. For that purpose, a transgenic mouse strain knocked-out for muIL-1R2 and knocked-in for huIL-1R2 is being generated. If the results of an immunisation assay performed on these mice prove the muteins to be more immunogenic than the wildtype IL-1β, the natural step will be immunisation of non-human primates prior to first-in-human studies.

Regarding the design pipeline developed for this project, efforts are under way to optimise its computational methods so that more accurate models can be produced faster and at a lower processing cost. Similar improvements are being carried out on the *in vitro* screenings, with the replacement of less informative techniques (i.e., nuclear magnetic resonance spectroscopy) for more informative ones (i.e., high throughput crystallography).

APPENDICES

A1. The four classic periodic fevers

In this particular group of SAIDs, mutations in genes coding for sensory or regulatory components of the inflammasomes (e.g., NLRP3, see A1.3) lead to overactivation of Caspase-1, ultimately resulting in excessive activation and release of IL-1β and IL-18.[77,78] Belonging to this category are the four classic recurrent fevers: familial Mediterranean fever (FMF), mevalonate kinase deficiency (MKD), cryopyrin-associated periodic syndrome (CAPS), and tumour necrosis factor-associated periodic syndrome (TRAPS), as well as the less-understood diseases associated to NLRC4 or NLRP12 mutations. Due their clear pathogenic mechanism, among other factors, FMF, MKD, CAPS, and TRAPS are the preferred targets for new therapies for SAIDS, and hence are succinctly described below.

A1.1 Familial Mediterranean Fever (FMF)

The most prevalent monogenic SAID, FMF affects mainly ethnic groups from the Eastern Mediterranean basin, as the Turks, Arabs, Armenians, and Sephardic Jews,[79] although the disease has also been identified in 32 % of Japanese patients with unexplained fever.[80] In Turkey, from where most of the epidemiological studies on FMF originate, the prevalence of the disease in the general population has been estimated in between 1:1,000 and 1:400,[81] with most cases occurring in the Black Sea and Central Anatolia regions.[82] Worldwide, it is believed that approximately 100,000 individuals suffer from FMF.[81]

The disease results from mutations in the *MEFV* gene,[83,84] which codes for pyrin, an ≈ 95 kDa intracellular pattern-recognition receptor (PRR) expressed almost exclusively by peripheral blood leucocytes, mostly by mature granulocytes.[85] Its pyrogenic function is triggered in response to toxin-mediated RhoA-GTPase inactivation, mechanism employed by several pathogenic bacteria (including *B. pertussis*, *C. botulinum*,

and *Y. pestis*) to evade phagocytosis.[86] The consequence is the inhibition of PKN1/2 activity, resulting in the release of 14-3-3ε/τ phosphoserine binding protein and subsequent dimerization of pyrin, which then interacts with the apoptosis-associated speck-like adaptor complex (ASC) to form the pyrin inflammasome.[87] Though the precise mechanism remains unclear, loss of affinity for PKN1/2 and/or 14-3-3ε/τ (resulting from mutations at or around their binding sites) is suggested by some authors as a likely cause for the spontaneous activation of pyrin observed in FMF.[88,89]

Originally described as purely autosomal recessive,[90] FMF has been shown to also affect heterozygous carriers of mutations in the pyrin gene.[91,92] To date, 61 out of the 393 *MEFV* variants currently reported to the INFEVERS database,[93,94] are classified either as definitely pathogenic or as having > 90 % chance of causing the disease.[95-97]. Interestingly, patients carrying one or two mutations of high penetrance[98] (e.g., E148Q on exon 2 and M694I on exon 10)[99] are more likely to suffer from periodic fever attacks than those bearing less frequent mutations[100] (e.g., T267I and P369S on exons 2 and 3, respectively).[98]

In addition to fever, the typical FMF phenotype includes recurrent attacks of pleuritis and peritonitis[101,102] accompanied by acute phases of synovitis,[100] which not infrequently evolves to peripheral spondyloarthritis.[103] Although several biomarkers have been proposed (including circulating active IL-1β[104] and, more recently, serum resistin, calpronectin, and neopterin),[105,106] clinical assessment remains the standard procedure for FMF diagnosis.[107] Responsiveness to colchicine is high among FMF patients, with only ≈ 12-15 % requiring a second line treatment, usually based on biological IL-1β inhibitors.[108]

A1.2 Mevalonate Kinase Deficiency (MKD)

MKD is a rare autosomal recessive metabolic disorder that equally affects males and females.[109] Unlike FMF, MKD distribution is not ethnically biased,[110] even though the majority of the documented cases come from the Netherlands, likely due the

high incidence of mevalonate kinase mutations (in particular *MVK* V377I)[111] in the Dutch population. The global prevalence of MKD is unknown, with estimation attempts being hampered by the significant number of undiagnosed/unreported patients, probably a result of the inherent rarity of the disease.[112]

The disease is caused by mutations in the *MVK* gene[113] that result in reduction or abolishment mevalonate kinase's function.[114] MVK catalyses the phosphorylation of mevalonate into mevalonate-5-phosphate, a key step in the synthesis of isoprenoids and cholesterols.[115] Reduction or abrogation of MVK activity results in accumulation of mevalonate (which may lead to MEVA, described below) and depletion of geranylgeranyl-pyrophosphate (GGPP), which, in addition to being a precursor of diterpenes and diterpenoids, functions as an anchor for GPCRs and other membrane-associated proteins.[116,117] Suppression of RhoA geranylgeranylation (and, consequently, its localisation on the cell membrane) via MVK downregulation is, therefore, the underlaying mechanism of pyrin overactivation in MKD.[118,119]

At the milder end of MKD phenotypic spectrum, hyperimmunoglobulinemia D syndrome appears early in childhood, having elevated serum IgD as the main blood marker. Rash and recurrent attacks of intense fever are the main clinical manifestations of HIDS.[1] Other symptoms include abdominal pain, adenopathy, pharyngitis, and mucocutaneous ulcerations.[112] These flares typically last 4-7 days, and may either be triggered (e.g., by illness, injury, excessive physical activity, among other physiological stressors) or occur spontaneously, in which case they may be repeated in a cyclical patter every 4-6 weeks.[10]

Also manifested in the first few months of life, mevalonate aciduria (MEVA) is the rarest and most severe phenotype of MKD. In addition to HIDS symptoms, MEVA patients typically exhibit dysmorphisms, mental and psychomotor retardation, and progressive visual impairment.[120] Elevated serum IgD and IgA are common findings in MEVA.[112] Although simvastatin[121] and anakinra[122] have shown some beneficial

effects for mildly affected patients, no effective treatment has yet been established for MEVA, with the disease most often leading to death in infancy.[112]

A1.3 Cryopyrin-associated Periodic Syndrome (CAPS)

CAPS is a rare disease, with prevalence estimated in 1-5 cases per million.[123-125] It is manifested as a spectrum of symptoms that, regarding mainly their extension and degree of severity, are grouped into three phenotypes presenting an increasing level of cutaneous, musculoskeletal, ocular, and central nervous system (CNS) involvement: familial cold autoinflammatory syndrome (FCAS), chronic infantile neurological cutaneous and articular (CINCA) syndrome (aka, Muckle-Wells syndrome, MWS), and neonatal onset multisystem inflammatory disease (NOMID).[126]

FCAS flares are triggered by generalised exposure to cooling temperatures (sometimes as mild as that of an airconditioned room), and present rigours (fever with chills), urticaria-like rashes, arthralgia, myalgia, conjunctivitis, and keratitis as the most frequent symptoms.[127] In addition to FCAS symptoms, CINCA patients may also experience episcleritis, papilledema, oligoarthritis, and intermittent aseptic meningitis.[128] Cold is a less important factor in CINCA, which flares can also be triggered by stress, infection, or trauma.[128] Finally, in NOMID – the most severe phenotype of CAPS – musculoskeletal and neurological involvement is more noticeable, with clinical manifestations including chronic aseptic meningitis, brain atrophy, epiphyseal bone overgrowth, and limb length discrepancies, in addition to CINCA symptoms.[128] Colchicine is the first line of treatment for CAPS. Clinical manifestations, responsiveness to first-line therapy, and genetic screening constitute the primary diagnostic strategy.[10]

Caused by mutations in the cryopyrin-encoding NACHT, LRR, PYD domains-containing protein 3 (*NLRP3,* aka *CIAS1* or *PYPAF1*) gene, the disease is predominantly autosomal dominant,[129] with only a few cases being reported to result from somatic mutagenesis (i.e., mosaicism).[130] Of the 264 *NLRP3* variants currently deposited in the INFEVERS database,[93] 117 are classified as pathogenic or as having > 90 %

chance[96] of causing CAPS or a similar autoinflammatory disorder. Although the majority of the pathogenic mutations fall into the NACHT domain of cryopyrin, there is no apparent correlation between disease phenotype and the mutation site.

Cryopyrin is the sensory component of the NLRP3 inflammasome, expressed predominantly in macrophages and activated in response to PAMPs and DAMPs associated with membrane damage,[131] in particular viruses[132,133] and crystals.[134-136] Activation of this inflammasome includes the upregulation of its components via NF-κB upon signalling by TLRs (e.g., TLR2 and TLR4) and proinflammatory cytokines (e.g., TNFα and IL-1β).[137,138] At the post-translational level, complex formation is triggered by secondary signals (e.g., lysosomal K^+efflux, extracellular Ca^{+2} influx, intracellular Cl^- efflux, mtROS and MAVS activity, among others) that induce PTMs on cryopyrin and release it from its inactive (heavily sumoylated) state.[137] Active cryopyrin then associates to ASC via its PYD domain and, together with NEK7,[139] oligomerises into a complex with caspase-1 in the centre. CAPS may then result from any mutations that affect this process.

A1.4 Tumour Necrosis Factor Receptor-associated Periodic Syndrome (TRAPS)

TRAPS is an autosomal dominant SAID caused by mutations in *TNFRSF1A,* gene encoding the tumour necrosis factor receptor superfamily member 1A (aka TNF-R1).[140] Expressed by nearly all cell types, TNF-R1 is a receptor for TNFSF2 (aka TNF-α) and homotrimeric TNFSF1 (aka LT-α),[141] playing an important role in T-cell-mediated antitumour responses and immune regulation.[142] Upon ligand binding, TNF-R1 trimerizes and, through its intracellular death domain, recruits the adaptor molecules Fas-associated death domain (FADD) and TNF receptor-associated death domain (TRADD). Recruitment by FADD results in the activation of caspase-8 and the initiation of a proteolytic cascade that ends in apoptosis.[143] Downstream of TRADD, TNF-R1 signalling leads to activation of NF-κB and upregulation of several inflammasome components.[143]

The *TNFRSF1A* gene is comprised of 10 exons, with exons 1 and 2 coding for the secretion sequence; exons 2-6 for the extracellular domain; exon 7 for the single-helix transmembrane segment; and exons 7-10 for the intracellular domain of TNF-R1. Interestingly, all but one of the 69 *TNFRSF1A* variants reported to INFEVERS[93] as having a role in the pathogenesis of TRAPS bear mutations on exons 2, 3, 4, and 6, particularly in two cysteine-rich domains critical for the correct folding of the protein.[144] This fact concurred with other findings to support a model in which TRAPS emerges mainly from intracellular accumulation of misfolded TNF-R1,[141] and the consequent NLRP3 inflammasome activation (hence TRAPS being considered and inflammasomopathy) due endoplasmic reticulum stress.[145] This model also includes a second, likely less prominent pathogenic mechanism in which some mutations on exon 6 close to the transmembrane segment would impede the proteolytic excision and subsequent secretion of the receptor's ectodomain, hampering its negative control function to ultimately lead to cytokine overactivity.[141]

TRAPS equally affects both sexes, with an estimated prevalence of ≈ 1:1,000,000 of the general population.[141] Although most of the reported cases are of infants (i.e., < 7 years of age),[146,147] the first symptoms may appear at any point in life. The disease phenotypes are similar to those of CAPS, with the difference that CNS involvement is rarer in TRAPS. Frequency, intensity, and duration of flares can be reduced by chronic administration of non-steroidal anti-inflammatory drugs.[148] Biological IL-1β inhibitors remain, however, the primary indication for moderate to severe cases of TRAPS.[1,6,148] Efficacy of TNF-α inhibitors has proven insufficient for TRAPS, possibly highlighting the secondary role of this cytokine in the pathophysiology of the disease.

A2. ^{15}N-labelling of proteins in *E. coli*

For the labelled medium:

Table A2.1 – ^{15}N-labelled medium

Amount	Reagent
100 mL	M9 medium (10x) (recipe below). Do not use commercial M9 as it has 14N-ammonium
5 mL	Trace elements (200x). A recipe can be found in http://www.mrc-lmb.cam.ac.uk/ms/methods/protein/nmr.html)
20 mL	20% (w/v) glucose (autoclaved separately and added under sterility)
1 mL	1 M MgSO4 sterile
1 mL	0.333 M CaCl2 sterile
1 mL	1 mg·mL^{-1} biotin sterile
1 mL	1 mg·mL^{-1} thiamin sterile
1 g	^{15}N-labelled NH_4Cl (filter sterile after dissolving)
	Appropriate antibiotics
q.s.t. 1,000 mL	Deionized water

And for a standard M9 medium (no ammonium chlorine):

Table A2.2 – M9 minimum medium

Amount	Reagent
60 g	$Na_2HPO_4 \cdot 7H_2O$
30 g	KH_2PO_4
5 g	NaCl
pH	Adjust to 7.4, then autoclave

A3. Rosetta resfile (.rf)

File containing the design constraints parsed to Rosetta (section 2.2.2). The residue numbers are relative to the template structure (PDB 1IOB).

```
#================================== Head ==================================#

# disallow any mutations
NATAA
start

#================================== Body ==================================#

# allow site-specific mutations
46 A POLAR
48 A NOTAA STNQHPYWC
51 A NOTAA EDC
52 A NOTAA STNQHPYWC
53 A NOTAA STNQHPYWC
```

56 A POLAR
93 A NOTAA RHKC
94 A NOTAA RHKC
103 A NOTAA RHKC
105 A NOTAA EDC
106 A NOTAA STNQHPYWC
107 A NOTAA STNQHPYWC

A4. Rosetta script (.xml)

File containing the instructions run by Rosetta (section 2.2.2).

```
<!-- Script to design first generation of IL-1b mutants -->

<ROSETTASCRIPTS>
  <SCOREFXNS>
    <ScoreFunction name="ref2015" weights="ref2015.wts" />
  </SCOREFXNS>
  <RESIDUE_SELECTORS>
    <!-- for rmsd calculations only -->
    <Index name="full_length_ligand" resnums="1-153" />
    <!-- for rmsd calculations only -->
    <Index name="non_designable_RBS" resnums="1,2,4,6,11,13-15,25,27,29-36,38,46,48,51,53,55,56,92-
94,103,105,108,127-129,149,150,152" />
  </RESIDUE_SELECTORS>
  <TASKOPERATIONS>
  <!--  GENERAL TASK OPERATIONS  ================================== -->
    <IncludeCurrent name="include_current"/>
    <ExtraRotamersGeneric name="extra_chi" ex1="1" ex2="1" ex1_sample_level="1" ex2_sample_level="1" />
    <LimitAromaChi2 name="limit_aro_chi2" />
    <ReadResfile name="read_resfile" filename="input_files/gp2gn1.rf" />
  </TASKOPERATIONS>
  <FILTERS>
  <!--  GENERAL FILTERS  ========================================== -->
  <!-- disabled general filters (report to scorefile) -->
    <ResidueCount name="rescount_general_disabled" max_residue_count="0" min_residue_count="0" confi-
dence="0" />
    <ExposedHydrophobics name="hydrophobics_general_disabled" threshold="0.0" confidence="0" />
    <RmsdFromResidueSelectorFilter name="rmsd_bb_all_general_disabled" CA_only="1" refer-
ence_name="native_structure" reference_selector="full_length_ligand" query_selector="full_length_ligand" thresh-
old="1.0" confidence="0" />
    <RmsdFromResidueSelectorFilter name="rmsd_bb_RBS_general_disabled" CA_only="1" refer-
ence_name="native_structure" reference_selector="non_designable_RBS" query_selector="non_designa-
ble_RBS" threshold="1.0" confidence="0" />
    <RmsdFromResidueSelectorFilter name="rmsd_sc_RBS_general_disabled" CA_only="0" refer-
ence_name="native_structure" reference_selector="non_designable_RBS" query_selector="non_designa-
ble_RBS" threshold="1.0" confidence="0" />
    <SecondaryStructure name="ss_general_disabled" compute_pose_secstruct_by_dssp="1" threshold="0.9"
confidence="0" />
    <Holes name="holes_general_disabled" residue_selector="full_length_ligand" threshold="1.0" confi-
dence="0" />
    <PackStat name="pack_stat_general_disabled" threshold="1.0" repeats="3" confidence="0" />
```

```
      <BuriedUnsatHbonds name="unsats_general_disabled" report_all_heavy_atom_unsats="1"
scorefxn="ref2015" cutoff="10" residue_surface_cutoff="20.0" ignore_surface_res="1" confidence="0" />
      <BuriedSurfaceArea name="buried_general_disabled" confidence="0" />
   <!-- enabled general filters (ensure that anything that comes from MC design will pass these minimum criteria)
-->
   <RmsdFromResidueSelectorFilter name="rmsd_bb_all_general_enabled" CA_only="1" reference_name="na-
tive_structure" reference_selector="full_length_ligand" query_selector="full_length_ligand" threshold="2.8" confi-
dence="1" />
   <RmsdFromResidueSelectorFilter name="rmsd_bb_RBS_general_enabled" CA_only="1" refer-
ence_name="native_structure" reference_selector="non_designable_RBS" query_selector="non_designa-
ble_RBS" threshold="2.5" confidence="1" />
   <RmsdFromResidueSelectorFilter name="rmsd_sc_RBS_general_enabled" CA_only="0" refer-
ence_name="native_structure" reference_selector="non_designable_RBS" query_selector="non_designa-
ble_RBS" threshold="3.0" confidence="1" />
   <PackStat name="pack_stat_general_enabled" threshold="0.62" repeats="3" confidence="1" />
   <CompoundStatement name="all_general_enabled" >
      <AND filter_name="rmsd_bb_all_general_enabled" />
      <AND filter_name="rmsd_bb_RBS_general_enabled" />
      <AND filter_name="rmsd_sc_RBS_general_enabled" />
      <AND filter_name="pack_stat_general_enabled" />
   </CompoundStatement>
   <!--  DESIGN-SPECIFIC FILTERS  ================================== -->
   <!-- enabled design filters (to be parsed to MC design) -->
      <ScoreType name="total_score_design_g2_enabled" scorefxn="ref2015" score_type="total_score" thresh-
old="-450" confidence="1" />
      <RmsdFromResidueSelectorFilter name="rmsd_bb_all_design_g2_enabled" CA_only="1" refer-
ence_name="native_structure" reference_selector="full_length_ligand" query_selector="full_length_ligand" thresh-
old="2.0" confidence="1" />
      <RmsdFromResidueSelectorFilter name="rmsd_bb_RBS_design_g2_enabled" CA_only="1" refer-
ence_name="native_structure" reference_selector="non_designable_RBS" query_selector="non_designa-
ble_RBS" threshold="1.8" confidence="1" />
      <RmsdFromResidueSelectorFilter name="rmsd_sc_RBS_design_g2_enabled" CA_only="0" refer-
ence_name="native_structure" reference_selector="non_designable_RBS" query_selector="non_designa-
ble_RBS" threshold="2.3" confidence="1" />
      <SecondaryStructure name="ss_design_g2_enabled" compute_pose_secstruct_by_dssp="1" thresh-
old="0.95" confidence="1" />
      <PackStat name="pack_stat_design_g2_enabled" threshold="0.65" repeats="3" confidence="1" />
      <Holes name="holes_design_g2_enabled" residue_selector="full_length_ligand" threshold="1.0" confi-
dence="1" />
      <BuriedUnsatHbonds name="unsats_design_g2_enabled" report_all_heavy_atom_unsats="1"
scorefxn="ref2015" cutoff="24" residue_surface_cutoff="20.0" ignore_surface_res="1" confidence="1" />
      <BuriedSurfaceArea name="buried_design_g2_enabled" cutoff_buried_surface_area="24000" confi-
dence="1" />
      <CompoundStatement name="all_design_g2_enabled" >
         <AND filter_name="total_score_design_g2_enabled" />
         <AND filter_name="rmsd_bb_all_design_g2_enabled" />
         <AND filter_name="rmsd_bb_RBS_design_g2_enabled" />
         <AND filter_name="rmsd_sc_RBS_design_g2_enabled" />
         <AND filter_name="unsats_design_g2_enabled" />
         <AND filter_name="ss_design_g2_enabled" />
         <AND filter_name="pack_stat_design_g2_enabled" />
         <AND filter_name="holes_design_g2_enabled" />
         <AND filter_name="buried_design_g2_enabled" />
      </CompoundStatement>
   </FILTERS>
   <MOVERS>
```

```
      <SavePoseMover name="save_native" reference_name="native_structure" pdb_file="input_files/1IOB.pdb"
/>
      <AtomTree name="apply_fold_tree" fold_tree_file="input_files/gp2gn1.ft" />
      <Dssp name="ss_by_dssp" />
      <FastDesign name="fast_design_g2" scorefxn="ref2015" task_operations="include_current,ex-
tra_chi,limit_aro_chi2,read_resfile" >
         <MoveMap bb="true" chi="true" jump="false" />
      </FastDesign>
      <GenericMonteCarlo name="MC_design_g2" mover_name="fast_design_g2" filter_name="all_de-
sign_g2_enabled" trials="5" preapply="0" recover_low="0" stopping_condition="all_design_g2_enabled" />
   </MOVERS>
   <PROTOCOLS>
   <!-- MOVERS ================================================== -->
      <Add mover="save_native" />
      <Add mover="apply_fold_tree" />
      <Add mover="ss_by_dssp" />
      <Add mover="MC_design_g2" />
   <!-- FILTERS ================================================== -->
   <!-- reporter filters must be parsed one by one (i.e., not in a CompoundStatement) if they are to appear individ-
ually in the output silent file -->
      <Add filter="rescount_general_disabled" />
      <Add filter="hydrophobics_general_disabled" />
      <Add filter="rmsd_bb_all_general_disabled" />
      <Add filter="rmsd_bb_RBS_general_disabled" />
      <Add filter="rmsd_sc_RBS_general_disabled" />
      <Add filter="ss_general_disabled" />
      <Add filter="holes_general_disabled" />
      <Add filter="pack_stat_general_disabled" />
      <Add filter="unsats_general_disabled" />
      <Add filter="buried_general_disabled" />
   <!-- all enabled general filters -->
      <Add filter="all_general_enabled" />
   </PROTOCOLS>
   <OUTPUT>
   </OUTPUT>
</ROSETTASCRIPTS>
```

A5. GROMACS parameters files (.mdp)

File containing the instructions run by Gromacs (section 2.2.3).

```
;------------------------------------------------------------------------------;
;                  PARAMETERS FOR ENERGY MINIMISATION                          ;
;------------------------------------------------------------------------------;

define               =
; RUN CONTROL PARAMETERS
integrator           = steep          ; steepest decent integrator
nstcomm              = 50             ; [steps] remove center of mass motion every 10 fs
comm-mode            = linear         ; remove center of mass translation
; ENERGY MINIMIZATION
emtol                = 1000           ; [kJ/mol.nm] threshold for energy conversion
emstep               = 0.01           ; [nm] step size
nsteps               = 10000          ; [steps] run up to 10,000 steps
; BOND CONSTRAINTS
```

```
; OUTPUT CONTROL OPTIONS
nstxout                 = 50            ; [steps] save coordinates at every 50 steps
nstenergy               = 50            ; [steps] save energies at every 50 steps
nstcalcenergy           = 50            ; [steps] calculate energies at every 50 steps
energygrps              = system        ; [groups] save energies for the entire system
; NEIGHBORSEARCHING PARAMETERS
cutoff-scheme           = Verlet        ; generate a pair list with buffering
nstlist                 = 10            ; [steps] update the pair list at every 10 steps
pbc                     = xyz           ; periodic boundary in all directions
verlet-buffer-tolerance = 0.005         ; [kJ/mol.ns] maximum allowed energy drift
; ELECTROSTATICS AND VDW
coulombtype             = PME           ; calculate electrostatic interactions by particle-mesh Ewald
pme-order               = 4             ; [int] interpolation order for PME
fourierspacing          = 0.10          ; [nm] grid dimensions for Fourier space
vdwtype                 = cut-off       ; use  and rvdw to calculate VdW forces
rvdw                    = 1.0           ; [nm] cut-off distance of 1.0 nm for vdW interactions
DispCorr                = no            ; do not apply dispersion correction
; TEMPERATURE COUPLING
; PRESSURE COUPLING
; SIMULATED ANNEALING
; FREE ENERGY CALCULATIONS
; VELOCITIES GENERATION


;------------------------------------------------------------------------------;
;                   PARAMETERS FOR TEMPERATURE COUPLING                        ;
;------------------------------------------------------------------------------;

define                  =
; RUN CONTROL PARAMETERS
integrator              = md            ; leap-frog integrator
dt                      = 0.002         ; [ps] integrate at every 2 fs
nsteps                  = 50000         ; [steps] integrate up to 100 ps
nstcomm                 = 50            ; [steps] remove center of mass motion at every 100 fs
comm-mode               = linear        ; remove translation motion only
; ENERGY MINIMIZATION
; OUTPUT CONTROL OPTIONS
nstxout                 = 500           ; [steps] save coordinates at every 1 ps
nstvout                 = 500           ; [steps] save velocities at every 1 ps
nstfout                 = 0             ; [steps] do not save forces
nstcalcenergy           = 50            ; [steps] calculate energies at every 100 fs
nstlog                  = 500           ; [steps] update log file at every 1 ps
nstenergy               = 500           ; [steps] save energies at every 1 ps
nstxout-compressed      = 500           ; [steps] save coordinates to compressed file at every 1 ps
energygrps              = system        ; [groups] write out energies for the entire system
compressed-x-precision  = 1000          ; [real] write out compressed trajectory file at precision 1000
compressed-x-grps       = system        ; write out compressed trajectory file for the entire system
; BOND CONSTRAINTS
continuation            = no            ; first MD run
constraints             = h-bonds       ; convert covalent H bonds into constraints
constraint-algorithm    = lincs         ; SHAKE not appropriate for domain decomposition
lincs-order             = 4             ; [int] expand constraint coupling matrix up to order 4
lincs-iter              = 1             ; [int] correct rotational lengthning at every 1 interation
lincs-warnangle         = 30            ; [int] warn is a bond rotates more than 30 degrees
; NEIGHBORSEARCHING PARAMETERS
cutoff-scheme           = verlet        ; buffered neighbour searching
nstlist                 = 10            ; [steps] update pair list every 20 fs
```

```
ns-type              = grid             ; search neighboring grid cells
pbc                  = xyz              ; periodic boundary in all directions

; ELECTROSTATICS AND VDW
coulombtype          = PME              ; method for calculating electrostatic interactions
rcoulomb             = 1.0              ; [nm] distance for the Coulomb cut-off
vdwtype              = cut-off          ; calculate VDW interactions by cut-off
rvdw                 = 1.0              ; [nm] LD cut-off of 1.0 nm
dispcorr             = enerpres         ; apply long-range dispersion corrections for both energy and pressure
fourierspacing       = 0.12             ; [nm] ratio of the box dimensions for Fourier spacing
pme-order            = 4                ; [int] PME interpolation order of 4
; TEMPERATURE COUPLING
tcoupl               = v-rescale        ; temperature coupling using velocities re-scaling
tc-grps              = protein non-protein ; couple protein and solvent to set temperature separately
tau_t                = 0.1 0.1          ; [ps] time constant for protein and solvent groups
ref_t                = 300 300          ; [K] reference temperature for coupling protein and solvent
; PRESSURE COUPLING
pcoupl               = no               ; no pressure coupling in NVT
; SIMULATED ANNEALING
; VELOCITIES GENERATION
gen-vel              = yes              ; assign velocities to particles according to random Maxwell distribution
gen-temp             = 300              ; [K] temperature for Maxwell distribution
gen-seed             = -1               ; pseudo-random seed generation



;-----------------------------------------------------------------------------;
;                    PARAMETERS FOR PRESSURE COUPLING                         ;
;-----------------------------------------------------------------------------;

define               =
; RUN CONTROL PARAMETERS
integrator           = md               ; leap-frog integrator
dt                   = 0.002            ; [ps] integrate at every 2 fs
nsteps               = 50000            ; [steps] integrate up to 100 ps
nstcomm              = 50               ; [steps] remove center of mass motion at every 100 fs
comm-mode            = linear           ; remove translation motion only
; ENERGY MINIMIZATION
; OUTPUT CONTROL OPTIONS
nstxout              = 500              ; [steps] save coordinates at every 1 ps
nstvout              = 500              ; [steps] save velocities at every 1 ps
nstfout              = 0                ; [steps] do not save forces
nstcalcenergy        = 50               ; [steps] calculate energies at every 100 fs
nstlog               = 500              ; [steps] update log file at every 1 ps
nstenergy            = 500              ; [steps] save energies at every 1 ps
nstxout-compressed   = 500              ; [steps] save coordinates to compressed file at every 1 ps
energygrps           = system           ; [groups] write out energies for the entire system
compressed-x-precision  = 1000          ; [real] write out compressed trajectory file at precision 1000
compressed-x-grps    = system           ; write out compressed trajectory file for the entire system
; BOND CONSTRAINTS
continuation         = yes              ; continue from NVT
constraints          = h-bonds          ; convert covalent H bonds into constraints
constraint-algorithm    = lincs         ; SHAKE not appropriate for domain decomposition
lincs-order          = 4                ; [int] expand constraint coupling matrix up to order 4
lincs-iter           = 1                ; [int] correct rotational lengthning at every 1 interation
lincs-warnangle      = 30               ; [int] warn is a bond rotates more than 30 degrees
; NEIGHBORSEARCHING PARAMETERS
cutoff-scheme        = verlet           ; buffered neighbour searching
```

```
nstlist             = 10              ; [steps] update pair list every 20 fs
ns-type             = grid            ; search neighboring grid cells
pbc                 = xyz             ; periodic boundary in all directions
; ELECTROSTATICS AND VDW
coulombtype         = pme             ; method for calculating electrostatic interactions
rcoulomb            = 1.0             ; [nm] distance for the Coulomb cut-off
vdwtype             = cut-off         ; calculate VDW interactions by cut-off
rvdw                = 1.0             ; [nm] LD cut-off of 1.0 nm
dispcorr            = enerpres        ; apply long-range dispersion corrections for both energy and pressure
fourierspacing      = 0.12            ; [nm] ratio of the box dimensions for Fourier spacing
pme-order           = 4               ; [int] PME interpolation order of 4
; TEMPERATURE COUPLING
tcoupl              = v-rescale       ; temperature coupling using velocities re-scaling
tc-grps             = protein non-protein ; couple protein and solvent to set temperature separately
tau_t               = 0.1 0.1         ; [ps] time constant for protein and solvent groups
ref_t               = 300 300         ; [K] reference temperature for coupling protein and solvent
; PRESSURE COUPLING
pcoupl              = Parrinello-Rahman  ; pressure coupling in NPT
pcoupltype          = isotropic       ; uniform scaling of box vectors
tau_p               = 2.0             ; [ps] time constant, in ps
ref_p               = 1.0             ; [bar] reference pressure, in bar
compressibility     = 4.5e-5          ; [barˆ-1] isothermal compressibility of water, bar^-1
; SIMULATED ANNEALING
; VELOCITIES GENERATION
gen-vel             = no              ; read velocities from NVT trajectory file


;---------------------------------------------------------------------------;
;                    PARAMETERS FOR PRODUCTION MD                           ;
;---------------------------------------------------------------------------;

define              =
; RUN CONTROL PARAMETERS
integrator          = md              ; leap-frog integrator
dt                  = 0.002           ; [ps] integrate at every 2 fs
nsteps              = 50000000        ; [steps] integrate up to 100 ns
nstcomm             = 50              ; [steps] remove center of mass motion at every 100 fs
comm-mode           = linear          ; remove translation motion only
; ENERGY MINIMIZATION
; OUTPUT CONTROL OPTIONS
nstxout             = 5000            ; [steps] save coordinates at every 10 ps
nstvout             = 5000            ; [steps] save velocities at every 10 ps
nstfout             = 0               ; [steps] do not save forces
nstcalcenergy       = 50              ; [steps] calculate energies at every 100 fs
nstlog              = 5000            ; [steps] update log file at every 10 ps
nstenergy           = 5000            ; [steps] save energies at every 10 ps
nstxout-compressed  = 5000            ; [steps] save coordinates to compressed file at every 10 ps
energygrps          = system          ; [groups] write out energies for the entire system
compressed-x-precision  = 1000        ; [real] write out compressed trajectory file at precision 1000
compressed-x-grps   = system          ; write out compressed trajectory file for the entire system
; BOND CONSTRAINTS
continuation        = yes             ; continue from NPT
constraints         = h-bonds         ; convert covalent H bonds into constraints
constraint-algorithm    = lincs       ; SHAKE not appropriate for domain decomposition
lincs-order         = 4               ; [int] expand constraint coupling matrix up to order 4
lincs-iter          = 1               ; [int] correct rotational lengthning at every 1 interation
lincs-warnangle     = 30              ; [int] warn is a bond rotates more than 30 degrees
```

```
; NEIGHBORSEARCHING PARAMETERS
cutoff-scheme          = verlet            ; buffered neighbour searching
nstlist                = 10                ; [steps] update pair list every 20 fs
ns-type                = grid              ; search neighboring grid cells
pbc                    = xyz               ; periodic boundary in all directions
; ELECTROSTATICS AND VDW
coulombtype            = pme               ; method for calculating electrostatic interactions
rcoulomb               = 1.0               ; [nm] distance for the Coulomb cut-off
vdwtype                = cut-off           ; calculate VDW interactions by cut-off
rvdw                   = 1.0               ; [nm] LD cut-off of 1.0 nm
dispcorr               = enerpres          ; apply long-range dispersion corrections for both energy and pressure
fourierspacing         = 0.12              ; [nm] ratio of the box dimensions for Fourier spacing
pme-order              = 4                 ; [int] PME interpolation order of 4
; TEMPERATURE COUPLING
tcoupl                 = v-rescale         ; temperature coupling using velocities re-scaling
tc-grps                = protein non-protein ; couple protein and solvent to set temperature separately
tau_t                  = 0.1 0.1           ; [ps] time constant for protein and solvent groups
ref_t                  = 300 300           ; [K] reference temperature for coupling protein and solvent
; PRESSURE COUPLING
pcoupl                 = Parrinello-Rahman  ; pressure coupling in NPT
pcoupltype             = isotropic         ; uniform scaling of box vectors
tau_p                  = 2.0               ; [ps] time constant, in ps
ref_p                  = 1.0               ; [bar] reference pressure, in bar
compressibility        = 4.5e-5            ; [barˆ-1] isothermal compressibility of water, bar^-1
; SIMULATED ANNEALING
; VELOCITIES GENERATION
gen-vel                = no                ; read velocities from NPT trajectory file
```

A6. Statistics from protein-protein interaction assays

The tables below reproduce the parameters employed on the statistical analyses of the interaction kinetics discussed in section 3.3.2.

Table A6.1 – Curve fitting statistics for interaction with canakinumab Fab.

Ligand	Analyte Conc. (nM)	R (nm)	R_{max} (nm)	R_{max} error	k_{obs} (s^{-1})	k_{obs} error	R_{eq}	R_{eq}/R_{max} (%)	Full X^2	Full R^2	K_D (M)	K_D error	k_{on} ($M^{-1}\cdot s^{-1}$)	k_{on} error	k_{off} (s^{-1})	k_{off} error
IL-1β	50	1.2493	1.3059	0.0003	1.30E-02	1.13E-05	1.2615	96.6	1.6419	0.9996	1.76E-09	2.36E-12	2.52E+05	2.17E+02	4.43E-04	4.54E-07
	25	0.9694	1.1999	0.0005	6.73E-03	5.89E-06	1.121	93.4	1.6419	0.9996						
	12.5	0.6592	1.1466	0.0008	3.59E-03	3.17E-06	1.0051	87.7	1.6419	0.9996						
	6.25	0.3838	1.0909	0.0009	2.01E-03	1.81E-06	0.8513	78	1.6419	0.9996						
	3.12	0.1926	0.9924	0.0011	1.23E-03	1.13E-06	0.6345	63.9	1.6419	0.9996						
	1.6	0.0967	0.9137	0.0016	8.45E-04	8.02E-07	0.4351	47.6	1.6419	0.9996						
IL-1b-02	50	1.1706	1.2625	0.0005	1.07E-02	1.26E-05	1.2092	95.8	2.1779	0.9993	2.20E-09	3.87E-12	2.05E+05	2.40E+02	4.51E-04	5.90E-07
	25	0.8523	1.1436	0.0008	5.57E-03	6.60E-06	1.051	91.9	2.1779	0.9993						
	12.5	0.5453	1.0821	0.0011	3.01E-03	3.59E-06	0.92	85	2.1779	0.9993						
	6.25	0.3057	1.0281	0.0013	1.73E-03	2.09E-06	0.7602	73.9	2.1779	0.9993						
	3.12	0.1559	0.9569	0.0015	1.09E-03	1.34E-06	0.5609	58.6	2.1779	0.9993						
	1.6	0.0712	0.8154	0.0022	7.79E-04	9.74E-07	0.3431	42.1	2.1779	0.9993						
IL-1b-03	50	1.0482	1.0899	0.0003	1.58E-02	1.88E-05	1.0442	95.8	2.3176	0.9991	2.19E-09	3.46E-12	3.03E+05	3.62E+02	6.64E-04	6.85E-07
	25	0.8076	0.9563	0.0005	8.24E-03	9.74E-06	0.8792	91.9	2.3176	0.9991						
	12.5	0.5452	0.8678	0.0008	4.45E-03	5.21E-06	0.7383	85.1	2.3176	0.9991						
	6.25	0.3091	0.7788	0.0009	2.56E-03	2.95E-06	0.5766	74	2.3176	0.9991						
	3.12	0.1596	0.7046	0.0012	1.61E-03	1.82E-06	0.4139	58.7	2.3176	0.9991						
	1.6	0.0653	0.5475	0.0016	1.15E-03	1.26E-06	0.231	42.2	2.3176	0.9991						
IL-1b-04	50	1.0452	1.1045	0.0004	1.31E-02	1.50E-05	1.0525	95.3	1.8908	0.9992	2.47E-09	3.84E-12	2.49E+05	2.87E+02	6.15E-04	6.38E-07
	25	0.7697	0.9688	0.0006	6.84E-03	7.82E-06	0.8816	91	1.8908	0.9992						
	12.5	0.4956	0.8878	0.0008	3.73E-03	4.23E-06	0.7412	83.5	1.8908	0.9992						
	6.25	0.2758	0.8106	0.001	2.17E-03	2.43E-06	0.5808	71.7	1.8908	0.9992						
	3.12	0.1313	0.706	0.0012	1.39E-03	1.53E-06	0.3939	55.8	1.8908	0.9992						
	1.6	0.0489	0.5251	0.0017	1.01E-03	1.10E-06	0.2063	39.3	1.8908	0.9992						
IL-1b-05	50	0.9918	1.0312	0.0003	1.63E-02	1.56E-05	0.9874	95.8	1.3631	0.9994	2.22E-09	2.79E-12	3.12E+05	3.00E+02	6.92E-04	5.59E-07
	25	0.7707	0.9079	0.0004	8.49E-03	8.07E-06	0.8339	91.9	1.3631	0.9994						
	12.5	0.5159	0.8111	0.0006	4.59E-03	4.31E-06	0.689	84.9	1.3631	0.9994						
	6.25	0.2853	0.7048	0.0007	2.64E-03	2.44E-06	0.5203	73.8	1.3631	0.9994						
	3.12	0.1351	0.5882	0.0008	1.67E-03	1.50E-06	0.3439	58.5	1.3631	0.9994						
	1.6	0.0464	0.4	0.0012	1.19E-03	1.04E-06	0.1677	41.9	1.3631	0.9994						

Table A7.1 – continuation.

Ligand	Analyte Conc. (nM)	R (nm)	R_{max} (nm)	R_{max} error	k_{obs} (s^{-1})	k_{obs} error	R_{eq}	R_{eq}/R_{max} (%)	Full X^2	Full R^2	K_D (M)	K_D error	k_{on} ($M^{-1}\cdot s^{-1}$)	k_{on} error	k_{off} (s^{-1})	k_{off} error
IL-1b-06	50	1.0062	1.0444	0.0003	1.52E-02	1.60E-05	1.0072	96.4	1.6368	0.9993	1.85E-09	2.80E-12	2.93E+05	3.08E+02	5.41E-04	5.92E-07
	25	0.7654	0.8975	0.0004	7.86E-03	8.28E-06	0.8357	93.1	1.6368	0.9993						
	12.5	0.4925	0.7833	0.0006	4.20E-03	4.44E-06	0.6824	87.1	1.6368	0.9993						
	6.25	0.2725	0.6801	0.0007	2.37E-03	2.51E-06	0.5249	77.2	1.6368	0.9993						
	3.12	0.1325	0.5817	0.0009	1.46E-03	1.55E-06	0.3653	62.8	1.6368	0.9993						
	1.6	0.038	0.3088	0.0013	1.01E-03	1.08E-06	0.1433	46.4	1.6368	0.9993						
IL-1b-07	50	0.9925	1.0572	0.0005	1.26E-02	1.84E-05	1.0107	95.6	2.6907	0.9988	2.30E-09	4.72E-12	2.40E+05	3.51E+02	5.52E-04	7.98E-07
	25	0.7098	0.9013	0.0007	6.56E-03	9.57E-06	0.8254	91.6	2.6907	0.9988						
	12.5	0.4568	0.8176	0.001	3.55E-03	5.19E-06	0.6906	84.5	2.6907	0.9988						
	6.25	0.2516	0.7387	0.0011	2.05E-03	2.99E-06	0.5401	73.1	2.6907	0.9988						
	3.12	0.1196	0.6327	0.0014	1.30E-03	1.89E-06	0.3643	57.6	2.6907	0.9988						
	1.6	0.0381	0.3499	0.002	9.36E-04	1.36E-06	0.1436	41	2.6907	0.9988						
IL-1b-08	50	1.0376	1.0995	0.0003	1.50E-02	1.35E-05	1.0476	95.3	1.2724	0.9995	2.48E-09	2.91E-12	2.85E+05	2.59E+02	7.06E-04	5.26E-07
	25	0.7902	0.9578	0.0004	7.83E-03	7.01E-06	0.8715	91	1.2724	0.9995						
	12.5	0.5099	0.8493	0.0006	4.27E-03	3.77E-06	0.7088	83.5	1.2724	0.9995						
	6.25	0.281	0.7462	0.0007	2.49E-03	2.15E-06	0.5344	71.6	1.2724	0.9995						
	3.12	0.1336	0.6212	0.0008	1.60E-03	1.34E-06	0.3463	55.7	1.2724	0.9995						
	1.6	0.0422	0.3507	0.0012	1.16E-03	9.41E-07	0.1376	39.2	1.2724	0.9995						
IL-1b-09	50	0.9358	0.9797	0.0003	1.70E-02	1.68E-05	0.9363	95.6	1.3071	0.9994	2.32E-09	2.94E-12	3.24E+05	3.23E+02	7.52E-04	5.91E-07
	25	0.7221	0.8445	0.0004	8.86E-03	8.67E-06	0.7728	91.5	1.3071	0.9994						
	12.5	0.4729	0.733	0.0005	4.81E-03	4.63E-06	0.6183	84.4	1.3071	0.9994						
	6.25	0.2624	0.6321	0.0006	2.78E-03	2.61E-06	0.4611	73	1.3071	0.9994						
	3.12	0.1258	0.5302	0.0008	1.76E-03	1.60E-06	0.3042	57.4	1.3071	0.9994						
	1.6	0.038	0.2901	0.0011	1.27E-03	1.11E-06	0.1185	40.8	1.3071	0.9994						
IL-1b-10	50	0.9746	1.0287	0.0003	1.39E-02	1.50E-05	0.9854	95.8	1.5395	0.9993	2.19E-09	3.30E-12	2.66E+05	2.89E+02	5.84E-04	6.08E-07
	25	0.7231	0.8839	0.0005	7.24E-03	7.82E-06	0.8126	91.9	1.5395	0.9993						
	12.5	0.4608	0.7813	0.0007	3.91E-03	4.22E-06	0.6646	85.1	1.5395	0.9993						
	6.25	0.2521	0.6859	0.0008	2.25E-03	2.41E-06	0.5077	74	1.5395	0.9993						
	3.12	0.123	0.594	0.001	1.42E-03	1.51E-06	0.3488	58.7	1.5395	0.9993						
	1.6	0.0375	0.3213	0.0014	1.01E-03	1.07E-06	0.1355	42.2	1.5395	0.9993						

Table A7.1 – continuation.

Ligand	Analyte Conc. (nM)	R (nm)	R_{max} (nm)	R_{max} error	k_{obs} (s^{-1})	k_{obs} error	R_{eq}	R_{eq}/R_{max} (%)	Full X^2	Full R^2	K_D (M)	K_D error	k_{on} ($M^{-1}\cdot s^{-1}$)	k_{on} error	k_{off} (s^{-1})	k_{off} error
IL-1b-11	50	1.0226	1.0744	0.0002	1.55E-02	1.32E-05	1.0289	95.8	1.1773	0.9995	2.21E-09	2.50E-12	2.97E+05	2.55E+02	6.57E-04	4.84E-07
	25	0.8233	0.9833	0.0004	8.08E-03	6.85E-06	0.9035	91.9	1.1773	0.9995						
	12.5	0.5546	0.8906	0.0006	4.37E-03	3.67E-06	0.7568	85	1.1773	0.9995						
	6.25	0.3325	0.8556	0.0007	2.51E-03	2.08E-06	0.632	73.9	1.1773	0.9995						
	3.12	0.1743	0.8006	0.0009	1.58E-03	1.28E-06	0.4686	58.5	1.1773	0.9995						
	1.6	0.0923	0.7746	0.0013	1.13E-03	8.92E-07	0.3252	42	1.1773	0.9995						
IL-1b-12	50	1.0298	1.0781	0.0002	1.49E-02	1.22E-05	1.0325	95.8	1.0622	0.9996	2.21E-09	2.43E-12	2.85E+05	2.34E+02	6.29E-04	4.61E-07
	25	0.8199	0.9877	0.0004	7.75E-03	6.32E-06	0.9075	91.9	1.0622	0.9996						
	12.5	0.5391	0.8873	0.0005	4.19E-03	3.39E-06	0.754	85	1.0622	0.9996						
	6.25	0.3244	0.8511	0.0007	2.41E-03	1.93E-06	0.6289	73.9	1.0622	0.9996						
	3.12	0.1689	0.7963	0.0009	1.52E-03	1.19E-06	0.4662	58.5	1.0622	0.9996						
	1.6	0.0808	0.7211	0.0012	1.09E-03	8.36E-07	0.3029	42	1.0622	0.9996						
IL-1b-13	50	0.9218	0.9672	0.0002	1.83E-02	1.61E-05	0.9234	95.5	1.0893	0.9994	2.37E-09	2.60E-12	3.50E+05	3.11E+02	8.30E-04	5.30E-07
	25	0.7641	0.8837	0.0003	9.57E-03	8.30E-06	0.8071	91.3	1.0893	0.9994						
	12.5	0.5252	0.7895	0.0005	5.20E-03	4.41E-06	0.6635	84	1.0893	0.9994						
	6.25	0.3118	0.7231	0.0006	3.02E-03	2.47E-06	0.5241	72.5	1.0893	0.9994						
	3.12	0.1549	0.6346	0.0007	1.92E-03	1.50E-06	0.3604	56.8	1.0893	0.9994						
	1.6	0.07	0.5225	0.001	1.39E-03	1.03E-06	0.2104	40.3	1.0893	0.9994						
IL-1b-14	50	0.9264	0.9661	0.0002	1.73E-02	1.32E-05	0.9247	95.7	0.8116	0.9996	2.24E-09	2.20E-12	3.30E+05	2.55E+02	7.39E-04	4.51E-07
	25	0.7558	0.8807	0.0003	9.00E-03	6.83E-06	0.8084	91.8	0.8116	0.9996						
	12.5	0.512	0.7858	0.0004	4.87E-03	3.64E-06	0.6665	84.8	0.8116	0.9996						
	6.25	0.3024	0.7213	0.0005	2.80E-03	2.05E-06	0.5312	73.6	0.8116	0.9996						
	3.12	0.143	0.5975	0.0006	1.77E-03	1.25E-06	0.348	58.2	0.8116	0.9996						
	1.6	0.0592	0.448	0.0009	1.27E-03	8.60E-07	0.1868	41.7	0.8116	0.9996						
IL-1b-15	50	0.8387	0.8775	0.0002	1.91E-02	1.74E-05	0.84	95.7	0.9855	0.9994	2.24E-09	2.55E-12	3.66E+05	3.37E+02	8.19E-04	5.51E-07
	25	0.7	0.7977	0.0003	9.98E-03	8.97E-06	0.7322	91.8	0.9855	0.9994						
	12.5	0.4813	0.7062	0.0004	5.40E-03	4.76E-06	0.599	84.8	0.9855	0.9994						
	6.25	0.2791	0.6234	0.0005	3.11E-03	2.66E-06	0.4591	73.6	0.9855	0.9994						
	3.12	0.1301	0.5013	0.0006	1.96E-03	1.60E-06	0.292	58.2	0.9855	0.9994						
	1.6	0.0457	0.3369	0.0009	1.41E-03	1.09E-06	0.1405	41.7	0.9855	0.9994						

Table A6.2 – Curve fitting statistics for interaction with gevokizumab Fab.

Ligand	Analyte Conc. (nM)	R (nm)	R_{max} (nm)	R_{max} error	k_{obs} (s^{-1})	k_{obs} error	R_{eq}	R_{eq}/R_{max} (%)	Full X^2	Full R^2	K_D (M)	K_D error	k_{on} ($M^{-1}\cdot s^{-1}$)	k_{on} error	k_{off} (s^{-1})	k_{off} error
IL-1β	50	1.0675	1.4437	0.0019	9.82E-03	2.13E-05	1.0913	75.6	4.2305	0.9974	1.61E-08	4.41E-11	1.49E+05	3.92E+02	2.40E-03	1.69E-06
	25	0.7349	1.432	0.0028	6.11E-03	1.15E-05	0.8702	60.8	4.2305	0.9974						
	12.5	0.4387	1.4298	0.0034	4.25E-03	6.59E-06	0.624	43.6	4.2305	0.9974						
	6.25	0.2496	1.5066	0.0042	3.33E-03	4.14E-06	0.4205	27.9	4.2305	0.9974						
	3.12	0.1269	1.5155	0.0053	2.86E-03	2.91E-06	0.2455	16.2	4.2305	0.9974						
	1.6	0.071	1.6278	0.0078	2.64E-03	2.31E-06	0.1468	9	4.2305	0.9974						
IL-1b-02	50	1.0866	1.4063	0.0012	6.70E-03	1.02E-05	1.2333	87.7	1.6158	0.9993	7.01E-09	1.27E-11	1.18E+05	1.90E+02	8.24E-04	6.56E-07
	25	0.7085	1.3545	0.0016	3.76E-03	5.41E-06	1.0578	78.1	1.6158	0.9993						
	12.5	0.4132	1.349	0.002	2.29E-03	3.03E-06	0.8642	64.1	1.6158	0.9993						
	6.25	0.2357	1.4071	0.0024	1.56E-03	1.85E-06	0.6631	47.1	1.6158	0.9993						
	3.12	0.1219	1.4208	0.0029	1.19E-03	1.25E-06	0.4375	30.8	1.6158	0.9993						
	1.6	0.0673	1.4929	0.0041	1.01E-03	9.61E-07	0.2773	18.6	1.6158	0.9993						
IL-1b-03	50	1.0289	1.3212	0.0007	6.38E-03	6.79E-06	1.1962	90.5	0.6851	0.9997	5.22E-09	6.83E-12	1.16E+05	1.27E+02	6.04E-04	4.26E-07
	25	0.6586	1.2414	0.001	3.49E-03	3.61E-06	1.0269	82.7	0.6851	0.9997						
	12.5	0.3832	1.2075	0.0012	2.05E-03	2.02E-06	0.8516	70.5	0.6851	0.9997						
	6.25	0.2107	1.2218	0.0014	1.33E-03	1.22E-06	0.6656	54.5	0.6851	0.9997						
	3.12	0.1122	1.2625	0.0018	9.65E-04	8.23E-07	0.4721	37.4	0.6851	0.9997						
	1.6	0.0608	1.3055	0.0025	7.89E-04	6.30E-07	0.3061	23.4	0.6851	0.9997						
IL-1b-04	50	1.0298	1.2215	0.001	7.82E-03	1.42E-05	1.1087	90.8	2.5898	0.9987	5.09E-09	1.13E-11	1.42E+05	2.67E+02	7.22E-04	8.37E-07
	25	0.6903	1.1619	0.0015	4.27E-03	7.52E-06	0.9654	83.1	2.5898	0.9987						
	12.5	0.4175	1.1666	0.002	2.50E-03	4.18E-06	0.8292	71.1	2.5898	0.9987						
	6.25	0.2341	1.1776	0.0023	1.61E-03	2.51E-06	0.6493	55.1	2.5898	0.9987						
	3.12	0.119	1.1781	0.0029	1.17E-03	1.67E-06	0.4479	38	2.5898	0.9987						
	1.6	0.0588	1.1321	0.004	9.49E-04	1.27E-06	0.2709	23.9	2.5898	0.9987						
IL-1b-05	50	0.7007	0.993	0.0011	6.74E-03	1.12E-05	0.7963	80.2	0.7477	0.9991	1.24E-08	2.50E-11	1.08E+05	2.08E+02	1.33E-03	8.36E-07
	25	0.4175	0.9076	0.0014	4.03E-03	6.03E-06	0.6075	66.9	0.7477	0.9991						
	12.5	0.238	0.8915	0.0016	2.68E-03	3.43E-06	0.4484	50.3	0.7477	0.9991						
	6.25	0.1194	0.8648	0.0018	2.01E-03	2.13E-06	0.2906	33.6	0.7477	0.9991						
	3.12	0.0646	0.9078	0.0023	1.67E-03	1.48E-06	0.1831	20.2	0.7477	0.9991						
	1.6	0.0294	0.8642	0.0033	1.51E-03	1.17E-06	0.0991	11.5	0.7477	0.9991						

Table A7.2 – continuation.

Ligand	Analyte Conc. (nM)	R (nm)	R_{max} (nm)	R_{max} error	k_{obs} (s^{-1})	k_{obs} error	R_{eq}	R_{eq}/R_{max} (%)	Full X^2	Full R^2	K_D (M)	K_D error	k_{on} ($M^{-1}\cdot s^{-1}$)	k_{on} error	k_{off} (s^{-1})	k_{off} error
IL-1b-06	50	1.1093	1.4123	0.0009	6.50E-03	8.08E-06	1.2693	89.9	1.1002	0.9996	5.63E-09	8.49E-12	1.17E+05	1.51E+02	6.59E-04	5.07E-07
	25	0.737	1.3738	0.0013	3.58E-03	4.29E-06	1.1212	81.6	1.1002	0.9996						
	12.5	0.4152	1.3114	0.0016	2.12E-03	2.40E-06	0.904	68.9	1.1002	0.9996						
	6.25	0.2388	1.4009	0.0019	1.39E-03	1.45E-06	0.7368	52.6	1.1002	0.9996						
	3.12	0.1214	1.3735	0.0023	1.02E-03	9.79E-07	0.4896	35.6	1.1002	0.9996						
	1.6	0.0617	1.3708	0.0031	8.46E-04	7.49E-07	0.3032	22.1	1.1002	0.9996						
IL-1b-07	50	1.0462	1.2076	0.001	8.29E-03	1.57E-05	1.0971	90.8	3.0668	0.9985	5.04E-09	1.16E-11	1.51E+05	2.96E+02	7.59E-04	9.03E-07
	25	0.7273	1.1745	0.0016	4.53E-03	8.29E-06	0.9775	83.2	3.0668	0.9985						
	12.5	0.4302	1.1416	0.002	2.64E-03	4.60E-06	0.8137	71.3	3.0668	0.9985						
	6.25	0.2439	1.1759	0.0024	1.70E-03	2.75E-06	0.6511	55.4	3.0668	0.9985						
	3.12	0.1305	1.1877	0.003	1.23E-03	1.82E-06	0.4543	38.2	3.0668	0.9985						
	1.6	0.064	1.1339	0.0041	1.00E-03	1.38E-06	0.2734	24.1	3.0668	0.9985						
IL-1b-08	50	0.6597	0.9261	0.0011	7.85E-03	1.39E-05	0.7067	76.3	0.8404	0.9987	1.55E-08	3.43E-11	1.20E+05	2.55E+02	1.86E-03	1.11E-06
	25	0.4049	0.8547	0.0014	4.86E-03	7.49E-06	0.5274	61.7	0.8404	0.9987						
	12.5	0.2272	0.8132	0.0016	3.36E-03	4.30E-06	0.3628	44.6	0.8404	0.9987						
	6.25	0.1256	0.8534	0.002	2.61E-03	2.70E-06	0.2451	28.7	0.8404	0.9987						
	3.12	0.0654	0.8469	0.0025	2.23E-03	1.90E-06	0.1418	16.7	0.8404	0.9987						
	1.6	0.0334	0.8693	0.0036	2.05E-03	1.51E-06	0.0813	9.3	0.8404	0.9987						
IL-1b-09	50	0.6266	0.8532	0.0009	7.18E-03	1.25E-05	0.6908	81	0.7038	0.9989	1.18E-08	2.48E-11	1.16E+05	2.32E+02	1.37E-03	9.18E-07
	25	0.3857	0.7827	0.0012	4.27E-03	6.73E-06	0.5324	68	0.7038	0.9989						
	12.5	0.214	0.7348	0.0014	2.82E-03	3.82E-06	0.3787	51.5	0.7038	0.9989						
	6.25	0.1207	0.7945	0.0017	2.09E-03	2.37E-06	0.2758	34.7	0.7038	0.9989						
	3.12	0.0597	0.7621	0.0021	1.73E-03	1.64E-06	0.1599	21	0.7038	0.9989						
	1.6	0.035	0.8325	0.0031	1.55E-03	1.29E-06	0.0997	12	0.7038	0.9989						
IL-1b-10	50	0.8786	1.0289	0.0008	8.39E-03	1.43E-05	0.9234	89.7	1.7479	0.9988	5.71E-09	1.16E-11	1.51E+05	2.68E+02	8.60E-04	8.44E-07
	25	0.5985	0.9794	0.0012	4.63E-03	7.55E-06	0.7972	81.4	1.7479	0.9988						
	12.5	0.3464	0.9333	0.0015	2.74E-03	4.20E-06	0.6406	68.6	1.7479	0.9988						
	6.25	0.196	0.9554	0.0018	1.80E-03	2.52E-06	0.4992	52.3	1.7479	0.9988						
	3.12	0.1007	0.9315	0.0022	1.33E-03	1.68E-06	0.3291	35.3	1.7479	0.9988						
	1.6	0.046	0.8778	0.0031	1.10E-03	1.27E-06	0.1921	21.9	1.7479	0.9988						

Table A7.2 – continuation.

Ligand	Analyte Conc. (nM)	R (nm)	R_{max} (nm)	R_{max} error	k_{obs} (s^{-1})	k_{obs} error	R_{eq}	R_{eq}/R_{max} (%)	Full X^2	Full R^2	K_D (M)	K_D error	k_{on} ($M^{-1}\cdot s^{-1}$)	k_{on} error	k_{off} (s^{-1})	k_{off} error
IL-1b-11	50	1.1129	1.3836	0.0007	7.82E-03	8.20E-06	1.2154	87.8	1.0137	0.9995	6.92E-09	8.59E-12	1.37E+05	1.54E+02	9.51E-04	5.09E-07
	25	0.7702	1.3494	0.0011	4.39E-03	4.36E-06	1.0569	78.3	1.0137	0.9995						
	12.5	0.4584	1.319	0.0013	2.67E-03	2.43E-06	0.849	64.4	1.0137	0.9995						
	6.25	0.2758	1.4441	0.0017	1.81E-03	1.47E-06	0.6854	47.5	1.0137	0.9995						
	3.12	0.1456	1.4338	0.002	1.38E-03	9.89E-07	0.4456	31.1	1.0137	0.9995						
	1.6	0.0824	1.5787	0.0029	1.17E-03	7.55E-07	0.2965	18.8	1.0137	0.9995						
IL-1b-12	50	0.8048	1.0666	0.001	8.70E-03	1.37E-05	0.8508	79.8	1.2176	0.9987	1.27E-08	2.44E-11	1.39E+05	2.55E+02	1.76E-03	9.93E-07
	25	0.5444	1.0365	0.0014	5.23E-03	7.36E-06	0.6876	66.3	1.2176	0.9987						
	12.5	0.3225	1.0311	0.0017	3.50E-03	4.18E-06	0.5118	49.6	1.2176	0.9987						
	6.25	0.1943	1.1568	0.0022	2.63E-03	2.59E-06	0.3819	33	1.2176	0.9987						
	3.12	0.0981	1.0885	0.0026	2.19E-03	1.79E-06	0.2149	19.7	1.2176	0.9987						
	1.6	0.0623	1.3202	0.004	1.98E-03	1.40E-06	0.1479	11.2	1.2176	0.9987						
IL-1b-13	50	0.8269	1.0411	0.0007	8.92E-03	1.21E-05	0.8731	83.9	1.0168	0.9991	9.63E-09	1.54E-11	1.50E+05	2.25E+02	1.44E-03	7.96E-07
	25	0.5653	0.9926	0.0011	5.18E-03	6.42E-06	0.7166	72.2	1.0168	0.9991						
	12.5	0.337	0.9716	0.0013	3.31E-03	3.61E-06	0.5489	56.5	1.0168	0.9991						
	6.25	0.2008	1.0592	0.0017	2.38E-03	2.20E-06	0.417	39.4	1.0168	0.9991						
	3.12	0.1042	1.0417	0.0021	1.91E-03	1.50E-06	0.255	24.5	1.0168	0.9991						
	1.6	0.0573	1.125	0.003	1.68E-03	1.16E-06	0.1603	14.3	1.0168	0.9991						
IL-1b-14	50	0.9088	1.0602	0.0006	1.01E-02	1.40E-05	0.9323	87.9	1.5219	0.9989	6.86E-09	1.11E-11	1.78E+05	2.63E+02	1.22E-03	8.07E-07
	25	0.6529	1.0138	0.001	5.67E-03	7.38E-06	0.7956	78.5	1.5219	0.9989						
	12.5	0.3971	0.9837	0.0013	3.45E-03	4.09E-06	0.6352	64.6	1.5219	0.9989						
	6.25	0.2434	1.0722	0.0016	2.33E-03	2.45E-06	0.5112	47.7	1.5219	0.9989						
	3.12	0.1267	1.0613	0.002	1.78E-03	1.63E-06	0.3319	31.3	1.5219	0.9989						
	1.6	0.0717	1.1645	0.003	1.51E-03	1.23E-06	0.2203	18.9	1.5219	0.9989						
IL-1b-15	50	0.8038	0.9833	0.0007	8.98E-03	1.26E-05	0.8459	86	1.0561	0.999	8.13E-09	1.34E-11	1.55E+05	2.36E+02	1.26E-03	7.96E-07
	25	0.5458	0.9208	0.001	5.12E-03	6.69E-06	0.695	75.5	1.0561	0.999						
	12.5	0.3239	0.8798	0.0012	3.19E-03	3.74E-06	0.5332	60.6	1.0561	0.999						
	6.25	0.1907	0.938	0.0015	2.22E-03	2.27E-06	0.4078	43.5	1.0561	0.999						
	3.12	0.1021	0.9677	0.0019	1.74E-03	1.53E-06	0.2685	27.7	1.0561	0.999						
	1.6	0.0583	1.0246	0.0028	1.50E-03	1.17E-06	0.1686	16.5	1.0561	0.999						

Table A6.3 – Curve fitting statistics for interaction with IL-1R2.

Ligand	Analyte Conc. (nM)	R (nm)	R_{max} (nm)	R_{max} error	k_{obs} (s^{-1})	k_{obs} error	R_{eq}	R_{eq}/R_{max} (%)	Full X^2	Full R^2	K_D (M)	K_D error	k_{on} ($M^{-1}\cdot s^{-1}$)	k_{on} error	k_{off} (s^{-1})	k_{off} error
IL-1β	100	0.5475	0.5851	0.0002	4.95E-03	4.83E-06	0.5851	100	1.0027	0.9988	<1.0E-12	<1.0E-12	4.95E+04	4.78E+01	<1.0E-07	<1.0E-07
	50	0.4562	0.6059	0.0003	2.47E-03	2.43E-06	0.6059	100	1.0027	0.9988						
	25	0.3311	0.6573	0.0005	1.24E-03	1.24E-06	0.6572	100	1.0027	0.9988						
	12.5	0.2176	0.7352	0.0007	6.19E-04	6.41E-07	0.7352	100	1.0027	0.9988						
	6.25	0.1183	0.7438	0.0009	3.09E-04	3.42E-07	0.7437	100	1.0027	0.9988						
IL-1b-02	100	0.6537	0.6581	0.0002	8.45E-03	1.18E-05	0.6581	100	4.5102	0.996	<1.0E-12	<1.0E-12	8.45E+04	1.18E+02	<1.0E-07	<1.0E-07
	50	0.592	0.6572	0.0003	4.22E-03	5.94E-06	0.6572	100	4.5102	0.996						
	25	0.4815	0.6925	0.0006	2.11E-03	3.01E-06	0.6925	100	4.5102	0.996						
	12.5	0.3494	0.7675	0.0009	1.06E-03	1.54E-06	0.7675	100	4.5102	0.996						
	6.25	0.2158	0.8178	0.0012	5.28E-04	8.03E-07	0.8178	100	4.5102	0.996						
IL-1b-03	100	0.53	0.5495	0.0002	5.76E-03	6.13E-06	0.548	99.7	0.74	0.9991	2.78E-10	8.84E-12	5.75E+04	5.63E+01	1.60E-05	5.08E-07
	50	0.4411	0.5444	0.0003	2.89E-03	3.32E-06	0.5414	99.4	0.74	0.9991						
	25	0.3226	0.5761	0.0005	1.45E-03	1.91E-06	0.5697	98.9	0.74	0.9991						
	12.5	0.2051	0.5949	0.0006	7.34E-04	1.21E-06	0.5819	97.8	0.74	0.9991						
	6.25	0.1207	0.629	0.0008	3.75E-04	8.59E-07	0.6022	95.7	0.74	0.9991						
IL-1b-04	100	0.4802	0.5121	0.0002	4.56E-03	4.45E-06	0.5108	99.7	0.3681	0.9994	2.57E-10	9.42E-12	4.55E+04	4.03E+01	1.17E-05	4.28E-07
	50	0.36	0.4906	0.0003	2.29E-03	2.44E-06	0.4881	99.5	0.3681	0.9994						
	25	0.2536	0.5266	0.0004	1.15E-03	1.44E-06	0.5213	99	0.3681	0.9994						
	12.5	0.1545	0.5601	0.0005	5.80E-04	9.31E-07	0.5488	98	0.3681	0.9994						
	6.25	0.0843	0.5445	0.0006	2.96E-04	6.80E-07	0.523	96	0.3681	0.9994						
IL-1b-05	100	0.4728	0.5077	0.0001	4.50E-03	3.16E-06	0.5047	99.4	0.1799	0.9997	5.91E-10	6.90E-12	4.47E+04	2.85E+01	2.64E-05	3.08E-07
	50	0.3593	0.4916	0.0002	2.26E-03	1.73E-06	0.4859	98.8	0.1799	0.9997						
	25	0.2431	0.5099	0.0003	1.14E-03	1.02E-06	0.4981	97.7	0.1799	0.9997						
	12.5	0.1479	0.5284	0.0004	5.85E-04	6.64E-07	0.5045	95.5	0.1799	0.9997						
	6.25	0.0794	0.5219	0.0004	3.06E-04	4.86E-07	0.4768	91.4	0.1799	0.9997						
IL-1b-06	100	0.5688	0.565	0.0001	7.69E-03	7.18E-06	0.565	100	1.3355	0.9984	<1.0E-12	<1.0E-12	7.69E+04	7.12E+01	<1.0E-07	<1.0E-07
	50	0.4912	0.5498	0.0002	3.85E-03	3.62E-06	0.5498	100	1.3355	0.9984						
	25	0.3815	0.5691	0.0003	1.92E-03	1.84E-06	0.569	100	1.3355	0.9984						
	12.5	0.2623	0.617	0.0005	9.62E-04	9.51E-07	0.617	100	1.3355	0.9984						
	6.25	0.1599	0.6572	0.0007	4.81E-04	5.06E-07	0.6572	100	1.3355	0.9984						

Table 7.3 – continuation.

Ligand	Analyte Conc. (nM)	R (nm)	R_{max} (nm)	R_{max} error	k_{obs} (s^{-1})	k_{obs} error	R_{eq}	R_{eq}/R_{max} (%)	Full X^2	Full R^2	K_D (M)	K_D error	k_{on} ($M^{-1}\cdot s^{-1}$)	k_{on} error	k_{off} (s^{-1})	k_{off} error
	100	0.4351	0.5225	0.0002	3.13E-03	2.77E-06	0.5225	100	0.2766	0.9995						
	50	0.3125	0.5266	0.0003	1.56E-03	1.40E-06	0.5266	100	0.2766	0.9995						
IL-1b-07	25	0.1995	0.5518	0.0004	7.82E-04	7.17E-07	0.5517	100	0.2766	0.9995	1.54E-12	1.01E-12	3.13E+04	2.74E+01	<1.0E-07	<1.0E-07
	12.5	0.1139	0.5723	0.0005	3.91E-04	3.74E-07	0.5722	100	0.2766	0.9995						
	6.25	0.0571	0.5561	0.0006	1.95E-04	2.03E-07	0.556	100	0.2766	0.9995						
	100	0.514	0.5199	0.0002	6.69E-03	7.88E-06	0.5184	99.7	0.9564	0.9986						
	50	0.4217	0.4916	0.0003	3.35E-03	4.23E-06	0.4888	99.4	0.9564	0.9986						
IL-1b-08	25	0.3297	0.5331	0.0005	1.69E-03	2.41E-06	0.5271	98.9	0.9564	0.9986	2.87E-10	8.83E-12	6.67E+04	7.29E+01	1.92E-05	5.89E-07
	12.5	0.2134	0.5591	0.0006	8.53E-04	1.50E-06	0.5466	97.8	0.9564	0.9986						
	6.25	0.1229	0.5574	0.0008	4.36E-04	1.04E-06	0.533	95.6	0.9564	0.9986						
	100	0.4326	0.4536	0.0001	5.46E-03	5.11E-06	0.4452	98.2	0.3351	0.9993						
	50	0.3382	0.4349	0.0002	2.78E-03	2.78E-06	0.4192	96.4	0.3351	0.9993						
IL-1b-09	25	0.2439	0.4563	0.0003	1.44E-03	1.62E-06	0.4244	93	0.3351	0.9993	1.88E-09	8.59E-12	5.36E+04	4.66E+01	1.01E-04	4.52E-07
	12.5	0.1464	0.467	0.0004	7.71E-04	1.03E-06	0.406	86.9	0.3351	0.9993						
	6.25	0.087	0.4883	0.0005	4.36E-04	7.43E-07	0.3755	76.9	0.3351	0.9993						
	100	0.4596	0.5174	0.0003	3.79E-03	4.78E-06	0.5148	99.5	0.4423	0.9992						
	50	0.3421	0.5122	0.0004	1.91E-03	2.64E-06	0.5071	99	0.4423	0.9992						
IL-1b-10	25	0.2274	0.5389	0.0006	9.63E-04	1.57E-06	0.5281	98	0.4423	0.9992	5.08E-10	1.33E-11	3.77E+04	4.28E+01	1.92E-05	5.01E-07
	12.5	0.1418	0.5896	0.0007	4.91E-04	1.04E-06	0.5666	96.1	0.4423	0.9992						
	6.25	0.0801	0.6251	0.0009	2.55E-04	7.69E-07	0.5781	92.5	0.4423	0.9992						
	100	0.4736	0.5137	0.0002	4.30E-03	3.90E-06	0.5128	99.8	0.2917	0.9995						
	50	0.3573	0.5022	0.0003	2.15E-03	2.14E-06	0.5004	99.7	0.2917	0.9995						
IL-1b-11	25	0.2552	0.5455	0.0004	1.08E-03	1.26E-06	0.5417	99.3	0.2917	0.9995	1.75E-10	8.95E-12	4.29E+04	3.52E+01	7.49E-06	3.84E-07
	12.5	0.1497	0.5694	0.0005	5.43E-04	8.23E-07	0.5615	98.6	0.2917	0.9995						
	6.25	0.0849	0.5968	0.0006	2.75E-04	6.03E-07	0.5806	97.3	0.2917	0.9995						
	100	0.5061	0.5504	0.0002	4.38E-03	4.21E-06	0.547	99.4	0.3834	0.9995						
	50	0.3899	0.5433	0.0003	2.20E-03	2.31E-06	0.5367	98.8	0.3834	0.9995						
IL-1b-12	25	0.2676	0.5704	0.0005	1.12E-03	1.36E-06	0.5567	97.6	0.3834	0.9995	6.17E-10	9.53E-12	4.35E+04	3.80E+01	2.69E-05	4.14E-07
	12.5	0.1594	0.5897	0.0006	5.71E-04	8.89E-07	0.562	95.3	0.3834	0.9995						
	6.25	0.0892	0.6112	0.0007	2.99E-04	6.52E-07	0.5563	91	0.3834	0.9995						

Table A7.3 – continuation.

Ligand	Analyte Conc. (nM)	R (nm)	R_{max} (nm)	R_{max} error	k_{obs} (s^{-1})	k_{obs} error	R_{eq}	R_{eq}/R_{max} (%)	Full X^2	Full R^2	K_D (M)	K_D error	k_{on} ($M^{-1}\cdot s^{-1}$)	k_{on} error	k_{off} (s^{-1})	k_{off} error
	100	0.45	0.4969	0.0002	4.31E-03	3.60E-06	0.4877	98.1	0.2201	0.9996						
	50	0.3426	0.4923	0.0003	2.19E-03	1.98E-06	0.4744	96.4	0.2201	0.9996						
IL-1b-13	25	0.2283	0.502	0.0004	1.14E-03	1.17E-06	0.4668	93	0.2201	0.9996	1.89E-09	8.71E-12	4.23E+04	3.24E+01	7.98E-05	3.63E-07
	12.5	0.1365	0.5276	0.0004	6.08E-04	7.68E-07	0.4583	86.9	0.2201	0.9996						
	6.25	0.0752	0.5415	0.0005	3.44E-04	5.66E-07	0.4159	76.8	0.2201	0.9996						
	100	0.5318	0.5541	0.0002	5.45E-03	5.87E-06	0.551	99.4	0.6947	0.9991						
	50	0.4245	0.5367	0.0003	2.74E-03	3.19E-06	0.5306	98.9	0.6947	0.9991						
IL-1b-14	25	0.308	0.5654	0.0005	1.39E-03	1.85E-06	0.5528	97.8	0.6947	0.9991	5.73E-10	9.43E-12	5.42E+04	5.36E+01	3.11E-05	5.10E-07
	12.5	0.1928	0.5915	0.0006	7.08E-04	1.18E-06	0.5656	95.6	0.6947	0.9991						
	6.25	0.1074	0.6105	0.0008	3.70E-04	8.45E-07	0.5592	91.6	0.6947	0.9991						
	100	0.4239	0.4605	0.0002	4.50E-03	4.38E-06	0.4539	98.5	0.2811	0.9994						
	50	0.3251	0.4513	0.0003	2.28E-03	2.41E-06	0.4384	97.1	0.2811	0.9994						
IL-1b-15	25	0.2239	0.4756	0.0004	1.17E-03	1.42E-06	0.4491	94.4	0.2811	0.9994	1.47E-09	9.76E-12	4.44E+04	3.96E+01	6.53E-05	4.29E-07
	12.5	0.1351	0.5009	0.0005	6.20E-04	9.23E-07	0.4481	89.5	0.2811	0.9994						
	6.25	0.0742	0.5126	0.0006	3.43E-04	6.76E-07	0.4149	80.9	0.2811	0.9994						

REFERENCES

1. Georgin-Lavialle S, Fayand A, Rodrigues F, et al. Autoinflammatory diseases: State of the art. *Presse Med* 2019;48(1 Pt 2):e25-e48. doi: 10.1016/j.lpm.2018.12.003 [published Online First: 20190124]
2. Krainer J, Siebenhandl S, Weinhausel A. Systemic autoinflammatory diseases. *J Autoimmun* 2020;109:102421. doi: 10.1016/j.jaut.2020.102421 [published Online First: 20200201]
3. McGonagle D, McDermott MF. A proposed classification of the immunological diseases. *PLoS Med* 2006;3(8):e297. doi: 10.1371/journal.pmed.0030297
4. Betrains A, Staels F, Schrijvers R, et al. Systemic autoinflammatory disease in adults. *Autoimmun Rev* 2021;20(4):102774. doi: 10.1016/j.autrev.2021.102774 [published Online First: 20210217]
5. Efthimiou P, Petryna O, Nakasato P, et al. New insights on multigenic autoinflammatory diseases. *Ther Adv Musculoskelet Dis* 2022;14:1759720X221117880. doi: 10.1177/1759720X221117880 [published Online First: 20220903]
6. Georgin-Lavialle S, Ducharme-Benard S, Sarrabay G, et al. Systemic autoinflammatory diseases: Clinical state of the art. *Best Pract Res Clin Rheumatol* 2020;34(4):101529. doi: 10.1016/j.berh.2020.101529 [published Online First: 20200613]
7. Havnaer A, Han G. Autoinflammatory Disorders: A Review and Update on Pathogenesis and Treatment. *Am J Clin Dermatol* 2019;20(4):539-64. doi: 10.1007/s40257-019-00440-y
8. Soriano A, Soriano M, Espinosa G, et al. Current Therapeutic Options for the Main Monogenic Autoinflammatory Diseases and PFAPA Syndrome: Evidence-Based Approach and Proposal of a Practical Guide. *Front Immunol* 2020;11:865. doi: 10.3389/fimmu.2020.00865 [published Online First: 20200603]
9. Ross JB, Finlayson LA, Klotz PJ, et al. Use of anakinra (Kineret) in the treatment of familial cold autoinflammatory syndrome with a 16-month follow-up. *J Cutan Med Surg* 2008;12(1):8-16. doi: 10.2310/7750.2008.07050
10. Romano M, Arici ZS, Piskin D, et al. The 2021 EULAR/American College of Rheumatology points to consider for diagnosis, management and monitoring of the interleukin-1 mediated autoinflammatory diseases: cryopyrin-associated periodic syndromes, tumour necrosis factor receptor-associated periodic syndrome, mevalonate kinase deficiency, and deficiency of the interleukin-1 receptor antagonist. *Ann Rheum Dis* 2022;81(7):907-21. doi: 10.1136/annrheumdis-2021-221801 [published Online First: 20220527]
11. Kone-Paut I, Lachmann HJ, Kuemmerle-Deschner JB, et al. Sustained remission of symptoms and improved health-related quality of life in patients with cryopyrin-associated periodic syndrome treated with canakinumab: results of a double-blind placebo-controlled randomized withdrawal study. *Arthritis Res Ther* 2011;13(6):R202. doi: 10.1186/ar3535 [published Online First: 20111209]
12. Kuemmerle-Deschner JB, Gautam R, George AT, et al. Systematic literature review of efficacy/effectiveness and safety of current therapies for the treatment of cryopyrin-associated periodic syndrome, hyperimmunoglobulin D syndrome and tumour necrosis factor receptor-associated periodic syndrome. *RMD Open* 2020;6(2) doi: 10.1136/rmdopen-2020-001227
13. Nordstrom D, Knight A, Luukkainen R, et al. Beneficial effect of interleukin 1 inhibition with anakinra in adult-onset Still's disease. An open, randomized, multicenter study. *J Rheumatol* 2012;39(10):2008-11. doi: 10.3899/jrheum.111549 [published Online First: 20120801]
14. Aksentijevich I, Masters SL, Ferguson PJ, et al. An autoinflammatory disease with deficiency of the interleukin-1-receptor antagonist. *N Engl J Med* 2009;360(23):2426-37. doi: 10.1056/NEJMoa0807865
15. Ben-Zvi I, Kukuy O, Giat E, et al. Anakinra for Colchicine-Resistant Familial Mediterranean Fever: A Randomized, Double-Blind, Placebo-Controlled Trial. *Arthritis Rheumatol* 2017;69(4):854-62. doi: 10.1002/art.39995
16. Quartier P, Allantaz F, Cimaz R, et al. A multicentre, randomised, double-blind, placebo-controlled trial with the interleukin-1 receptor antagonist anakinra in patients with systemic-onset juvenile idiopathic arthritis (ANAJIS trial). *Ann Rheum Dis* 2011;70(5):747-54. doi: 10.1136/ard.2010.134254 [published Online First: 20101220]
17. Cohen S, Hurd E, Cush J, et al. Treatment of rheumatoid arthritis with anakinra, a recombinant human interleukin-1 receptor antagonist, in combination with methotrexate: results of a twenty-four-week, multicenter, randomized, double-blind, placebo-controlled trial. *Arthritis Rheum* 2002;46(3):614-24. doi: 10.1002/art.10141
18. Cohen SB, Moreland LW, Cush JJ, et al. A multicentre, double blind, randomised, placebo controlled trial of anakinra (Kineret), a recombinant interleukin 1 receptor antagonist, in patients with rheumatoid arthritis treated with background methotrexate. *Ann Rheum Dis* 2004;63(9):1062-8. doi: 10.1136/ard.2003.016014 [published Online First: 20040413]
19. Kedor C, Listing J, Zernicke J, et al. Canakinumab for Treatment of Adult-Onset Still's

Disease to Achieve Reduction of Arthritic Manifestation (CONSIDER): phase II, randomised, double-blind, placebo-controlled, multicentre, investigator-initiated trial. *Ann Rheum Dis* 2020;79(8):1090-97. doi: 10.1136/annrheumdis-2020-217155 [published Online First: 20200513]
20. Lachmann HJ, Kone-Paut I, Kuemmerle-Deschner JB, et al. Use of canakinumab in the cryopyrin-associated periodic syndrome. *N Engl J Med* 2009;360(23):2416-25. doi: 10.1056/NEJMoa0810787 [published Online First: 2009/06/06]
21. Kuemmerle-Deschner JB, Ramos E, Blank N, et al. Canakinumab (ACZ885, a fully human IgG1 anti-IL-1beta mAb) induces sustained remission in pediatric patients with cryopyrin-associated periodic syndrome (CAPS). *Arthritis Res Ther* 2011;13(1):R34. doi: 10.1186/ar3266 [published Online First: 20110228]
22. Kuemmerle-Deschner JB, Hachulla E, Cartwright R, et al. Two-year results from an open-label, multicentre, phase III study evaluating the safety and efficacy of canakinumab in patients with cryopyrin-associated periodic syndrome across different severity phenotypes. *Ann Rheum Dis* 2011;70(12):2095-102. doi: 10.1136/ard.2011.152728 [published Online First: 20110821]
23. De Benedetti F, Gattorno M, Anton J, et al. Canakinumab for the Treatment of Autoinflammatory Recurrent Fever Syndromes. *N Engl J Med* 2018;378(20):1908-19. doi: 10.1056/NEJMoa1706314 [published Online First: 2018/05/17]
24. Jeyaratnam J, Simon A, Calvo I, et al. Long-term efficacy and safety of canakinumab in patients with mevalonate kinase deficiency: results from the randomised Phase 3 CLUSTER trial. *Rheumatology (Oxford)* 2022;61(5):2088-94. doi: 10.1093/rheumatology/keab696
25. Ruperto N, Brunner HI, Quartier P, et al. Canakinumab in patients with systemic juvenile idiopathic arthritis and active systemic features: results from the 5-year long-term extension of the phase III pivotal trials. *Ann Rheum Dis* 2018;77(12):1710-19. doi: 10.1136/annrheumdis-2018-213150 [published Online First: 20180929]
26. Ruperto N, Brunner HI, Quartier P, et al. Two randomized trials of canakinumab in systemic juvenile idiopathic arthritis. *N Engl J Med* 2012;367(25):2396-406. doi: 10.1056/NEJMoa1205099 [published Online First: 2012/12/21]
27. Schlesinger N, Alten RE, Bardin T, et al. Canakinumab for acute gouty arthritis in patients with limited treatment options: results from two randomised, multicentre, active-controlled, double-blind trials and their initial extensions. *Ann Rheum Dis* 2012;71(11):1839-48. doi: 10.1136/annrheumdis-2011-200908 [published Online First: 20120514]
28. Gul A, Tugal-Tutkun I, Dinarello CA, et al. Interleukin-1beta-regulating antibody XOMA 052 (gevokizumab) in the treatment of acute exacerbations of resistant uveitis of Behcet's disease: an open-label pilot study. *Ann Rheum Dis* 2012;71(4):563-6. doi: 10.1136/annrheumdis-2011-155143 [published Online First: 20111114]
29. Tugal-Tutkun IM, Kadayifcilar SM, Khairallah MM, et al. Safety and Efficacy of Gevokizumab in Patients with Behcet's Disease Uveitis: Results of an Exploratory Phase 2 Study. *Ocul Immunol Inflamm* 2017;25(1):62-70. doi: 10.3109/09273948.2015.1092558 [published Online First: 20160130]
30. Tugal-Tutkun I, Pavesio C, De Cordoue A, et al. Use of Gevokizumab in Patients with Behcet's Disease Uveitis: An International, Randomized, Double-Masked, Placebo-Controlled Study and Open-Label Extension Study. *Ocul Immunol Inflamm* 2018;26(7):1023-33. doi: 10.1080/09273948.2017.1421233 [published Online First: 20180125]
31. Sloan-Lancaster J, Abu-Raddad E, Polzer J, et al. Double-blind, randomized study evaluating the glycemic and anti-inflammatory effects of subcutaneous LY2189102, a neutralizing IL-1beta antibody, in patients with type 2 diabetes. *Diabetes Care* 2013;36(8):2239-46. doi: 10.2337/dc12-1835 [published Online First: 20130320]
32. Cavelti-Weder C, Babians-Brunner A, Keller C, et al. Effects of gevokizumab on glycemia and inflammatory markers in type 2 diabetes. *Diabetes Care* 2012;35(8):1654-62. doi: 10.2337/dc11-2219 [published Online First: 20120614]
33. Larsen CM, Faulenbach M, Vaag A, et al. Sustained effects of interleukin-1 receptor antagonist treatment in type 2 diabetes. *Diabetes Care* 2009;32(9):1663-8. doi: 10.2337/dc09-0533 [published Online First: 20090619]
34. Spohn G, Schori C, Keller I, et al. Preclinical efficacy and safety of an anti-IL-1beta vaccine for the treatment of type 2 diabetes. *Mol Ther Methods Clin Dev* 2014;1:14048. doi: 10.1038/mtm.2014.48 [published Online First: 2014/01/01]
35. Jegerlehner A, Tissot A, Lechner F, et al. A molecular assembly system that renders antigens of choice highly repetitive for induction of protective B cell responses. *Vaccine* 2002;20(25-26):3104-12. doi: 10.1016/s0264-410x(02)00266-9
36. Bode C, Zhao G, Steinhagen F, et al. CpG DNA as a vaccine adjuvant. *Expert Rev Vaccines* 2011;10(4):499-511. doi: 10.1586/erv.10.174
37. Cavelti-Weder C, Timper K, Seelig E, et al. Development of an Interleukin-1beta Vaccine in Patients with Type 2 Diabetes. *Mol Ther* 2016;24(5):1003-12. doi: 10.1038/mt.2015.227 [published Online First: 2015/12/22]

38. Tissot AC, Maurer P, Nussberger J, et al. Effect of immunisation against angiotensin II with CYT006-AngQb on ambulatory blood pressure: a double-blind, randomised, placebo-controlled phase IIa study. *Lancet* 2008;371(9615):821-7. doi: 10.1016/S0140-6736(08)60381-5
39. Ross C, Svenson M, Nielsen H, et al. Increased in vivo antibody activity against interferon alpha, interleukin-1alpha, and interleukin-6 after high-dose Ig therapy. *Blood* 1997;90(6):2376-80.
40. Hansen MB, Svenson M, Diamant M, et al. Anti-interleukin-6 antibodies in normal human serum. *Scand J Immunol* 1991;33(6):777-81. doi: 10.1111/j.1365-3083.1991.tb02552.x
41. Meager A, Wadhwa M. Detection of anti-cytokine antibodies and their clinical relevance. *Expert Rev Clin Immunol* 2014;10(8):1029-47. doi: 10.1586/1744666X.2014.918848 [published Online First: 20140605]
42. Zha J, Chi XW, Yu XL, et al. Interleukin-1beta-Targeted Vaccine Improves Glucose Control and beta-Cell Function in a Diabetic KK-Ay Mouse Model. *PLoS One* 2016;11(5):e0154298. doi: 10.1371/journal.pone.0154298 [published Online First: 20160506]
43. Zhang Y, Yu XL, Zha J, et al. Therapeutic vaccine against IL-1beta improved glucose control in a mouse model of type 2 diabetes. *Life Sci* 2018;192:68-74. doi: 10.1016/j.lfs.2017.11.021 [published Online First: 20171116]
44. Watanabe H, Gaide O, Petrilli V, et al. Activation of the IL-1beta-processing inflammasome is involved in contact hypersensitivity. *J Invest Dermatol* 2007;127(8):1956-63. doi: 10.1038/sj.jid.5700819 [published Online First: 20070412]
45. Yeung K, Mraz V, Geisler C, et al. The role of interleukin-1beta in the immune response to contact allergens. *Contact Dermatitis* 2021;85(4):387-97. doi: 10.1111/cod.13955 [published Online First: 20210810]
46. Goksoyr L, Funch AB, Okholm AK, et al. Preclinical Efficacy of a Capsid Virus-like Particle-Based Vaccine Targeting IL-1beta for Treatment of Allergic Contact Dermatitis. *Vaccines (Basel)* 2022;10(5) doi: 10.3390/vaccines10050828 [published Online First: 20220523]
47. Thrane S, Janitzek CM, Matondo S, et al. Bacterial superglue enables easy development of efficient virus-like particle based vaccines. *J Nanobiotechnology* 2016;14:30. doi: 10.1186/s12951-016-0181-1 [published Online First: 20160427]
48. Ducreux J, Houssiau FA, Vandepapeliere P, et al. Interferon alpha kinoid induces neutralizing anti-interferon alpha antibodies that decrease the expression of interferon-induced and B cell activation associated transcripts: analysis of extended follow-up data from the interferon alpha kinoid phase I/II study. *Rheumatology (Oxford)* 2016;55(10):1901-5. doi: 10.1093/rheumatology/kew262 [published Online First: 20160628]
49. Durez P, Vandepapeliere P, Miranda P, et al. Therapeutic vaccination with TNF-Kinoid in TNF antagonist-resistant rheumatoid arthritis: a phase II randomized, controlled clinical trial. *PLoS One* 2014;9(12):e113465. doi: 10.1371/journal.pone.0113465 [published Online First: 20141217]
50. Schluter T, Schelmbauer C, Karram K, et al. Regulation of IL-1 signaling by the decoy receptor IL-1R2. *J Mol Med (Berl)* 2018;96(10):983-92. doi: 10.1007/s00109-018-1684-z [published Online First: 2018/08/16]
51. Wang D, Zhang S, Li L, et al. Structural insights into the assembly and activation of IL-1beta with its receptors. *Nat Immunol* 2010;11(10):905-11. doi: 10.1038/ni.1925 [published Online First: 2010/08/31]
52. Bachmann MF, Whitehead P. Active immunotherapy for chronic diseases. *Vaccine* 2013;31(14):1777-84. doi: 10.1016/j.vaccine.2013.02.001 [published Online First: 2013/02/19]
53. Spohn G, Keller I, Beck M, et al. Active immunization with IL-1 displayed on virus-like particles protects from autoimmune arthritis. *Eur J Immunol* 2008;38(3):877-87. doi: 10.1002/eji.200737989 [published Online First: 2008/02/07]
54. Tissot AC, Spohn G, Jennings GT, et al. A VLP-based vaccine against interleukin-1alpha protects mice from atherosclerosis. *Eur J Immunol* 2013;43(3):716-22. doi: 10.1002/eji.201242687 [published Online First: 2012/12/21]
55. Rohl CA, Strauss CE, Misura KM, et al. Protein structure prediction using Rosetta. *Methods Enzymol* 2004;383:66-93. doi: 10.1016/S0076-6879(04)83004-0
56. Li Z, Scheraga HA. Monte Carlo-minimization approach to the multiple-minima problem in protein folding. *Proceedings of the National Academy of Sciences of the United States of America* 1987;84(19):6611-5. doi: 10.1073/pnas.84.19.6611
57. Fields JK, Gunther S, Sundberg EJ. Structural Basis of IL-1 Family Cytokine Signaling. *Front Immunol* 2019;10:1412. doi: 10.3389/fimmu.2019.01412 [published Online First: 2019/07/10]
58. Spohn G, Arenas-Ramirez N, Bouchaud G, et al. Endogenous polyclonal anti-IL-1 antibody responses potentiate IL-1 activity during pathogenic inflammation. *J Allergy Clin Immunol* 2017;139(6):1957-65 e3. doi: 10.1016/j.jaci.2016.09.033 [published Online First: 2016/11/12]
59. Blech M, Peter D, Fischer P, et al. One target-two different binding modes: structural insights into gevokizumab and canakinumab interactions to interleukin-1beta. *J Mol Biol* 2013;425(1):94-111.

doi: 10.1016/j.jmb.2012.09.021 [published Online First: 2012/10/09]
60. Baker D. Centenary Award and Sir Frederick Gowland Hopkins Memorial Lecture. Protein folding, structure prediction and design. *Biochem Soc Trans* 2014;42(2):225-9. doi: 10.1042/BST20130055
61. Mandell DJ, Kortemme T. Backbone flexibility in computational protein design. *Curr Opin Biotechnol* 2009;20(4):420-8. doi: 10.1016/j.copbio.2009.07.006 [published Online First: 20090824]
62. Alford RF, Leaver-Fay A, Jeliazkov JR, et al. The Rosetta All-Atom Energy Function for Macromolecular Modeling and Design. *J Chem Theory Comput* 2017;13(6):3031-48. doi: 10.1021/acs.jctc.7b00125 [published Online First: 2017/04/22]
63. Nerli S, Sgourakis NG. Cs-Rosetta. *Methods Enzymol* 2019;614:321-62. doi: 10.1016/bs.mie.2018.07.005 [published Online First: 20180911]
64. Pronk S, Pall S, Schulz R, et al. GROMACS 4.5: a high-throughput and highly parallel open source molecular simulation toolkit. *Bioinformatics* 2013;29(7):845-54. doi: 10.1093/bioinformatics/btt055 [published Online First: 2013/02/15]
65. Lindorff-Larsen K, Piana S, Palmo K, et al. Improved side-chain torsion potentials for the Amber ff99SB protein force field. *Proteins* 2010;78(8):1950-8. doi: 10.1002/prot.22711 [published Online First: 2010/04/22]
66. Khalak Y, Baumeier B, Karttunen M. Improved general-purpose five-point model for water: TIP5P/2018. *J Chem Phys* 2018;149(22):224507. doi: 10.1063/1.5070137 [published Online First: 2018/12/17]
67. Timr S, Madern D, Sterpone F. Protein thermal stability. *Prog Mol Biol Transl Sci* 2020;170:239-72. doi: 10.1016/bs.pmbts.2019.12.007 [published Online First: 20200131]
68. Skinner SP, Fogh RH, Boucher W, et al. CcpNmr AnalysisAssign: a flexible platform for integrated NMR analysis. *J Biomol NMR* 2016;66(2):111-24. doi: 10.1007/s10858-016-0060-y [published Online First: 20160923]
69. Skinner SP, Fogh RH, Boucher W, et al. Erratum to: CcpNmr AnalysisAssign: a flexible platform for integrated NMR analysis. *J Biomol NMR* 2017;67(4):321. doi: 10.1007/s10858-017-0102-0
70. Driscoll PC, Clore GM, Marion D, et al. Complete resonance assignment for the polypeptide backbone of interleukin 1 beta using three-dimensional heteronuclear NMR spectroscopy. *Biochemistry* 1990;29(14):3542-56. doi: 10.1021/bi00466a018
71. Williamson MP. Using chemical shift perturbation to characterise ligand binding. *Prog Nucl Magn Reson Spectrosc* 2013;73:1-16. doi: 10.1016/j.pnmrs.2013.02.001 [published Online First: 20130321]
72. Kumar S, Deshpande PA. Structural and thermodynamic analysis of factors governing the stability and thermal folding/unfolding of SazCA. *PLoS One* 2021;16(4):e0249866. doi: 10.1371/journal.pone.0249866 [published Online First: 20210415]
73. Hailey KL, Li S, Andersen MD, et al. Pro-interleukin (IL)-1beta shares a core region of stability as compared with mature IL-1beta while maintaining a distinctly different configurational landscape: a comparative hydrogen/deuterium exchange mass spectrometry study. *J Biol Chem* 2009;284(38):26137-48. doi: 10.1074/jbc.M109.027375 [published Online First: 20090710]
74. Zeltins A, West J, Zabel F, et al. Incorporation of tetanus-epitope into virus-like particles achieves vaccine responses even in older recipients in models of psoriasis, Alzheimer's and cat allergy. *NPJ Vaccines* 2017;2:30. doi: 10.1038/s41541-017-0030-8 [published Online First: 2017/12/22]
75. Vogel M, Augusto G, Chang X, et al. Molecular definition of severe acute respiratory syndrome coronavirus 2 receptor-binding domain mutations: Receptor affinity versus neutralization of receptor interaction. *Allergy* 2021 doi: 10.1111/all.15002
76. Teo A, Tan HD, Loy T, et al. Understanding antibody-dependent enhancement in dengue: Are afucosylated IgG1s a concern? *PLoS Pathog* 2023;19(3):e1011223. doi: 10.1371/journal.ppat.1011223 [published Online First: 20230330]
77. Torre-Minguela Cd, Castillo PFRd, Pelegrín P. The NLRP3 and Pyrin Inflammasomes: Implications in the Pathophysiology of Autoinflammatory Diseases. *Frontiers in Immunology* 2017 doi: 10.3389/fimmu.2017.00043
78. Lara-Reyna S, Caseley EA, Topping J, et al. Inflammasome activation: from molecular mechanisms to autoinflammation. *Clinical & Translational Immunology* 2022;11(7):e1404. doi: https://doi.org/10.1002/cti2.1404
79. Ozen S, Batu ED, Demir S. Familial Mediterranean Fever: Recent Developments in Pathogenesis and New Recommendations for Management. *Frontiers in Immunology* 2017 doi: 10.3389/fimmu.2017.00253
80. Migita K, Izumi Y, Jiuchi Y, et al. Familial Mediterranean fever is no longer a rare disease in Japan. *Arthritis Res Ther* 2016;18:175. doi: 10.1186/s13075-016-1071-5 [published Online First: 20160730]
81. Ben-Chetrit E, Touitou I. Familial Mediterranean Fever in the World. *Arthritis Care & Research* 2009;61(10):1447-53. doi: https://doi.org/10.1002/art.24458
82. Barut K, Pamuk G, Adrovic Yıldız A, et al. Comparison of Familial Mediterranean Fever and juvenile idiopathic arthritis patients according to

family origin. *Turk Pediatri Arsivi* 2018;53:31-36. doi: 10.5152/TurkPediatriArs.2018.5818
83. French FMFC. A candidate gene for familial Mediterranean fever. *Nat Genet* 1997;17(1):25-31. doi: 10.1038/ng0997-25
84. Consortium IF. Ancient missense mutations in a new member of the RoRet gene family are likely to cause familial Mediterranean fever. *Cell* 1997;90(4):797-807. doi: 10.1016/s0092-8674(00)80539-5
85. Tidow N, Chen X, Muller C, et al. Hematopoietic-specific expression of MEFV, the gene mutated in familial Mediterranean fever, and subcellular localization of its corresponding protein, pyrin. *Blood* 2000;95(4):1451-5.
86. Schnappauf O, Chae JJ, Kastner DL, et al. The Pyrin Inflammasome in Health and Disease. *Front Immunol* 2019;10:1745. doi: 10.3389/fimmu.2019.01745 [published Online First: 20190807]
87. Heilig R, Broz P. Function and mechanism of the pyrin inflammasome. *European Journal of Immunology* 2018;48(2):230-38. doi: https://doi.org/10.1002/eji.201746947
88. Gao W, Yang J, Liu W, et al. Site-specific phosphorylation and microtubule dynamics control Pyrin inflammasome activation. *Proceedings of the National Academy of Sciences of the United States of America* 2016;113(33):E4857-66. doi: 10.1073/pnas.1601700113 [published Online First: 20160801]
89. Chirita D, Bronnec P, Magnotti F, et al. Mutations in the B30.2 and the central helical scaffold domains of pyrin differentially affect inflammasome activation. *Cell Death Dis* 2023;14(3):213. doi: 10.1038/s41419-023-05745-9 [published Online First: 20230325]
90. Adwan MH. A brief history of familial Mediterranean fever. *Saudi Med J* 2015;36(9):1126-7. doi: 10.15537/smj.2015.9.12219
91. Marek-Yagel D, Berkun Y, Padeh S, et al. Clinical disease among patients heterozygous for familial Mediterranean fever. *Arthritis Rheum* 2009;60(6):1862-6. doi: 10.1002/art.24570
92. Booty MG, Chae JJ, Masters SL, et al. Familial Mediterranean fever with a single MEFV mutation: where is the second hit? *Arthritis Rheum* 2009;60(6):1851-61. doi: 10.1002/art.24569
93. Sarrauste de Menthiere C, Terriere S, Pugnere D, et al. INFEVERS: the Registry for FMF and hereditary inflammatory disorders mutations. *Nucleic Acids Res* 2003;31(1):282-5. doi: 10.1093/nar/gkg031
94. Touitou I, Lesage S, McDermott M, et al. Infevers: an evolving mutation database for auto-inflammatory syndromes. *Hum Mutat* 2004;24(3):194-8. doi: 10.1002/humu.20080
95. Shinar Y, Obici L, Aksentijevich I, et al. Guidelines for the genetic diagnosis of hereditary recurrent fevers. *Ann Rheum Dis* 2012;71(10):1599-605. doi: 10.1136/annrheumdis-2011-201271 [published Online First: 20120601]
96. Van Gijn ME, Ceccherini I, Shinar Y, et al. New workflow for classification of genetic variants' pathogenicity applied to hereditary recurrent fevers by the International Study Group for Systemic Autoinflammatory Diseases (INSAID). *J Med Genet* 2018;55(8):530-37. doi: 10.1136/jmedgenet-2017-105216 [published Online First: 20180329]
97. Richards S, Aziz N, Bale S, et al. Standards and guidelines for the interpretation of sequence variants: a joint consensus recommendation of the American College of Medical Genetics and Genomics and the Association for Molecular Pathology. *Genet Med* 2015;17(5):405-24. doi: 10.1038/gim.2015.30 [published Online First: 20150305]
98. Touitou I. The spectrum of Familial Mediterranean Fever (FMF) mutations. *Eur J Hum Genet* 2001;9(7):473-83. doi: 10.1038/sj.ejhg.5200658
99. Miyashita K, Matsuda Y, Okajima M, et al. Role of E148Q in familial Mediterranean fever with an exon 10 mutation in MEFV. *Pediatr Int* 2022;64(1):e14696. doi: 10.1111/ped.14696 [published Online First: 20211028]
100. Migita K, Asano T, Sato S, et al. Familial Mediterranean fever: overview of pathogenesis, clinical features and management. *Immunol Med* 2018;41(2):55-61. doi: 10.1080/13497413.2018.1481579 [published Online First: 20180907]
101. Majeed HA, Barakat M. Familial Mediterranean fever (recurrent hereditary polyserositis) in children: analysis of 88 cases. *Eur J Pediatr* 1989;148(7):636-41. doi: 10.1007/BF00441519
102. Barakat MH, Karnik AM, Majeed HW, et al. Familial Mediterranean fever (recurrent hereditary polyserositis) in Arabs--a study of 175 patients and review of the literature. *Q J Med* 1986;60(233):837-47.
103. Acer Kasman S, Duruoz MT. Spondyloarthritis in familial Mediterranean fever: a cohort study. *Rheumatol Int* 2022;42(10):1729-39. doi: 10.1007/s00296-022-05158-5 [published Online First: 20220618]
104. Migita K, Izumi Y, Fujikawa K, et al. Dysregulated mature IL-1beta production in familial Mediterranean fever. *Rheumatology (Oxford)* 2015;54(4):660-5. doi: 10.1093/rheumatology/keu359 [published Online First: 20140919]
105. Kilicaslan E, Duzenli T, Celik S, et al. Assessment of Serum Resistin and Plasma Calprotectin Levels as Biomarkers of Inflammation in Patients with Familial Mediterranean Fever Disease. *Mediterr J Rheumatol* 2022;33(3):322-27. doi: 10.31138/mjr.33.3.322 [published Online First: 20220930]
106. Tezcan D, Onmaz DE, Sivrikaya A, et al. Assessment of serum neopterin and calprotectin as

biomarkers for subclinical inflammation in patients with familial Mediterranean fever. *Ir J Med Sci* 2023;192(4):2015-22. doi: 10.1007/s11845-022-03173-w [published Online First: 20220926]
107. Ozdogan H, Ugurlu S. Familial Mediterranean Fever. *Presse Med* 2019;48(1 Pt 2):e61-e76. doi: 10.1016/j.lpm.2018.08.014 [published Online First: 20190125]
108. Yin X, Tian F, Wu B, et al. Interventions for reducing inflammation in familial Mediterranean fever. *Cochrane Database Syst Rev* 2022;3(3):CD010893. doi: 10.1002/14651858.CD010893.pub4 [published Online First: 20220329]
109. van der Hilst JCH, Bodar EJ, Barron KS, et al. Long-term follow-up, clinical features, and quality of life in a series of 103 patients with hyperimmunoglobulinemia D syndrome. *Medicine (Baltimore)* 2008;87(6):301-10. doi: 10.1097/MD.0b013e318190cfb7
110. van der Burgh R, Ter Haar NM, Boes ML, et al. Mevalonate kinase deficiency, a metabolic autoinflammatory disease. *Clin Immunol* 2013;147(3):197-206. doi: 10.1016/j.clim.2012.09.011 [published Online First: 20121004]
111. Houten SM, van Woerden CS, Wijburg FA, et al. Carrier frequency of the V377I (1129G>A) MVK mutation, associated with Hyper-IgD and periodic fever syndrome, in the Netherlands. *Eur J Hum Genet* 2003;11(2):196-200. doi: 10.1038/sj.ejhg.5200933
112. Favier LA, Schulert GS. Mevalonate kinase deficiency: current perspectives. *Appl Clin Genet* 2016;9:101-10. doi: 10.2147/TACG.S93933 [published Online First: 20160720]
113. Houten SM, Kuis W, Duran M, et al. Mutations in MVK, encoding mevalonate kinase, cause hyperimmunoglobulinaemia D and periodic fever syndrome. *Nat Genet* 1999;22(2):175-7. doi: 10.1038/9691
114. Cuisset L, Drenth JP, Simon A, et al. Molecular analysis of MVK mutations and enzymatic activity in hyper-IgD and periodic fever syndrome. *Eur J Hum Genet* 2001;9(4):260-6. doi: 10.1038/sj.ejhg.5200614
115. Nunez A, Castillo M, Iglesias J, et al. Regulation of mevalonate 5-pyrophosphate decarboxylase in HeLa cells. Inhibition of enzymatic protein synthesis by serum lipoproteins. *Int J Biochem Cell Biol* 1997;29(7):1037-41. doi: 10.1016/s1357-2725(97)00019-8
116. Yim YY, Zurawski Z, Hamm H. GPCR regulation of secretion. *Pharmacol Ther* 2018;192:124-40. doi: 10.1016/j.pharmthera.2018.07.005 [published Online First: 20180726]
117. Xu N, Shen N, Wang X, et al. Protein prenylation and human diseases: a balance of protein farnesylation and geranylgeranylation. *Sci China Life Sci* 2015;58(4):328-35. doi: 10.1007/s11427-015-4836-1 [published Online First: 20150411]
118. Li X, Liu L, Tupper JC, et al. Inhibition of protein geranylgeranylation and RhoA/RhoA kinase pathway induces apoptosis in human endothelial cells. *J Biol Chem* 2002;277(18):15309-16. doi: 10.1074/jbc.M201253200 [published Online First: 20020211]
119. Politiek FA, Waterham HR. Compromised Protein Prenylation as Pathogenic Mechanism in Mevalonate Kinase Deficiency. *Front Immunol* 2021;12:724991. doi: 10.3389/fimmu.2021.724991 [published Online First: 20210903]
120. Haas D, Hoffmann GF. Mevalonate kinase deficiencies: from mevalonic aciduria to hyperimmunoglobulinemia D syndrome. *Orphanet J Rare Dis* 2006;1:13. doi: 10.1186/1750-1172-1-13 [published Online First: 20060426]
121. Simon A, Drewe E, van der Meer JW, et al. Simvastatin treatment for inflammatory attacks of the hyperimmunoglobulinemia D and periodic fever syndrome. *Clin Pharmacol Ther* 2004;75(5):476-83. doi: 10.1016/j.clpt.2004.01.012
122. Bodar EJ, van der Hilst JC, Drenth JP, et al. Effect of etanercept and anakinra on inflammatory attacks in the hyper-IgD syndrome: introducing a vaccination provocation model. *Neth J Med* 2005;63(7):260-4.
123. Lainka E, Neudorf U, Lohse P, et al. Analysis of Cryopyrin-Associated Periodic Syndromes (CAPS) in German Children: Epidemiological, Clinical and Genetic Characteristics. *Klin Padiatr* 2010;222(06):356-61. doi: 10.1055/s-0030-1265181
124. Cuisset L, Jeru I, Dumont B, et al. Mutations in the autoinflammatory cryopyrin-associated periodic syndrome gene: epidemiological study and lessons from eight years of genetic analysis in France. *Ann Rheum Dis* 2011;70(3):495-9. doi: 10.1136/ard.2010.138420 [published Online First: 20101124]
125. Mehr S, Allen R, Boros C, et al. Cryopyrin-associated periodic syndrome in Australian children and adults: Epidemiological, clinical and treatment characteristics. *J Paediatr Child Health* 2016;52(9):889-95. doi: 10.1111/jpc.13270
126. Booshehri LM, Hoffman HM. CAPS and NLRP3. *J Clin Immunol* 2019;39(3):277-86. doi: 10.1007/s10875-019-00638-z [published Online First: 20190510]
127. Stych B, Dobrovolny D. Familial cold auto-inflammatory syndrome (FCAS): characterization of symptomatology and impact on patients' lives. *Current Medical Research and Opinion* 2008;24(6):1577-82. doi: 10.1185/03007990802081543
128. Welzel T, Kuemmerle-Deschner JB. Diagnosis and Management of the Cryopyrin-Associated Periodic Syndromes (CAPS): What Do We Know Today? *J Clin Med* 2021;10(1) doi: 10.3390/jcm10010128 [published Online First: 20210101]

129. Aksentijevich I, D. Putnam C, Remmers EF, et al. The clinical continuum of cryopyrinopathies: Novel CIAS1 mutations in North American patients and a new cryopyrin model. *Arthritis & Rheumatism* 2007;56(4):1273-85. doi: https://doi.org/10.1002/art.22491
130. Nishikomori R, Izawa K, Kambe N, et al. Low-frequency mosaicism in cryopyrin-associated periodic fever syndrome: mosaicism in systemic autoinflammatory diseases. *Int Immunol* 2019;31(10):649-55. doi: 10.1093/intimm/dxz047
131. de Zoete MR, Palm NW, Zhu S, et al. Inflammasomes. *Cold Spring Harb Perspect Biol* 2014;6(12):a016287. doi: 10.1101/cshperspect.a016287 [published Online First: 20141016]
132. Doitsh G, Galloway NL, Geng X, et al. Cell death by pyroptosis drives CD4 T-cell depletion in HIV-1 infection. *Nature* 2014;505(7484):509-14. doi: 10.1038/nature12940
133. Sefik E, Qu R, Junqueira C, et al. Inflammasome activation in infected macrophages drives COVID-19 pathology. *Nature* 2022;606(7914):585-93. doi: 10.1038/s41586-022-04802-1 [published Online First: 20220428]
134. Dostert C, Petrilli V, Van Bruggen R, et al. Innate immune activation through Nalp3 inflammasome sensing of asbestos and silica. *Science* 2008;320(5876):674-7. doi: 10.1126/science.1156995 [published Online First: 20080410]
135. Hornung V, Bauernfeind F, Halle A, et al. Silica crystals and aluminum salts activate the NALP3 inflammasome through phagosomal destabilization. *Nat Immunol* 2008;9(8):847-56. doi: 10.1038/ni.1631 [published Online First: 20080711]
136. Martinon F, Petrilli V, Mayor A, et al. Gout-associated uric acid crystals activate the NALP3 inflammasome. *Nature* 2006;440(7081):237-41. doi: 10.1038/nature04516 [published Online First: 20060111]
137. Swanson KV, Deng M, Ting JP. The NLRP3 inflammasome: molecular activation and regulation to therapeutics. *Nat Rev Immunol* 2019;19(8):477-89. doi: 10.1038/s41577-019-0165-0
138. Frising UC, Ribo S, Doglio MG, et al. Nlrp3 inflammasome activation in macrophages suffices for inducing autoinflammation in mice. *EMBO Rep* 2022;23(7):e54339. doi: 10.15252/embr.202154339 [published Online First: 20220516]
139. He Y, Zeng MY, Yang D, et al. NEK7 is an essential mediator of NLRP3 activation downstream of potassium efflux. *Nature* 2016;530(7590):354-7. doi: 10.1038/nature16959 [published Online First: 20160127]
140. McDermott MF, Aksentijevich I, Galon J, et al. Germline mutations in the extracellular domains of the 55 kDa TNF receptor, TNFR1, define a family of dominantly inherited autoinflammatory syndromes. *Cell* 1999;97(1):133-44. doi: 10.1016/s0092-8674(00)80721-7
141. Cudrici C, Deuitch N, Aksentijevich I. Revisiting TNF Receptor-Associated Periodic Syndrome (TRAPS): Current Perspectives. *Int J Mol Sci* 2020;21(9) doi: 10.3390/ijms21093263 [published Online First: 20200505]
142. Salomon BL, Leclerc M, Tosello J, et al. Tumor Necrosis Factor alpha and Regulatory T Cells in Oncoimmunology. *Front Immunol* 2018;9:444. doi: 10.3389/fimmu.2018.00444 [published Online First: 20180312]
143. Chen G, Goeddel DV. TNF-R1 signaling: a beautiful pathway. *Science* 2002;296(5573):1634-5. doi: 10.1126/science.1071924
144. Rebelo SL, Bainbridge SE, Amel-Kashipaz MR, et al. Modeling of tumor necrosis factor receptor superfamily 1A mutants associated with tumor necrosis factor receptor-associated periodic syndrome indicates misfolding consistent with abnormal function. *Arthritis Rheum* 2006;54(8):2674-87. doi: 10.1002/art.21964
145. Lv S, Li X, Wang H. The Role of the Effects of Endoplasmic Reticulum Stress on NLRP3 Inflammasome in Diabetes. *Front Cell Dev Biol* 2021;9:663528. doi: 10.3389/fcell.2021.663528 [published Online First: 20210414]
146. Lachmann HJ, Papa R, Gerhold K, et al. The phenotype of TNF receptor-associated autoinflammatory syndrome (TRAPS) at presentation: a series of 158 cases from the Eurofever/EUROTRAPS international registry. *Ann Rheum Dis* 2014;73(12):2160-7. doi: 10.1136/annrheumdis-2013-204184 [published Online First: 20130821]
147. Ozen S, Kuemmerle-Deschner JB, Cimaz R, et al. International Retrospective Chart Review of Treatment Patterns in Severe Familial Mediterranean Fever, Tumor Necrosis Factor Receptor-Associated Periodic Syndrome, and Mevalonate Kinase Deficiency/Hyperimmunoglobulinemia D Syndrome. *Arthritis Care Res (Hoboken)* 2017;69(4):578-86. doi: 10.1002/acr.23120 [published Online First: 20170303]
148. Georgin-Lavialle S, Kone-Paut I, Delaleu J, et al. [Tumor necrosis receptor associated periodic syndrome (TRAPS): State of the art]. *Rev Med Interne* 2018;39(4):256-64. doi: 10.1016/j.revmed.2018.02.002 [published Online First: 20180307]